



universität
wien

DIPLOMARBEIT

Titel der Diplomarbeit

„Increasing the Signal to Noise Ratio in MR Spectroscopic
Imaging by Coil Combination at 7T“

Verfasser

Bernhard Strasser

angestrebter akademischer Grad

Magister der Naturwissenschaften (Mag. rer. nat.)

Wien, 2012

Studienkennzahl lt. Studienblatt:

A 411

Studienrichtung lt. Studienblatt:

411 Diplomstudium Physik UniStG

Betreuer:

a.o. Univ.-Prof. Mag. Dr. Wilfried Schranz

Kurzfassung

Das Ziel dieser Diplomarbeit war es das Signal zu Rausch Verhältnis (SNR) in der Magnetresonanz-Spektroskopiebildgebung (MRSI) bei 7 T durch die Benutzung von Mehrkanalspulen (AC) zu erhöhen. Mithilfe dieser Spulen kann das SNR stark verbessert werden, indem die einzelnen Kanäle der Spule aufsummiert werden. Es zeigt sich allerdings, dass diese Kanalkombination im Falle von spektroskopischen Daten problematisch ist, da das einfache Aufsummieren zu einer Signalauslöschung aufgrund von Phasendifferenzen der einzelnen Kanäle führt. Die Spektren der einzelnen Kanäle müssen daher vorher phasiert werden. Die gängige Methode um dies zu Erreichen benutzt den ersten Datenpunkt der FIDs, was bei guter Wasserunterdrückung aber zu unzuverlässigen Ergebnissen führen kann. Daher wurde die Phase mithilfe von schnellen Gradientenecho-Bildgebungssequenzen (GRE) bestimmt. Mit deren Hilfe wurde jedes Voxel und jeder Kanal der MRSI Daten phasiert und gewichtet. Dies führt zu einer geringeren Signalauslöschung im Vergleich zur gängigen Methode.

Die Realisierbarkeit der neuen Methode wurde durch das Messen der Gehirne von 7 gesunden Probanden und 3 Phantommessungen gezeigt. Dafür wurde im ersten Schritt nachgewiesen, dass das Phasieren von MRSI-Daten mithilfe von GRE-Daten grundsätzlich möglich ist. Im nachfolgenden zweiten Schritt wurde ein Algorithmus programmiert, mit dessen Hilfe spektroskopische Daten von AC-Kanälen mit oben genannter neuen Methode kombiniert werden können. Daraufhin wurde der SNR-Gewinn durch diese Methode im Vergleich zu einer Volumsspule mit den Messdaten ermittelt. Im letzten Schritt wurde gezeigt, dass diese neu entwickelte Methode zur Kanalkombination zu besseren Ergebnissen in Bezug auf SNR und Reproduzierbarkeit führt als die gängige Methode, insbesondere nahe der Oberfläche des Gehirns.

Abstract

The aim of this diploma thesis was to increase the Signal to Noise Ratio (SNR) in Magnetic Resonance Spectroscopic Imaging (MRSI) at 7 T by deploying Array Coils (AC). ACs can highly increase the SNR when summing up the individual channels. Yet, the combination of spectroscopic data is problematic due to phase differences between the channels, leading to signal cancellations if the channels are naively summed up. To prevent this, the signal of each channel has to be phased prior to summing. The phase information is typically obtained by the first FID data point. However, for good water suppression, this method can be unreliable. Therefore, a method is proposed with which the phase is estimated from fast Gradient Echo (GRE) imaging sequences. Each voxel and each channel is phased and weighted with these additional GRE data, leading to less signal cancellations in comparison to the conventional method.

In order to show the feasibility of this method and its superiority over the established method, MRSI and GRE data of 7 healthy volunteers and 3 phantoms were measured. Thus, in the first step the possibility to phase MRSI data with GRE data was proven. In the subsequent step, an algorithm for combining the MRSI data of the AC-channels with the above mentioned new method was written. Then, the gain in the SNR using this method in comparison with the data of a Volume Coil was estimated using the measured data. Finally, the superiority of the new coil combination method over the established one was shown in terms of SNR and reproducibility, particularly at the surface of the brain.

Contents

Kurzfassung/Abstract	3
Abbreviations & Symbols	11
1 Introduction	13
2 Theoretical Background	17
2.1 Basic Principle	17
2.2 Quantum Mechanical Properties	17
2.2.1 The Spin	17
2.2.2 The Magnetic Moment	19
2.2.3 The Equation of Motion	19
2.2.4 Chemical Shift	20
2.2.5 Macroscopic Magnetization	22
2.3 Setup of a medical NMR scanner	24
2.3.1 Overview	24
2.3.2 RF Coils	26
2.4 Signal Acquisition - From Excitation to the Spectrum	27
2.4.1 Excitation	27
2.4.2 Relaxation	30
T1 Relaxation	30
T2- and T2*-Relaxation	31
Bloch Equation	33
2.4.3 Acquisition	33
2.4.4 Fourier Transformation & the Spectrum	35
2.5 The Phase in Detail	37
2.5.1 Zero Order Phase	38
Distance to the Coil	38
Different Cable Lengths	38
B0 Inhomogeneities	38

2.5.2	First Order Phase	39
2.6	Localization	41
2.6.1	The Effects of Gradients	43
2.6.2	Slice Selection	44
2.6.3	Frequency Encoding	44
2.6.4	Phase Encoding	45
2.6.5	k-Space	46
2.6.6	MR Imaging vs MR Spectroscopic Imaging	48
2.7	Sequences	49
2.7.1	The Simplest Possible Sequence	50
2.7.2	The Simplest Possible Spin Echo Sequence	50
2.7.3	The Gradient Echo Sequence	51
2.7.4	FID-Based MRSI Sequence	53
2.8	Postprocessing	54
2.8.1	Fourier Transformation	54
2.8.2	Apodization	54
2.8.3	Zero Filling	55
2.8.4	Fitting the Spectroscopic Data	56
2.8.5	Phasing the signal	57
	Correcting the Zero Order Phases	57
	Correcting the First Order Phases	58
3	Implementation	59
3.1	Materials & Methods: General Information	59
3.1.1	Principle of Coil Combination	59
3.1.2	Work plan	60
3.1.3	Hardware	61
	The Scanner and the Coil	61
	The Phantoms	62
3.1.4	Sequences	64
	The MRSI Sequence	64
	The Gradient Echo Sequence	67
	Phase Problems of the GRE Sequence	68
3.1.5	Basis Set	70
3.1.6	The Basic Algorithm	71
3.1.7	The Data	72

	Using the Raw Data	72
	The Measured Datasets	73
3.2	Step 1: Validation of Proper Phasing & Additional Benefits	74
3.2.1	Materials & Methods	74
	Part A: Comparison of Phase Maps	74
	Part B: Side Benefits	75
3.2.2	Results	77
	Part A: Phase Map Comparison	77
	Part B: Side Benefits	81
3.3	Step 2: Implementing the Coil Combination Algorithm	85
3.3.1	Materials & Methods	85
3.3.2	Results	87
3.4	Step 3: Validation of SNR Increase	89
3.4.1	Materials & Methods	89
	The SNR Computation Function	89
	Evaluation of the SNR Results	93
3.4.2	Results	94
3.5	Step 4: Comparison with Available Techniques	97
3.5.1	Materials & Methods	97
	Description of the Available Technique	97
	Comparison of the methods	98
3.5.2	Results	98
4	Summary	103
	Bibliography	105
	Appendix	107

Abbreviations

AC	Array Coil
ADC	Analog to Digital Converter
FID	Free Induction Decay
GIN	Gradient echo Image based coil combiNation
GRE	Gradient Echo
Ins	<i>myo</i> -Inositol
MRI	Magnetic Resonance Imaging
MRSI	Magnetic Resonance Spectroscopic Imaging
(t)NAA	(total) N-Acetyl Aspartate
NMR	Nuclear Magnetic Resonance
RF	Radio Frequency
rms	Root Mean Square
SC	Surface Coil
SNR	Signal to Noise Ratio
(t)Cho	(total) Choline
(t)Cr	(total) Creatine
TE	Echo Time
VC	Volume Coil

Mathematical Operators

$\ \cdot \ $	Euclidean norm of a vector
$\langle \cdot, \cdot \rangle$	Standard dot product in the euclidean space
\times	Cross product
$*$	Complex conjugation operator

Contents

1 Introduction

Nuclear Magnetic Resonance (NMR) is an effect that is commonly used in medicine. Since its first medical applications by Lauterbur and Mansfield in 1973 [Haacke et al., 1999, p. 2], medical NMR rose to an vital technique in diagnostics to detect tumors, multiple sclerosis, damages in ligaments, tendons and cartilage, and many other diseases. In contrast to Computer Tomography, NMR does not expose patients and volunteers to any ionizing radiation, and can thus be seen as harmless for the human body [Badurek, 2010, p.32] [Haacke et al., 1999, p.2].

One specific method of NMR is proton Magnetic Resonance Spectroscopy, a method to detect certain chemical groups containing protons. Beside its widespread usage in structural chemistry and biology, Magnetic Resonance Spectroscopy is as well used in medical imaging, since many metabolites in humans can be identified that bear valuable information. Magnetic Resonance Spectroscopic Imaging (MRSI) combines the methods of conventional MR Imaging (MRI), i.e. localization of the signal, with Magnetic Resonance Spectroscopy, hence providing information about the metabolite concentrations in dependence of the position.

Great efforts were made since the first medical application of NMR in order to improve the quality of the images and spectra. One way to achieve this is to use so called “Array Coils” (AC), consisting of several individual Radio Frequency (RF) coils, often referred to as channels, for signal acquisition. Each of these channels can only detect signal from a very distinct volume. Nevertheless, the combination of these channels lead to a higher SNR than using a single coil that covers the whole volume of interest (so called Volume Coils (VC)).

In conventional MRI, this combination is easily performed, since only the magnitude of the signal is of interest. However, in MRSI, the phase of the signal plays an important role. Since the signals obtained from different coils of an AC have different phases, and summing up differently phased signals nullifies these, the naive summation of the coils would lead to signal cancellations and totally distorted spectra. Therefore, the signal of

1 Introduction

the individual channels have to be phased somehow, prior to summation.

Another way to improve the data quality in NMR is to use high magnetic fields. The benefits of using ultra high magnetic fields (≥ 7 T) are among others an increased Signal to Noise Ratio (SNR) and an enhanced discrimination of metabolite peaks. However, severe problems are encountered in MRSI at high fields, as the measured signal decays faster, higher energies are deposited in the tissue of the patients/volunteers leading to an unwanted warming, and increased inhomogeneities in the involved magnetic fields [Bogner et al., 2011] [Henning et al., 2009].

Henning et al. proposed a new method in 2009 to solve these problems by measuring the signal directly after excitation. A quantification of 13 metabolites with an uncertainty below 20% were reported [Henning et al., 2009]. Bogner et al. adapted and modified this method in 2011 [Bogner et al., 2011].

Based on this work of Bogner et al., the aim of this diploma thesis was to develop a robust method for combining the signals of the individual AC channels. This was achieved by measuring, in addition to the MRSI data, a conventional MR image with each channel and with similar parameters. The MRSI data were then phased and weighted by these images channel by channel and the signals of all channels were subsequently summed. The measurements were performed using a 7 T NMR scanner at the MR Center of Excellence of the Medical University of Vienna.

The work was subdivided in four steps: The first one proves the feasibility and reliability of phasing MRSI with MRI data. In the second one, the coil combination algorithm was programmed using MATLAB (version 2007b; MathWorks, Natick, Mass) and Bash. Subsequently, the AC and VC were compared with respect to the SNR in order to estimate the benefits of this method. Finally, the new coil combination method was compared with the state of the art method.

The work of this diploma thesis is part of a project (“7 Tesla MR spectroscopy in diffusely infiltrating gliomas”, FWF Grant KLI 61, 2011) that aims to develop a 3D-MRSI sequence for measuring the whole brain within a feasible time, i.e. less than 10 minutes, for usage in clinical routine. The first part of the project was finished by the thesis by highly increasing the SNR, and enabling the usage of so called “Parallel Imaging” to accelerate the measurement. Thus, the next steps are to implement Parallel Imaging and extending the sequence from a 2D- to a 3D-sequence. The resulting sequence is

supposed to be used then, among other applications, to improve the reliable discrimination between tumor and normal tissue to support neurosurgeons pre-operatively in their decisions of tissue removal.

1 Introduction

2 Theoretical Background

2.1 Basic Principle

The basis of NMR is the spin of nuclei. A non-zero spin leads to a magnetic moment of the nucleus, which, together with an external magnetic field results in a certain resonance frequency of the magnetic moment. The frequency is dependent on the external field and the gyromagnetic ratio γ . In case of NMR, the frequency is within the RF range. Applying an electromagnetic field matching this frequency, the resonance condition is fulfilled, and the nucleus gets excited. During the subsequent relaxation process, the nucleus emits an electromagnetic field itself while falling back again to the ground state. This radiation of matter can be measured by a nearby coil. Information can be extracted out of the signal, e.g. the density of the nuclei can be determined.

Classical physics is not capable of describing the phenomena of NMR completely. Instead, standard Quantum Mechanics or a comparable theory has to be used. However, most phenomena of NMR can be understood in a semi-classical approach. Therefore a semi-classical description of NMR was chosen for this work. An extensive quantum mechanical description of NMR can be found in [Haacke et al., 1999].

The following description of the basic principles of NMR is largely based on [de Graaf, 2007], [Haacke et al., 1999] and [Badurek, 2010]. Statements and facts that are not referenced can be assumed to be either general knowledge of physicists, or taken from one of the aforementioned sources.

2.2 Quantum Mechanical Properties

2.2.1 The Spin

The spin \vec{I} of a nucleus can be described as a vector. According to quantum mechanics, the magnitude of the spin is quantized by the spin quantum number I :

2 Theoretical Background

$$\|\vec{I}\| = \hbar\sqrt{I(I+1)} \quad (2.1)$$

where $\|\cdot\|$ denotes the euclidean norm of a vector. The spin quantum number of the nucleus depends on its number of neutrons and protons. It is positive and

- integer, if the number of neutrons and the number of protons are odd
- zero, if the number of neutrons and the number of protons are even
- half-integer, otherwise.

In table 2.1 the spin numbers of NMR relevant nuclei and their gyromagnetic ratios γ (see below) are listed.

Nucleus	I [\hbar]	γ [Mrad T ⁻¹ s ⁻¹]
¹ H	1/2	267.52
² H	2	41.07
¹⁷ O	5/2	-36.28
¹⁹ F	1/2	251.81
²³ Na	3/2	70.80
³¹ P	1/2	108.41
¹³ C	1/2	67.28

Table 2.1: The spin quantum numbers I and the gyromagnetic ratios γ of some nuclei commonly used in NMR [de Graaf, 2007].

If an external magnetic field \vec{B}_0 is applied along the z-axis, the z-component of the spin is quantized as well. The z-component is then given by

$$I_z = \hbar m \quad (2.2)$$

where m is the magnetic quantum number. The possible values of m are restricted by I :

$$m \in \{-I, -I+1, \dots, I\} \quad (2.3)$$

In this diploma thesis we will focus on **proton** NMR spectroscopy. Protons are the most commonly used nuclei in medical NMR. Their quantum numbers are $I = 1/2$ and $m \in \{-1/2, 1/2\}$.

2.2.2 The Magnetic Moment

The spin \vec{I} of a charged particle or a particle containing charged sub-particles (like neutrons) is associated to a magnetic dipole moment of

$$\vec{\mu} = \gamma \vec{I} \quad (2.4)$$

where γ is the gyromagnetic ratio (e.g. of a nucleus). Although the nuclei have a magnetic dipole moment, they do not align with an external magnetic field. This is due to the fact that the magnitude as well as the z-component of $\vec{\mu}$ is quantized. Using eq. (2.1) - (2.4), the cosine of the angle Θ between $\vec{\mu}$ and the external magnetic field \vec{B}_0 can be computed as:

$$\cos \Theta = \frac{\langle \vec{\mu}, \vec{B}_0 \rangle}{\|\vec{\mu}\| \|\vec{B}_0\|} = \frac{m}{\sqrt{I(I+1)}} \quad (2.5)$$

For protons with $I = 1/2$, this results in $\Theta \approx \pm 54.74^\circ$ [de Graaf, 2007, p. 6]. It is convenient to refer to the state with $\Theta > 0$ as the "parallel"- or the α -state and the other one as the "antiparallel" or β -state.

2.2.3 The Equation of Motion

The external magnetic field causes a torque \vec{N} on $\vec{\mu}$, given by

$$\vec{N} = \vec{\mu} \times \vec{B}_0 \quad (2.6)$$

The torque is the time derivative of the angular momentum, and the spin \vec{I} can be interpreted as an angular momentum in a semi-classical picture. Therefore, eq. (2.6) can be rewritten as

$$\frac{d\vec{I}}{dt} = \vec{\mu} \times \vec{B}_0 \quad (2.7)$$

which leads to

$$\frac{d\vec{\mu}}{dt} = \gamma \vec{\mu} \times \vec{B}_0 \quad (2.8)$$

using eq. (2.4).

Eq. (2.8) is the equation of motion for a single spin in an external magnetic field. It describes a circular motion around \vec{B}_0 with an angular frequency of $\omega_0 = \gamma B_0$ (defining

2 Theoretical Background

$B_0 := \|\vec{B}_0\|$) in the mathematical negative sense (clockwise). Thus, it is convenient to define the Larmor frequency as

$$\vec{\omega}_0 := -\gamma \vec{B}_0 \quad (2.9)$$

Eq. (2.8) can then be rewritten to

$$\frac{d\vec{\mu}}{dt} = \vec{\omega}_0 \times \vec{\mu} \quad (2.10)$$

In fig. 2.1 the motion of a single magnetic moment $\vec{\mu}$ is shown.

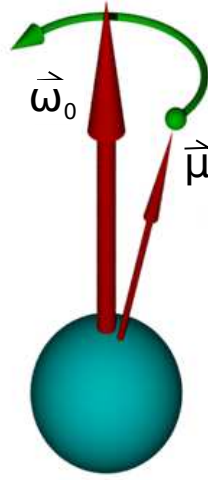


Figure 2.1: The main magnetic field \vec{B}_0 causes the magnetic moment $\vec{\mu}$ to precess around $\vec{\omega}_0$. From: “Yamavu”, 29.01.2009, available at Wikimedia Commons (URL: <http://de.wikipedia.org/w/index.php?title=Datei:Pr%C3%A4zession2.png&filetimestamp=20090129155713>), no License, Time of access: 29.03.2012.

2.2.4 Chemical Shift

The chemical environment influences the local magnetic field to which the nucleus is exposed to, because the electrons of the neighbouring atoms shield off the magnetic field. The local magnetic field \vec{B}_{Loc} can be described by the empirical law

$$\vec{B}_{Loc} = (1 - \sigma) \vec{B}_0 \quad (2.11)$$

which leads to a lowered Larmor frequency according to eq. (2.9):

$$\omega_{Loc} = (1 - \sigma) \omega_0 \quad (2.12)$$

where σ is the shielding constant and ω_0 and ω_{Loc} the norms of the corresponding vectors. This means that the same type of nucleus can have different Larmor frequencies dependent on the molecule it is bound to. It is possible to determine the chemical compound due to its characteristic set of frequencies. In fig. 2.2, a spectrum that is acquired from a rat brain at 11.75 T can be seen [de Graaf, 2007, p. 44]. The spectrum contains peaks of different chemical compounds like N-acetyl aspartate (NAA), total creatine (tCr) which is the sum of phosphocreatine and inorganic creatine, and total choline (tCho, the sum of choline, phosphorylcholine and glycerophosphocholine).

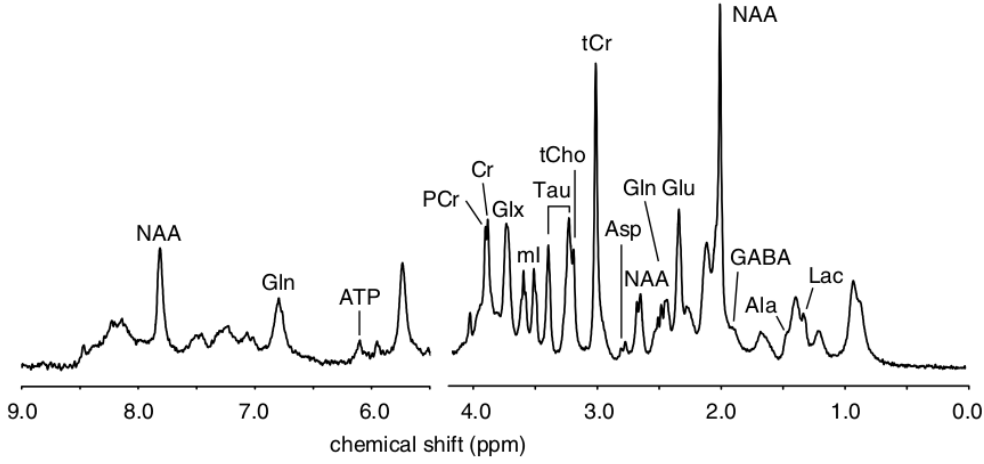


Figure 2.2: Example spectrum of a rat brain acquired with an 11.75 T scanner. From: [de Graaf, 2007, p. 44].

Note that on the horizontal axis the chemical shift δ instead of the frequency is plotted, defined as

$$\delta := \frac{\omega - \omega_{ref}}{\omega_{ref}} \cdot 10^6 \quad (2.13)$$

where ω_{ref} is the angular frequency of a reference compound.

In contrast to the frequency, the chemical shift is not dependent on the main magnetic field B_0 . The subtraction of ω_{ref} sets the chemical shift of the reference compound to zero, and by dividing through its frequency, the chemical shift (in ppm) becomes independent of B_0 . This simplifies the usage in NMR spectroscopy and is the reason for the

2 Theoretical Background

widespread use of the chemical shift instead of the frequency.

In proton NMR spectroscopy the reference compound is tetra methyl silane (TMS), having a frequency of about 298 MHz at 7 T [de Graaf, 2007, p. 19].

The frequencies of all chemical compounds are proportional to the magnetic field strength B_0 as can be seen from eq. (2.12) and (2.9). Therefore the frequency difference between two chemical compounds with shielding constants σ_1 and σ_2 and angular frequencies ω_1 and ω_2 increases with higher B_0 :

$$\Delta\omega = (\sigma_2 - \sigma_1) B_0 \quad (2.14)$$

This means that the resonance peaks of different chemical compounds are better distinguishable and less overlapping at higher magnetic fields, which is one reason for the trend towards higher main magnetic fields B_0 .

2.2.5 Macroscopic Magnetization

The energy E of a magnetic dipole moment $\vec{\mu}$ in an external magnetic field \vec{B}_0 is given by:

$$E = \langle \vec{\mu}, \vec{B}_0 \rangle = \gamma \hbar B_0 m \quad (2.15)$$

For the latter equality eq. (2.2) - (2.4) were used. Because of the quantization of $\vec{\mu}$, the energy of the spin is quantized as well by the magnetic spin quantum number m . This energy splitting is called Zeeman effect. States with lower energies are more probable than those with higher energy. For $I = 1/2$ (e.g. 1H) there are only two energy levels:

$$E = \pm \frac{1}{2} \gamma \hbar B_0 \quad (2.16)$$

The energy difference

$$\Delta E = \gamma \hbar B_0 \quad (2.17)$$

causes the spin state that is parallel to the magnetic field ($m = +1/2$) to be more probable than the other.

If we consider a macroscopic material with a huge number of spins, the net magnetization is given by

$$\vec{M} = \sum_i \vec{\mu}_i \quad (2.18)$$

The unequal occupation probabilities of the energy states lead to a population difference of these, and therefore to a net magnetization that is parallel to \vec{B}_0 , as described by the Boltzmann distribution:

$$\frac{n_{\text{antiparallel}}}{n_{\text{parallel}}} = e^{-\frac{\Delta E}{k_B T}} \quad (2.19)$$

with $n_{\text{antiparallel}}$ and n_{parallel} being the number of spins in the antiparallel and parallel state, respectively.

In thermal equilibrium, the x- and y-components of \vec{M} are zero, because the individual magnetic moments $\vec{\mu}_i$ are equally distributed in the x-y-plane (i.e. they do not have any phase coherence). In fig. 2.3 the magnetic moments and the resulting net magnetization in thermal equilibrium are depicted.

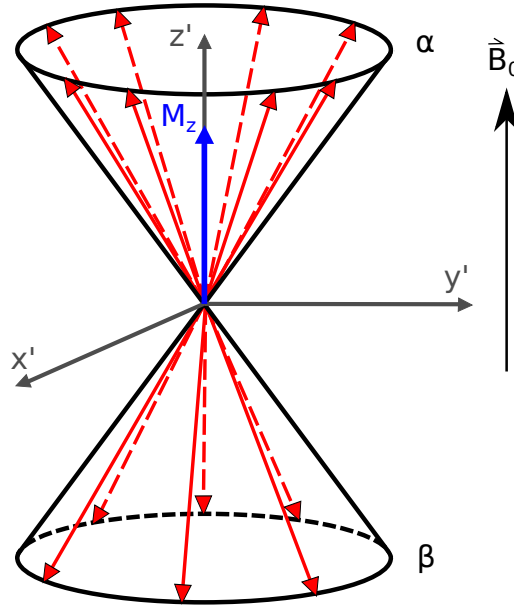


Figure 2.3: The individual magnetic moments are equally distributed in the transverse plane leading to no net transverse magnetization. However, more spins are in the α -state, resulting in a net magnetization parallel to \vec{B}_0 and the z' -axis. The apostrophe of the axes denotes the frame of reference co-rotating with the magnetic moments $\vec{\mu}_i$.

2 Theoretical Background

Summing over the magnetic moments in eq. (2.8) leads to the macroscopic equation of motion

$$\frac{d\vec{M}}{dt} = \gamma \vec{M} \times \vec{B}_0 \quad (2.20)$$

which as well describes a precession around the z-axis. The solution of eq. (2.20) can be written as

$$\vec{M}(t, \vec{r}) = \begin{pmatrix} M_{xy}(\vec{r}) \cos(\omega_0 t + \varphi_{total}(\vec{r})) \\ -M_{xy}(\vec{r}) \sin(\omega_0 t + \varphi_{total}(\vec{r})) \\ M_z(\vec{r}) \end{pmatrix} \quad (2.21)$$

$M_{xy}(t, \vec{r})$ is the amplitude of \vec{M} in the x-y (i.e. transversal) plane, and $\varphi_{total}(\vec{r})$ is the total phase at $t = 0$.

Eq. (2.20) implies a static magnetization in thermal equilibrium, where $M_x = M_y = 0$ and M_z is constant. Therefore, no signal can be measured in thermal equilibrium. However, the magnetization precesses around \vec{B}_0 with the same frequency as the magnetic moments $\vec{\mu}_i$, as soon as the magnetization is tilted towards the x-y-plane. This can be achieved by a radio frequency (RF) pulse which is described in section 2.4.1.

2.3 Setup of a medical NMR scanner

In order to understand the acquisition of an NMR signal in a real experiment, we need some basic information about the hardware of a medical NMR scanner. The RF coils for excitation and signal acquisition will be discussed in more detail because their understanding is crucial for the present diploma thesis.

2.3.1 Overview

In fig. 2.4, the schematic setup of a medical whole-body NMR scanner for investigations in human subjects can be seen.

The most important components of an NMR scanner are:

- The magnet/coil responsible for the main magnetic field. In most modern scanners this is realized as a superconducting coil. The field strength of medical scanners

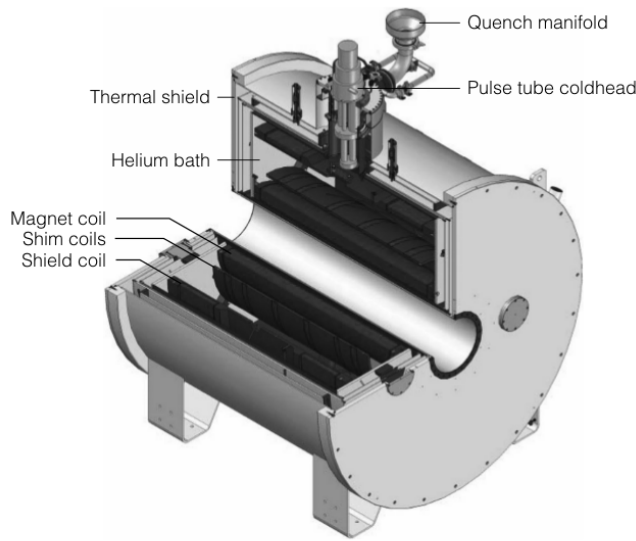


Figure 2.4: Schematic setup of an medical NMR scanner. From: [de Graaf, 2007, p. 483].

currently ranges from 0.1 T to 9.4 T, with NMR scanners above 3 T still being used exclusively for scientific studies.

- The shim coils: Non-superconducting coils for improving the field homogeneity by adjusting the currents that flow through these coils.
- The gradient coils for applying an additional magnetic field to the tissue in order to achieve spatial localization of the signal. These coils are non-superconducting electromagnets with a strength of typically $25\text{--}45\text{ mT m}^{-1}$ each, and that can be switched very fast (typical gradient slew rates are $200\text{ T s}^{-1}\text{ m}^{-1}$). There is one gradient for each Cartesian direction. A combination of all three leads to a gradient in any desired direction.
- The RF coils: Coils for exciting the spins and for signal reception.
- The RF transmission system, consisting of a synthesizer, a modulator, an amplifier and a computer, that creates an RF signal, determines the shape of the signal, amplifies the pulse, and controls the whole process [de Graaf, 2007, p. 536 f.].
- The signal reception system. The first step is to preamplify the signal followed by downsampling the signal to a frequency range of 10 MHz. Afterwards, the signal is split in its x- and y-component, again downsampled to frequencies in the range

of kHz and digitized by an Analog to Digital Converter (ADC). Finally the signal is saved by a computer [de Graaf, 2007, p. 537 ff.].

2.3.2 RF Coils

There are several different types of coils available for NMR applications. These can be subdivided into three major groups: Volume Coils (VC), Surface Coils (SC) and Array Coils (AC) [Haacke et al., 1999, p. 853 ff.] [de Graaf, 2007, p. 531 ff.].

VCS are large coils with a typical diameter of 20-30 cm for a head coil. This type of coils provides a homogeneous B_1 - field, leading to an excitation angle that is uniform across the whole sample. Moreover, a VC receives the signal homogeneously within a large volume. The drawback of VCs is their large size and poor filling factor resulting in low SNRs when used for signal acquisition. The sensitivity profile of a VC head coil can be seen in fig. 2.5 a.

In contrary to VCs, a SC has a small diameter of typically 5-10 cm. SCs have a very distinct sensitivity profile which can be seen in fig. 2.5 b. Although SCs cannot fully cover a volume like a whole head due to its distinct sensitivity profile, they have a very high sensitivity adjacent to the coil, which rapidly drops with distance. The SNR close to an SC is much higher than that of a VC.

An AC is, in simplified terms, a set of SCs put together in one coil housing. Interaction between these coils (referred to as coupling) has to be restricted in order to prevent signal loss [de Graaf, 2007, p. 532]. Each individual SC of the AC acquires signal from the whole volume. If these signals are summed up for every spatial position, a much higher SNR is achieved compared to a VC. For optimally placed coils, the SNR is higher in the whole region of interest.

The sensitivity profile of an AC can be seen in fig. 2.5 c. The homogeneity of an AC is between that of a VC and an SC, with a higher SNR at the surface and a lower in the middle of the region of interest.

ACs are rarely used for excitation because of the high demands on additional scanner hardware. Nevertheless, recent results suggest that there are certain advantages for such parallel transmission techniques, especially at high magnetic field strengths, if several hardware limitations can be overcome [Katscher and Börnert, 2006]. Although ACs are

in most cases superior to VCs and SCs in signal acquisition, the combination of the signals from all coils can be complicated.

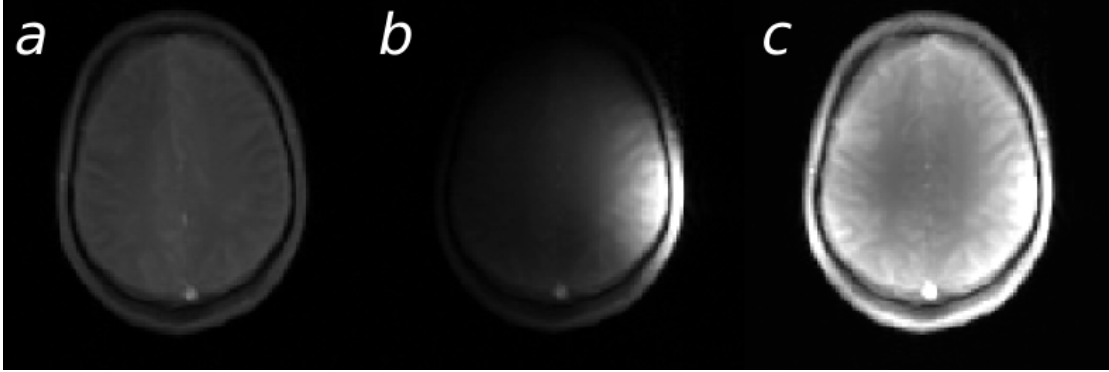


Figure 2.5: Sensitivity profiles of (a) VC, (b) SC, (c) AC coil. The VC coil has a very homogeneous sensitivity profile, whereas the SC has a distinct sensitivity profile. However, if several SC coils are combined like in an AC, the sensitivity profile is again homogeneous and a higher SNR is obtained. Bright gray values represent a high signal. The maps are equally scaled.

From the facts above one can deduce that VCs are best used for excitation, whereas SCs or ACs are preferably used for receiving the signal.

2.4 Signal Acquisition - From Excitation to the Spectrum

With the information about the basic principles of NMR and the setup of a medical NMR scanner, we can now depict the pathway of getting to an NMR spectrum. This includes the excitation, the relaxation, the acquisition of the signal, and the Fourier transform from the time to the spectral domain.

2.4.1 Excitation

In the microscopic picture, excitation can be seen as flipping more spins to the antiparallel state than there are in equilibrium, with a coherence among the phases of the individual magnetic moments. The latter means that the magnetic moments are no longer distributed equally in the x-y-plane, but a preferred direction is given. This can be seen in fig. 2.6.

If we want to describe excitation as a macroscopic phenomenon, we have to introduce an additional time dependent magnetic field $\vec{B}_1(t)$ with

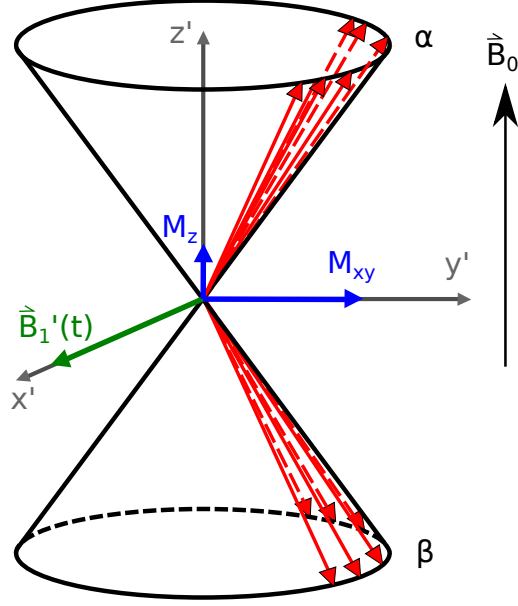


Figure 2.6: Excitation achieves a phase coherence between the magnetic moments. Hence, they are no longer equally distributed in the transverse plane, giving rise to a net transversal magnetization. The apostrophes denote the co-rotating frame of reference.

$$\vec{B}_1 = B_1 \cdot \begin{pmatrix} \cos(\omega t + \psi) & \sin(\omega t + \psi) & 0 \end{pmatrix}^T \quad (2.22)$$

The equation of motion, eq. (2.20), is changed to

$$\frac{d\vec{M}}{dt} = \gamma \vec{M} \times \begin{pmatrix} B_1 \cos(\omega t + \psi) & B_1 \sin(\omega t + \psi) & B_0 \end{pmatrix}^T \quad (2.23)$$

For reasons of convenience we set $\psi = 0$. If we transform to a frame of reference co-rotating with \vec{B}_1 (the axes and variables in this frame are denoted by apostrophes), the effective magnetic field is changed to

$$\vec{B}' = \begin{pmatrix} B_1 & 0 & B_0 - \frac{\omega}{\gamma} \end{pmatrix}^T \quad (2.24)$$

Effective means that this is not the magnetic field computed by transforming to the co-rotating frame of reference, but the field that is changed in a way, so that the form of eq. (2.20) remains, see [Badurek, 2010, p. 42] and [Haacke et al., 1999, p. 38 ff.]. Hence, the equation of motion in the co-rotating frame can be changed to

$$\frac{d\vec{M}'}{dt} = \gamma \vec{M}' \times \begin{pmatrix} B_1 & 0 & B_0 - \frac{\omega}{\gamma} \end{pmatrix}^\top \quad (2.25)$$

If we set the frequency of \vec{B}_1 to $\omega := \omega_0$ and use eq. (2.9), eq. (2.25) simplifies to

$$\frac{d\vec{M}'}{dt} = \gamma \vec{M}' \times \begin{pmatrix} B_1 & 0 & 0 \end{pmatrix}^\top \quad (2.26)$$

This case is called “on-resonance” and it describes a rotation of the magnetization around the x-axis, with an angular frequency of

$$\omega_1 := \gamma B_1 \quad (2.27)$$

Therefore, the motion of \vec{M} in the non-rotating frame of reference is a superposition of rotations around the z- and x-axis. By changing the phase ψ of \vec{B}_1 , the latter rotation axis can be changed to any axis in the x-y-plane.

The rotation of \vec{M}' in the on-resonance co-rotating frame of reference during excitation is shown in fig. 2.7(a) and the rotation in the resting frame of reference in fig. 2.7(b).

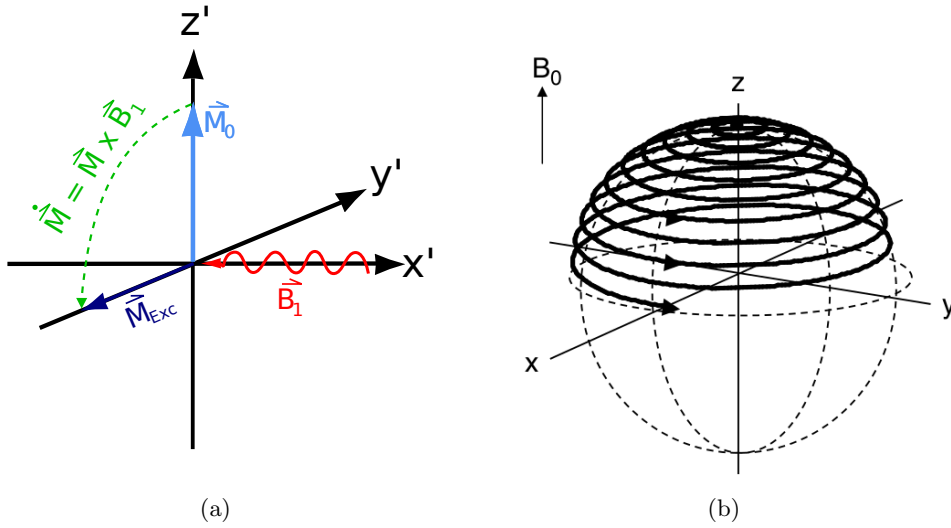


Figure 2.7: The motion of the magnetization in (a), the co-rotating frame of reference and (b), the static frame of reference. In (a), the magnetization rotates around the x' -axis towards the y' -axis according to eq. (2.26) and the right-hand-rule (provided that the RF pulse is applied along the negative x' -axis). In the static frame of reference, this motion is superimposed by the rotation around the z -axis according to eq. (2.20). (b) is taken from [de Graaf, 2007, p. 9]

Due to the rotation around the x-axis, the angle α of \vec{M} towards the z-axis is given by

2 Theoretical Background

$$\alpha = \omega_1 \tau = \gamma B_1 \tau \quad (2.28)$$

where τ is the time span in which the \vec{B}_1 -field is applied. In modern so called “Fourier-NMR”, the \vec{B}_1 field is applied as a short pulse with high intensity. α can be adjusted by either setting the amplitude B_1 , or the RF pulse duration τ . A combination of B_1 and τ leading to an angle of α is called α -pulse, e.g. 90° -pulse or 180° -pulse.

In the off-resonance case, the motion of \vec{M} becomes more complex, see [Haacke et al., 1999, p.47 f.] and [de Graaf, 2007, p. 233 ff.] for further information.

2.4.2 Relaxation

After the RF pulse is applied, the magnetization precesses in the x-y-plane, as depicted in fig. 2.8. However, the magnetization doesn't precess forever, but returns to the equilibrium state due to relaxation processes. There are two different kinds of relaxation processes, T1- and T2-relaxation.

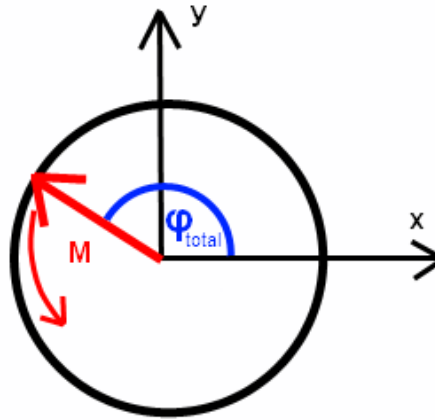


Figure 2.8: After excitation, the net transverse magnetization \vec{M}_{xy} is non-zero and rotates in the x-y-plane.

T1 Relaxation

T1-relaxation is the relaxation process affecting the z-component of the magnetization. The RF pulse excites the system to a non-equilibrium state by flipping some of the spins from the α -state to the β -state. As a result more spins are in the β -state compared to

2.4 Signal Acquisition - From Excitation to the Spectrum

the equilibrium state. The system approaches equilibrium again which results in β spins flipping back to the α -state. This happens the faster, the farther the system is deviating from the equilibrium. Mathematically spoken this is described by

$$\frac{dM_z}{dt} = -\frac{M_z - M_{equi}}{T1} \quad (2.29)$$

where $T1$ is the $T1$ -relaxation time constant and M_{equi} is the z -component of the magnetization in equilibrium. $T1$ is inverse to the rate with which the system approaches equilibrium after excitation.

The solution of eq. (2.29) can be easily computed as

$$M_z = k_1 e^{-\frac{t}{T1}} + M_{equi} \quad (2.30)$$

k_1 is a constant and determines the magnetization at the beginning of the relaxation process. Assuming this time point to be $t = 0$, k_1 can be computed as

$$k_1 = M(0) - M_{equi} \quad (2.31)$$

with $-M_{equi} \leq M(0) \leq M_{equi}$.

The spin ensemble gains energy during excitation, thus it loses energy during the relaxation process. This energy $E = \hbar\omega_0$ is transferred to the surrounding of the spin, the „lattice“ (this word comes from solid state NMR, in medical NMR there is no real lattice in soft tissues, the neighbouring magnetic spins are less coupled). This is why the $T1$ -relaxation is also called spin-lattice relaxation.

T2- and T2*-Relaxation

$T2$ - and $T2^*$ -relaxation describe the convergence of the transversal magnetization to its equilibrium state. The x - and y -components of the magnetization correspond to a phase coherence of the individual magnetic moments as described in 2.4.1. The phase coherence will be destroyed after some time due to two phenomena:

1. The intrinsic loss of phase coherence resulting from fluctuations of the local magnetic field, which in turn result from varying magnetic fields of the neighbouring spins [de Graaf, 2007, p. 112 ff.], [Badurek, 2010, p. 76 ff.], [Haacke et al., 1999, p. 56]. This is called $T2$ -relaxation.

2 Theoretical Background

2. Loss of phase coherence based on inhomogeneities of the external magnetic field \vec{B}_0 .

Both phenomena together are called T2*-relaxation.

Variations in the magnetic field lead to different precession frequencies of the magnetic moments $\vec{\mu}_i$. Thus, different $\vec{\mu}_i$ acquire different phases, leading to the destruction of phase coherence as depicted in fig. 2.9.

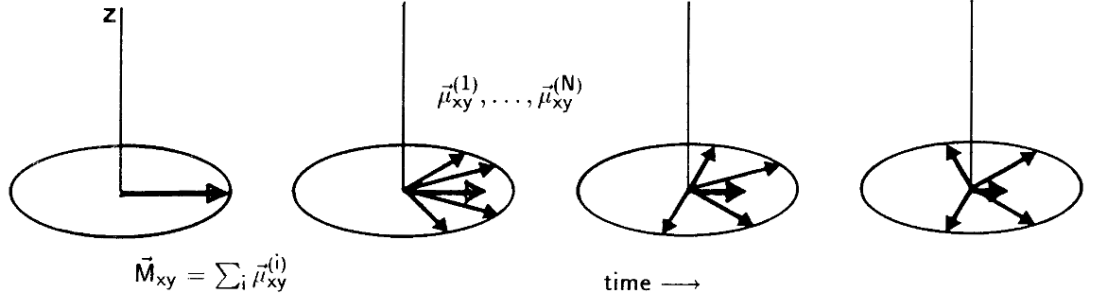


Figure 2.9: The phase coherence between the magnetic moments $\vec{\mu}_i$ decreases with time, leading to a fanning out of the magnetic moments. Thus the net transverse magnetization decreases with time. From: [Badurek, 2010, p. 51].

The T2*-relaxation is again faster, the more the system deviates from equilibrium (i.e. equally distributed spins in the x-y-plane), mathematically described as

$$\frac{dM_{xy}}{dt} = -\frac{M_{xy}}{T2^*} \quad (2.32)$$

Although the T1- and T2*-relaxation processes are independent of each other, the real measured decay of the transverse magnetization is always a combination of both, because there is no transverse magnetization left to measure if the magnetization is already fully T1-relaxed. Consequently, $T1 \geq T2 \geq T2^*$ is valid for all materials.

The solution of eq. (2.32) is

$$M_{xy}(t) = M_{xy}(0)e^{-\frac{t}{T2^*}} \quad (2.33)$$

where $M_{xy}(0)$ is the transversal magnetization at $t = 0$ and is restricted to

$$M_{xy}(0) \in [-M_{equi}, M_{equi}] \quad (2.34)$$

Bloch Equation

If we incorporate the relaxation processes in eq. (2.20), we obtain the so called Bloch equation:

$$\frac{d\vec{M}}{dt} = \gamma \vec{M} \times \vec{B}_0 - \left(\frac{M_x}{T_2^*} \quad \frac{M_y}{T_2^*} \quad \frac{M_z - M_{equi}}{T_1} \right)^\top \quad (2.35)$$

The solution of this equation is discussed in [Bloch, 1946]

2.4.3 Acquisition

The precessing magnetization is a time dependent magnetic field that will induce a voltage in an adjacent coil with matching resonance frequency. After receiving the RF signal in the coil, it is split into two components using a method called “signal demodulation”, see [Haacke et al., 1999, p. 102 ff.], amplified, and its frequency is adjusted to the reference frequency. The latter is equivalent to a transformation to the co-rotating frame of reference. It is convenient to write the components of the signal in a complex form

$$S_{Loc}(\vec{r}, t) = S_{Loc,x}(\vec{r}, t) + iS_{Loc,y}(\vec{r}, t) \quad \text{Cartesian form} \quad (2.36)$$

or

$$S_{Loc}(\vec{r}, t) = S_{Loc,0}(\vec{r}, t) \cdot e^{-\frac{t}{T_2^*}} \cdot e^{i(\omega_0 - \omega)t + i\varphi_{total}} \quad \text{Polar form} \quad (2.37)$$

with

$S_{Loc}(\vec{r}, t)$...	Local complex signal arising from position \vec{r}
$S_{Loc,x}$...	x component of the local signal
$S_{Loc,y}$...	y component of the local signal
$S_{Loc,0}$...	Magnitude of the local signal
ω	...	Frequency of the measured signal
φ_{total}	...	Total phase of the signal at t=0

However, the RF coils can never measure the local signal directly. Instead, the signal of the whole excited region V is measured, which mathematically corresponds to an integration over V. Therefore, eq. (2.37) has to be changed to

2 Theoretical Background

$$S(t) = \int_V S_{Loc,0}(\vec{r}, t) \cdot e^{-\frac{t}{T_2^*}} \cdot e^{i(\omega_0 - \omega)t + i\varphi_{total}} d^3r \quad (2.38)$$

In the following text, the term "phase" is identified with the phase at $t=0$.

The time dependent signal that is received during the T_2^* -relaxation process is called Free Induction Decay (FID). The magnetization precessing in the transverse plane, and the resulting FID with a single frequency ω and $\varphi_{total} = 0$ can be seen in fig. 2.10.

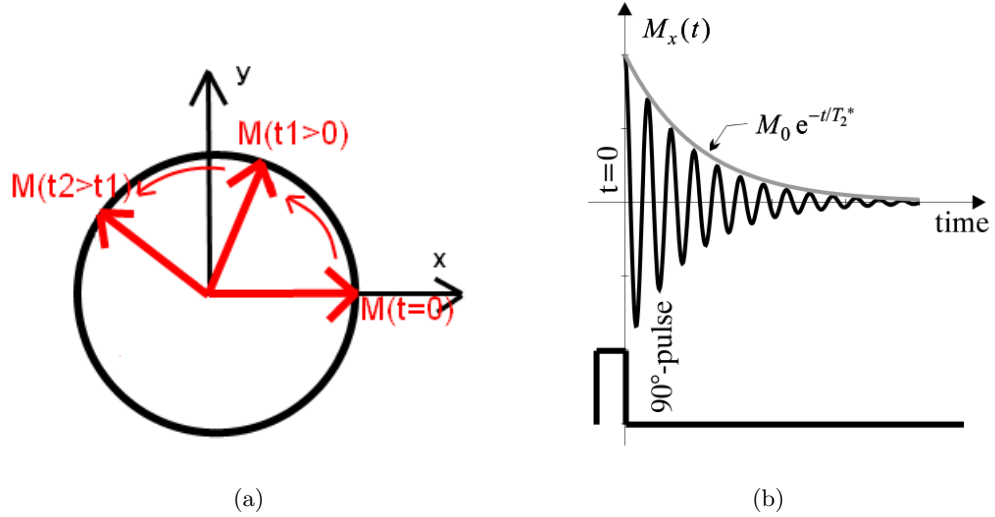


Figure 2.10: (a) After excitation, the magnetization precesses in the x-y-plane. This time dependent magnetic field causes a voltage in a nearby coil, which together with the T_2^* -decay results in the FID (b). Figure (b) is taken from [Badurek, 2010, p. 58]

In case of a time dependent frequency ω , we have to replace ωt by $\int \omega dt$ leading to a generalized equation

$$S(t) = \int_V S_{Loc,0}(\vec{r}, t) \cdot e^{-\frac{t}{T_2^*}} \cdot e^{i \int \omega_0 - \omega(t) dt} \cdot e^{i\varphi_{total}} d^3r \quad (2.39)$$

What happens to the FID if the phase is non-zero, i.e. the magnetization starts to precess with an angle φ_{total} inclined towards the x-axis? This is illustrated in fig. 2.11 for the angles 0° , 90° , 180° and 270° . As can be seen from this figure, the phase changes the starting point of the FID. The FID is no longer a cosine, but a mixed cosine and sine function.

Three main factors contribute to the total phase:

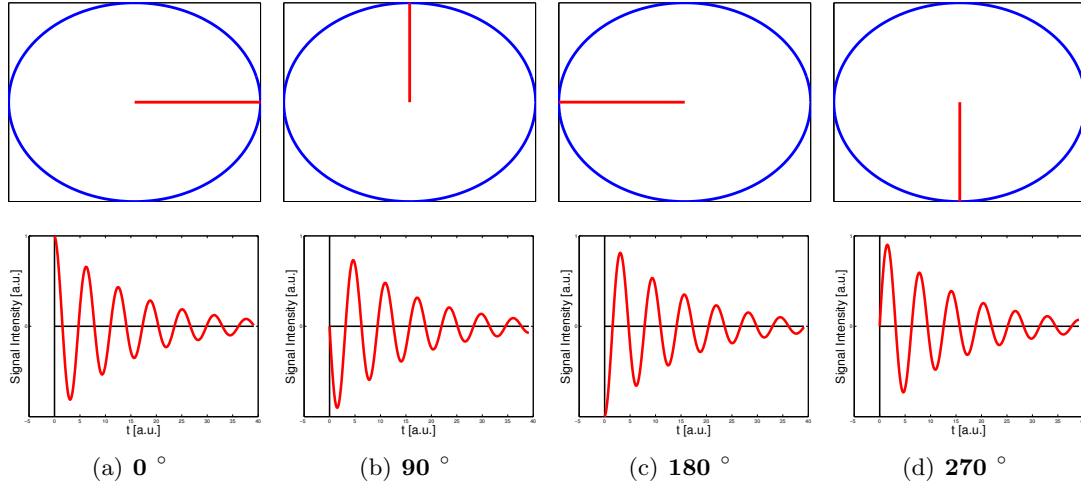


Figure 2.11: The magnetization vector (top) and the corresponding FID (bottom) for phases (a) 0°, (b) 90°, (c) 180° and (d) 270°. If the magnetization starts its precession not along the x-axis, but with a different angle to the x-axis, the starting point of the FID changes.

$$\varphi_{total} := \varphi_{anatomy} + \varphi_{PE} + \varphi_{inherent} \quad (2.40)$$

The first contribution is related to anatomical susceptibility variations resulting from boundaries between different tissues (e.g. tissue containing substantial iron depositions and its surrounding) or tissue and the air (e.g. in the nasal cavity), where the magnetic susceptibility changes rapidly.

The second contribution is caused by NMR localization techniques such as phase encoding.

The third contribution is due to artifacts of different origins. This includes B_0 -inhomogeneities, technical problems with RF pulses, gradients, and small timing errors.

2.4.4 Fourier Transformation & the Spectrum

The FID is an aperiodic (since it is damped by the T1- and T2*-decay), non-discrete function of time that is sampled in a discrete manner by the scanner. Therefore, one can analyze which frequencies are contained within the FID by performing a Discrete Fourier Transformation. Out of the discrete intensity function of time (i.e. the FID), a discrete intensity function of the frequency (i.e. the spectrum) is obtained. Because of the chemical shift, the different frequencies within the spectrum can be identified with different chemical groups of several metabolites.

2 Theoretical Background

In fig. 2.12, one can see two FIDs, one consisting of a single frequency component, the other with a superposition of two frequencies. Moreover the corresponding spectra are shown.

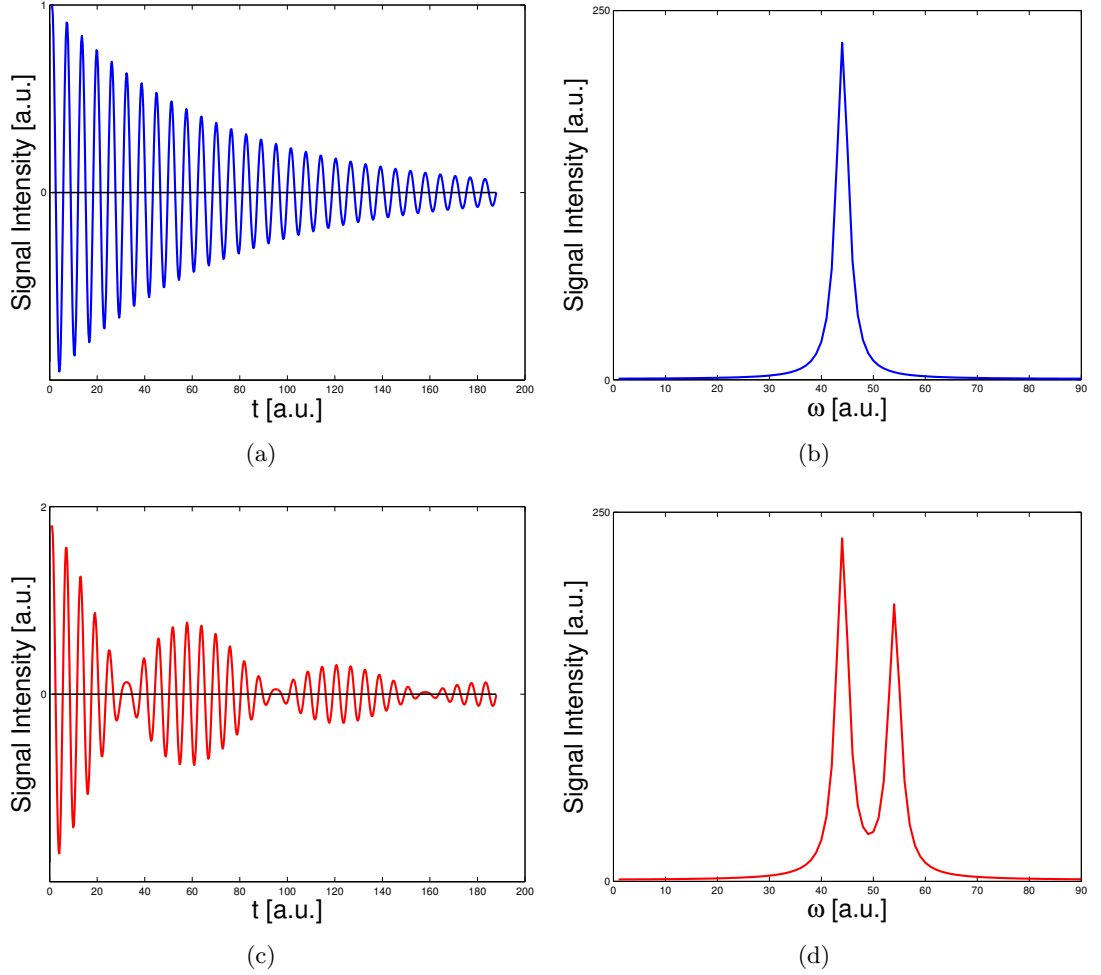


Figure 2.12: (a),(b): The spectrum of an FID with a single frequency consists of a single peak. (c),(d): Two superimposed signals with slightly different frequencies lead to two peaks in the spectrum.

What is the effect of a non-zero phase on spectra? Fig. 2.13 includes the effect of the phase on the real part of spectra. From this figure, one can see the problems of coil combination when doing spectroscopy: If two coils have a phase offset to each other, e.g. 180° , and both signals were summed up naively, the resulting spectrum would be zero. This is the reason why ACs are rarely used in spectroscopy but commonly in MRI. In

MRI, in most cases one is only interested in the magnitude of the signal. The combination of the coils can then be easily achieved by a weighted sum of the magnitudes of all coils, without taking phase information into account.

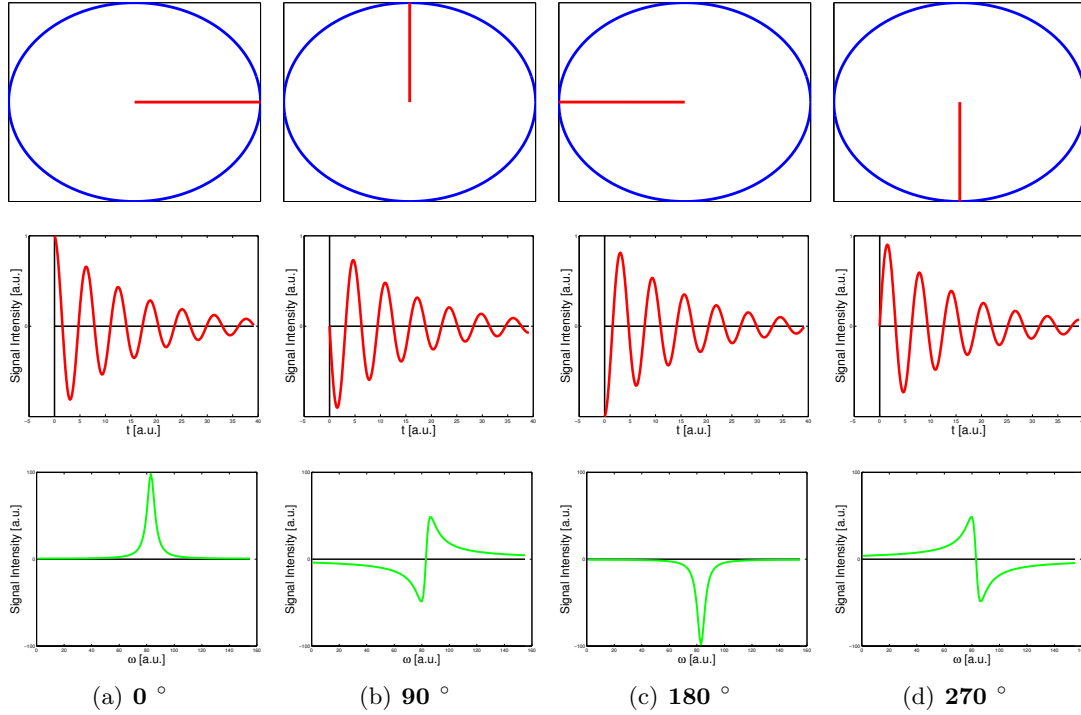


Figure 2.13: The effect of the phase on the magnetization vector (top), the FID (middle) and the spectrum (bottom) for phases (a) 0°, (b) 90°, (c) 180° and (d) 270°.

2.5 The Phase in Detail

The phase of the magnetization is caused by several reasons, as mentioned with eq. (2.40). In general the inherent phase $\varphi_{inherent}$ can be split into two components, one that is dependent on the chemical shift/frequency (first order phase) and one that is not (zero order phase). The origin of both will be explained below.

A phase that is the same for all voxels, coils and chemical shifts can be ignored, since its correction is easy and can be achieved by adding a constant value.

2.5.1 Zero Order Phase

Distance to the Coil

Although this phase contribution is very basic and easy to understand, hardly anything can be found about it in literature. Robinson et al. mention this effect: “The second problem is that individual receivers are subject to different, spatially varying, phase offsets [...]”. [Robinson et al., 2011] Nevertheless, since the following considerations are easily understood, they were incorporated in this thesis.

Consider a voxel with a distance r to the RF coil. Assuming that the RF pulse travels with a speed of c_{mat} within the matter, the pulse needs the time $T_{DistExc}$ to arrive at the voxel and excite its magnetization ($t := 0$ at emission of the RF pulse)

$$T_{DistExc} = \frac{r}{c_{mat}} \quad (2.41)$$

During this time, the magnetization of the voxel precesses with the Larmor frequency ω_0 , which leads to a phase of

$$\varphi_{Distance} = \omega_0 \cdot T_{DistExc} = \omega_0 \cdot \frac{r}{c_{mat}} \quad (2.42)$$

This phase contribution is dependent on the distance r to the coil, and therefore on the position \vec{r} of the voxel. As a result, two voxels with different distances to the coil will have different phases. This is illustrated in fig. 2.14.

Different Cable Lengths

If the cable lengths of the different AC channels differ from each other, the same effect as described above occurs. However, the resulting phase φ_{Cable} is not dependent on the voxel position, but on the channel.

B0 Inhomogeneities

Inhomogeneities of the main magnetic field \vec{B}_0 are another reason for the zero order phase [Reichenbach and Haacke, 2011, p. 51 ff.].

Depending on the local main magnetic field $\vec{B}_0(\vec{r})$, the magnetization of a voxel at \vec{r} precesses with a Larmor frequency given by eq. (2.9). If the magnetization is excited at $t = 0$, and measured with an acquisition delay at $t = t_{AD}$, the magnetization will have acquired a phase of

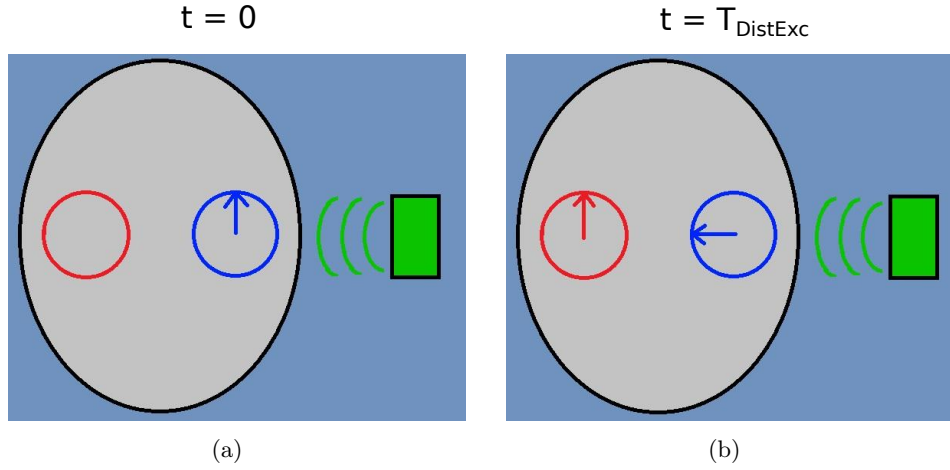


Figure 2.14: (a) Since the RF pulse needs more time to travel from the coil to the more distant voxel, this voxel is still not excited at the time when the closer one is. (b) At the time $T_{DistExc}$ when the distant voxel is excited, the closer one has already acquired some phase, leading to a phase difference between both voxels.

$$\varphi_{Inhomo} = \gamma B_0(\vec{r}) t_{AD} \quad (2.43)$$

Thus, inhomogeneities in \vec{B}_0 introduce another phase contribution that is dependent on the position of the voxel. In fig. 2.15, this effect is illustrated for two different positions with magnetic field strengths \vec{B}_0 and \vec{B}_0^* .

2.5.2 First Order Phase

Different chemical compounds have different chemical shifts and therefore different frequencies. If we measure two chemical compounds with frequencies ω_1 and $\omega_2 > \omega_1$ at time t_{AD} after excitation, compound 2 acquires a higher phase during the same time. This is illustrated in fig. 2.16. The phase φ_{AD} of an chemical compound with frequency ω caused by the acquisition delay t_{AD} is given by

$$\varphi_{AD} = \omega t_{AD} = \omega_0 t_{AD} + (\omega - \omega_0) t_{AD} \quad (2.44)$$

Neglecting the first term which is a simple constant, using eq. (2.14), and defining φ_1 as the first order phase in [rad/ppm], we obtain:

$$\varphi_{AD} = \delta \frac{\omega_0}{10^6} t_{AD} =: \delta \cdot \varphi_1 \quad (2.45)$$

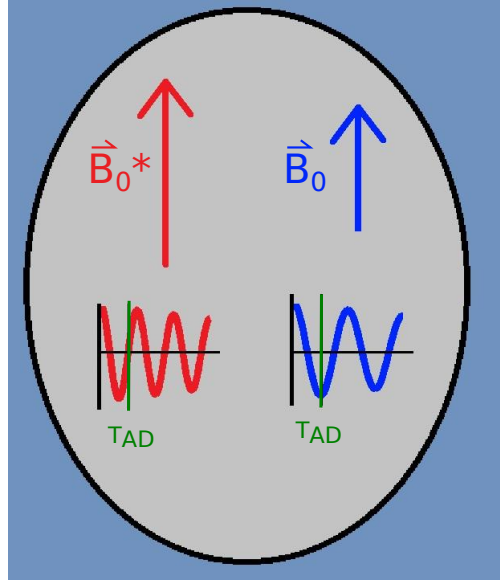


Figure 2.15: The magnetization at \vec{B}_0^* precesses with a higher frequency than the one at \vec{B}_0 , leading to a phase difference at the acquisition delay time t_{AD} (i.e. the beginning of the acquisition).

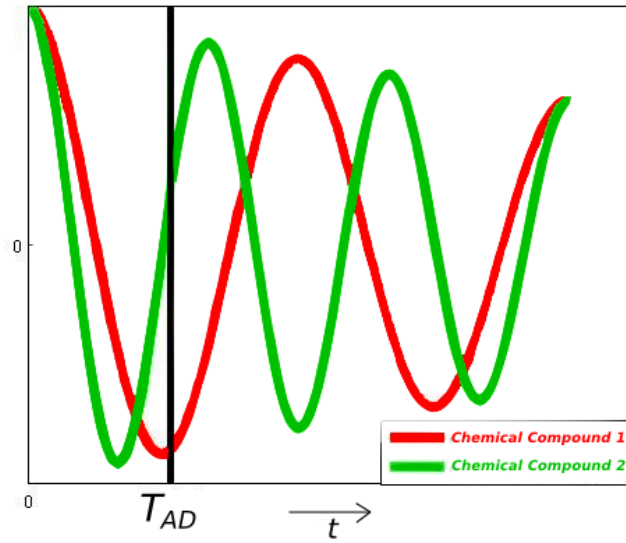


Figure 2.16: Different chemical compounds have different Larmor frequencies according to eq. (2.12). If the experiment starts at time t_{AD} , the magnetization with the higher Larmor frequency (green) will have acquired a higher phase than the one with the lower frequency (red). This leads to a phase component that is dependent on the frequency/chemical shift.

The acquisition delay can be caused by an imperfect timing of the read out with the ADC. Moreover, all FID-based sequences have a certain acquisition delay, since it is not possible to measure directly after excitation. This is simply because the excitation pulse and the localization gradients require a certain time.

The effect of the first order phase is illustrated in fig. 2.17. Comparing with fig. 2.2, the peaks of tCr and tCho look downwards as a result of the first order phase. NAA on the other hand looks upwards as the acquisition delay was chosen to achieve so.

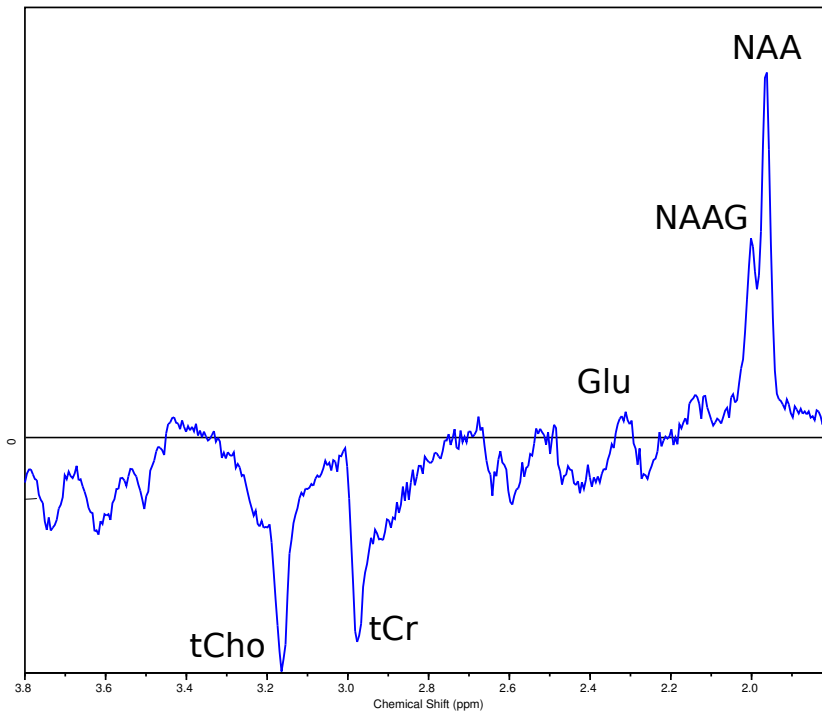


Figure 2.17: The effects of the first order phase illustrated by a spectrum acquired of a healthy volunteer at 7T. It is clearly visible that depending on the position on the chemical shift scale, the phase is different for each peak.

2.6 Localization

Without any localization, the magnetization of the whole excited volume contributes to the signal. This results in several disadvantages.

One drawback is the lower information content of signals acquired without any localiza-

2 Theoretical Background

tion. Moreover, the quality of spectra improves dramatically if the signals originate from a smaller region. This is related to B_0 -inhomogeneities, since the variations in B_0 are lower across smaller volumes. Therefore, localization results in better spectral separation of metabolite resonances. Additionally, non-localized spectra can be contaminated by signals that are not of interest. As an example, the spectrum of a brain would be highly contaminated with the signals from the extracranial lipids surrounding the brain. In fig. 2.18, an example of a non-localized spectrum and a localized one is given.

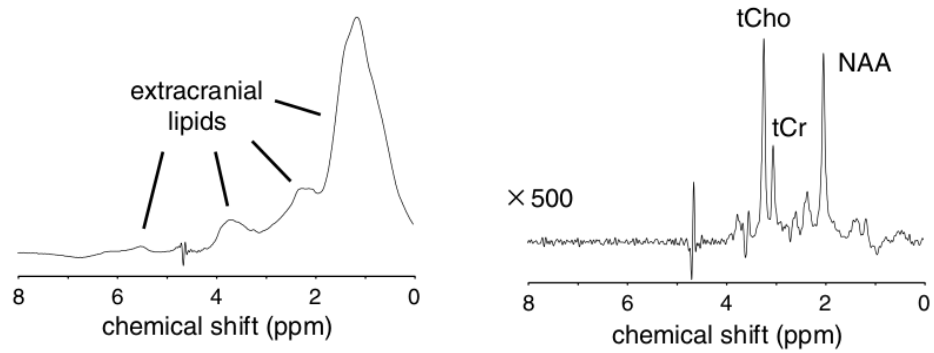


Figure 2.18: (a) A spectrum acquired of a newborn piglet without any localization. The signals of the extracranial lipids overlay the actual spectrum. (b) The same spectrum acquired with a single-voxel localization method called “PRESS”. Distinct metabolite peaks are visible and can be quantified. From: [de Graaf, 2007, p. 298]

There are several methods to acquire spatial information of the signal. All common methods use additional magnetic fields induced by the gradient coils.

Exciting only the magnetization of a certain volume, or destroying the x-y-magnetization outside a volume, e.g. a single voxel or a slice, is one commonly used method. Acquiring signal from a single voxel is only used in MR Spectroscopy, since one can solely get information of one position at a time. This type of MR Spectroscopy is called “Single Voxel Spectroscopy”. For further information on that topic see [de Graaf, 2007, p. 297 ff.].

Contrary to single voxel spectroscopy, a whole matrix of spectra is acquired in MRSI by combining spectroscopy with localization techniques of MRI. The basis of MRI is slice selection, frequency and phase encoding. In the latter two, spatial information is encoded in the frequency or phase, respectively. Slice selection is a method to excite the magnetization only of a single slice. All three methods are explained below, but at first the effects of the gradient field have to be discussed.

2.6.1 The Effects of Gradients

The gradient coils add an additional magnetic field along the z-axis that is linearly dependent on the x-, y- or z-axis, i.e.

$$\vec{G} := \left(\frac{\partial B_z}{\partial x} \quad \frac{\partial B_z}{\partial y} \quad \frac{\partial B_z}{\partial z} \right)^\top \quad (2.46)$$

Be aware that the additional magnetic field \vec{B}_G , that results from the gradients, points along the z-direction, only the change of the z-component is along the x-, y- or z-component. This is illustrated in fig 2.19.

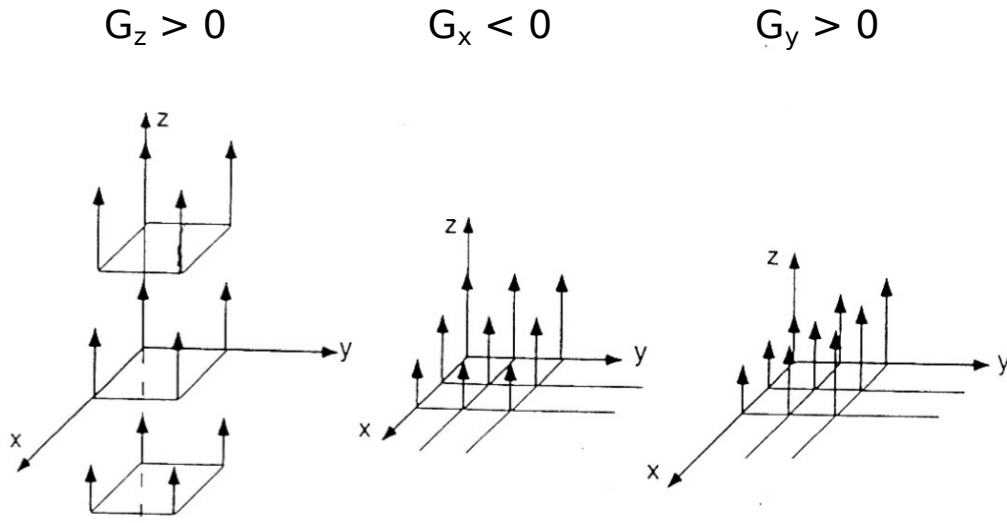


Figure 2.19: The magnetic field caused by a gradient in z-direction (left), x-direction (middle) and y-direction (right). The length of the arrows represent the field strength. From: [Gurker, 2011]

The magnetic field $\vec{B}_G(\vec{r})$ caused by the gradients is given by

$$\vec{B}_G(\vec{r}) = \langle \vec{r}, \vec{G} \rangle \cdot \vec{e}_z \quad (2.47)$$

As a result, the Larmor frequency has to be changed to

$$\omega(\vec{r}, t) = \gamma(B_0 + B_G(\vec{r}, t)) = \gamma(B_0 + \langle \vec{r}, \vec{G}(t) \rangle) \quad (2.48)$$

where B_G is the norm of \vec{B}_G .

2.6.2 Slice Selection

The gradients achieve a linear correspondence between the spatial position and the frequency. Thus, by exciting a certain frequency range, only the corresponding spatial positions are excited. A single slice can be excited by applying a frequency selective RF pulse simultaneously with a gradient in one direction. Assuming that an x-y-slice should be excited, a z-gradient has to be applied. Each z-position corresponds then to a certain frequency, determined by the z-gradient. Therefore only these z-positions get excited that correspond to a frequency within the frequency excitation range (i.e. bandwidth) of the RF pulse. This is depicted in fig 2.20 for two different gradient strengths.

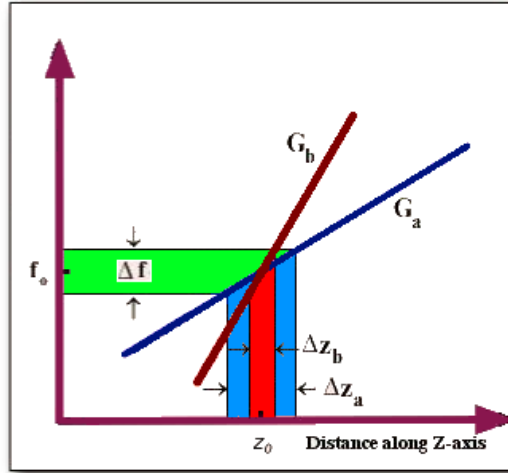


Figure 2.20: Exciting only within the frequency range $f_0 \pm \Delta f$ translates to excitation of the z-positions $z_0 \pm \Delta z_a$ (blue gradient) and $z_0 \pm \Delta z_b$ (red gradient). As can be seen by this figure, changing f_0 determines the position of the excited slice, whereas Δf determines the thickness of the slice for a given gradient strength. Image recolored, taken from: “KieranMaher”, 10.11.2006, available at Wikimedia Commons (URL: http://en.wikibooks.org/wiki/Basic_Physics_of_Nuclear_Medicine/MRI_%26_Nuclear_Medicine), no License, Time of access: 31.03.2012

2.6.3 Frequency Encoding

Frequency encoding uses the gradient coils to encode the spatial position within the frequency. The gradient has to be applied during the read out.

As described by eq. (2.48), the Larmor frequency is dependent on the position if gradients are applied. Neglecting the phase, the signal intensity $S(t)$ is given by

$$S(t) = \int_V S_0(\vec{r}, t) \cdot e^{it(\omega_0 - \int \omega(t) dt)} d^3r \quad (2.49)$$

see eq. (2.38).

If we replace ω with eq. (2.48) and use eq. (2.9), we obtain

$$S(t) = \int_V S_0(\vec{r}, t) \cdot e^{-i\gamma \langle \vec{r}, \int \vec{G}_{freq}(t) \rangle dt} d^3r \quad (2.50)$$

where \vec{G}_{freq} is the frequency encoding gradient. We define the k-vector as

$$\vec{k}(t) := \gamma \int \vec{G}(t) dt \quad (2.51)$$

and the x-direction as the direction along the frequency encoding gradient. Using these definitions and restricting the spatial dependence of the signal in x-direction, eq. (2.50) simplifies to

$$S(k_x, t) = \int_{V_x} S_0(x, t) \cdot e^{-ixk_x} dx \quad (2.52)$$

which is exactly the 1-dimensional Fourier transformation of the wanted signal $S_0(x, t)$. Hence, the signal $S(x, t)$ as a function of x can be retrieved by performing an inverse Fourier transformation on $S(k_x, t)$.

2.6.4 Phase Encoding

By applying another gradient in y-direction, the frequencies are as well dependent on the position along this direction. The trick is now to apply this gradient **before** data acquisition for a certain time period t_{PE} . Since some spins are rotating faster during this time, these will acquire a higher phase than others. This phase is described by

$$\varphi_{PE}(y, t) = \int_0^{t_{PE}} \omega(y, t) dt = \int_0^{t_{PE}} y \cdot G_y(t) dt = y \cdot k_y(t_{PE}) \quad (2.53)$$

where eq. (2.48) and (2.51) were used and a constant phase was neglected. If we recover the phase φ_{PE} which we neglected in eq. (2.52) again, and use eq. (2.53), we obtain

$$S(k_x, k_y, t) = \int_{V_{x,y}} S_0(x, y, t) \cdot e^{-i(xk_x + yk_y)} dx dy \quad (2.54)$$

2 Theoretical Background

which is the two-dimensional Fourier transformation of the wanted signal. The signal $S(x, y, t)$ can again be computed by performing a two-dimensional inverse Fourier transformation, leading to a two dimensional image.

2.6.5 k-Space

The k-space is defined as the set of all k-vectors \vec{k} .

It can be filled in a variety of ways. The easiest way is to fill it line by line by exciting the magnetization, jumping to a position k_y in y-direction using phase encoding, and for that fixed k_y , acquiring the whole line in x-direction using frequency encoding. Then, the whole procedure is repeated with a different k_y value (i.e. different phase encoding gradient strength) until the whole k-space is measured. This procedure is illustrated in fig. 2.21.

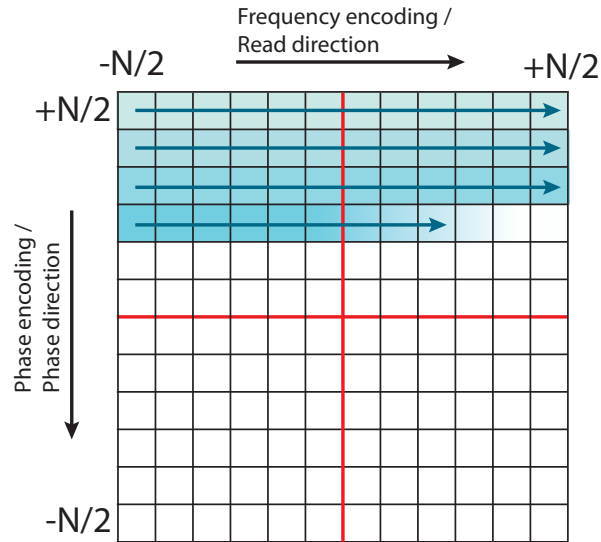


Figure 2.21: In each repetition of the sequence, a line in frequency encoding direction is read in (blue arrows). The phase encoding gradient strength is varied with every repetition, corresponding to different values along the phase encoding direction. Hence, the whole k-space is filled line by line. Figure taken from [Horn, 2012], with kind permission of Christian Horn.

As an example, we could acquire 512 different k_y -values and for each of these, 256 k_x -values, leading to a 512x256x1 matrix in k-space. The Fourier transformation in k-space matrix results in a 512x256x1 matrix in the "image space".

In fig. 2.22 the magnitude and the phase of a data set in k-space and in "direct space" can be seen.

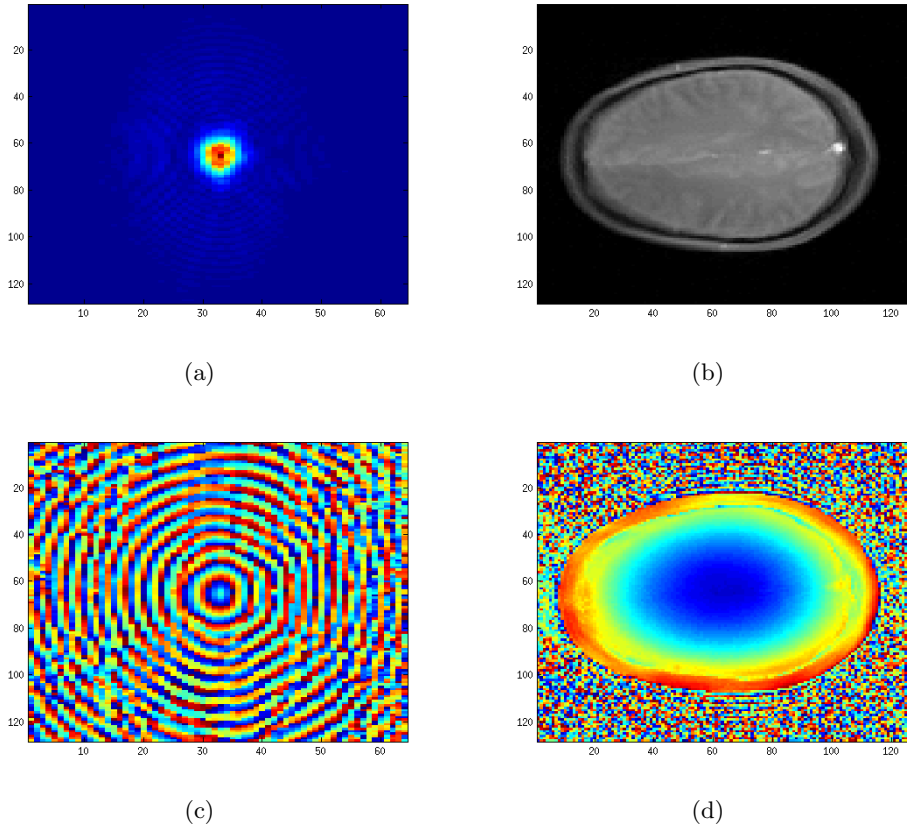


Figure 2.22: The magnitude (a) and phase (c) of an volunteer acquisition in k-space, and the magnitude (b) and phase (d) in the image space after Fourier transformation. The k-space figures are zoomed in with an factor of 2. Red colors represent high values and blue represent low values.

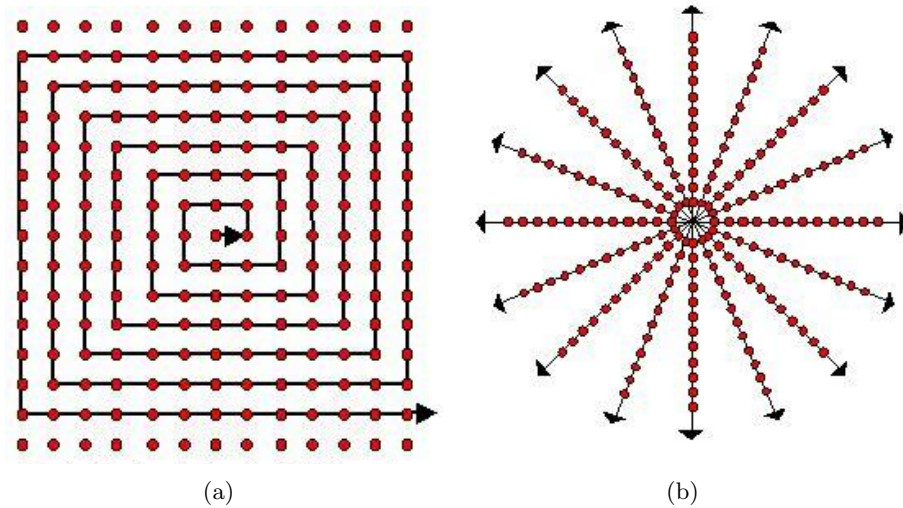


Figure 2.23: k-space acquisition using a pseudo-spiral (a), and a radial scheme (b). From: Stanislav Sýkora, 22.03.2006, available at <http://www.ebyte.it/library/educards/mri/K-SpaceMRI.html>, doi: 10.3247/SL1Mri05.001, Time of access: 31.03.2012

Other examples for acquiring the k-space are spiral, pseudo-spiral, radial pathways, and many more. The latter two are shown in fig. 2.23.

2.6.6 MR Imaging vs MR Spectroscopic Imaging

Typical MRI sequences use both, frequency and phase encoding to acquire spatial information. As a result, an image is obtained, whose contrast is determined by T1 and T2-relaxation times or spin density variations between different tissue types.

On the other hand, in MRSI a whole FID is measured for each spatial position in order to acquire spectral information. The acquisition of spectral information with common methods prohibits the usage of frequency encoding. Instead, the localization has to be performed using the much slower phase encoding. The reason for this slowness is founded in the necessity to repeat the whole sequence of excitation, slice selection, application of the phase encoding gradient and other elements for each k-point. As an example, the acquisition of a 64x64 MRSI matrix with slice selection in the third dimension takes 30 minutes, whereas the acquisition of an MRI matrix of the same size takes less than 1 s. In order to reduce the acquisition time of MRSI, slice selection is widely used.

2.7 Sequences

The process of transmitting RF power for excitation, the reception, localization, and the destruction of remaining signal is repeated numerous times during each NMR experiment and is termed “MR Sequence”. An MR Sequence is therefore a sequential arrangement of RF pulses, gradients, the read out of the signal and the timing between those elements. The symbols used for the individual elements when depicting a sequence are shown in fig. 2.24.

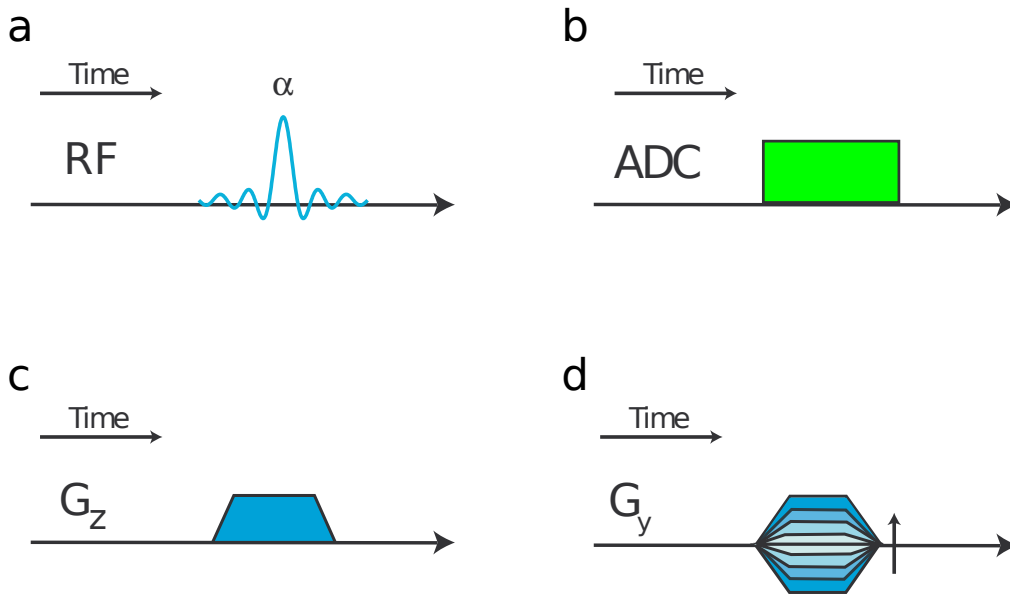


Figure 2.24: The elements a typical sequence consists of. (a): Sinc RF pulse, (b): Acquisition window of the ADC, (c): A Gradient, (d): Phase encoding gradient. In the latter, the different lines and the arrow emphasize the increase of the phase encoding gradient with every repetition of the signal. Based on an illustration by Christian Horn, [Horn, 2012].

Every MR Sequence for medical purposes consists of five parts: The preparation, e.g. for suppressing the water signal, the excitation, the localization, the acquisition and the dephasing part for destroying all remaining signal and to prepare for the next repetition.

In the following chapter, four example sequences are described: (i) the simplest possible sequence, (ii) the simplest possible spin-echo sequence, (iii) a localized gradient echo sequence, and (iv) an FID-based MRSI sequence. The last two sequences are those that were used in the experimental part of this diploma thesis.

2.7.1 The Simplest Possible Sequence

The simplest sequence is shown in fig. 2.25. It consists of a 90° -pulse that excites

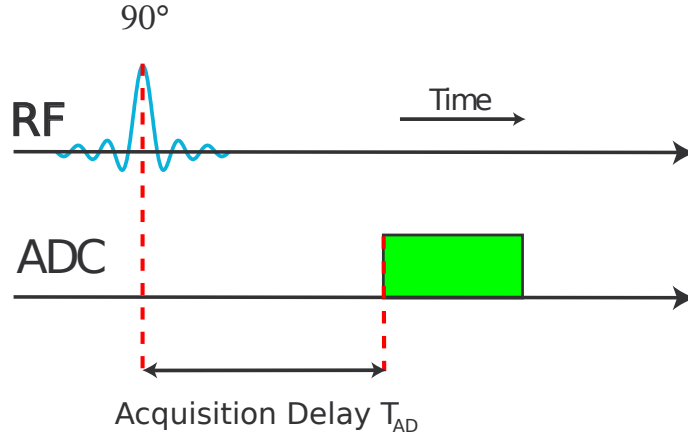


Figure 2.25: Simplest possible MR Sequence consisting of an RF-pulse, a short acquisition delay t_{AD} and the acquisition of the signal with the ADC. Based on an illustration by Christian Horn, [Horn, 2012].

the magnetization without localization, a short acquisition delay time t_{AD} , and the acquisition of the signal with the ADC.

The result is an FID consisting of complex data points, e.g. 1024. A spectrum can be computed out of this signal, nevertheless the spectrum will be distorted as described in section 2.6, since no localization is performed.

2.7.2 The Simplest Possible Spin Echo Sequence

The simplest possible spin echo sequence is shown in fig. 2.26. The first element is a 90° -pulse to excite the magnetization without localization. During the subsequent time $TE/2$ (half of the Echo Time), the individual magnetic moments μ_i fan out due to $T2^*$ -relaxation. However, at time $TE/2$, a 180° -pulse is applied which refocuses the magnetic moments, producing an echo at time TE . For further information, see [de Graaf, 2007, p. 37 ff.] and [Badurek, 2010, p. 86 ff.].

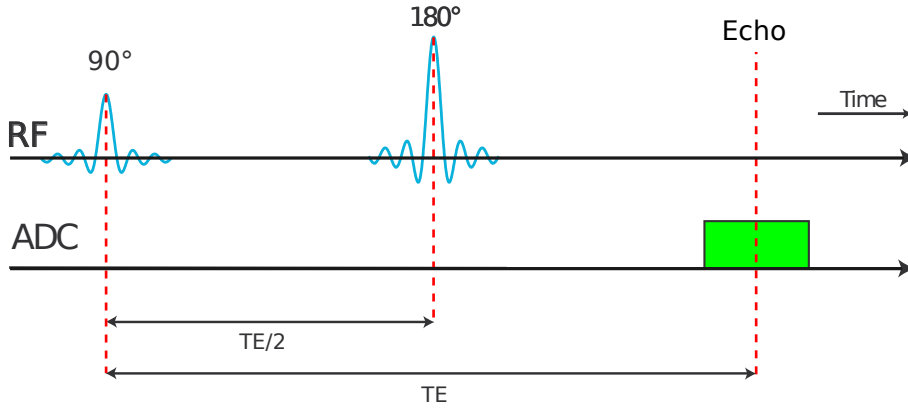


Figure 2.26: The simplest possible spin echo sequence. A 90° -pulse excites the magnetization. The consequent 180° -pulse refocuses the magnetization at time TE , leading to a spin echo which is acquired with the ADC. Based on an illustration by Christian Horn, [Horn, 2012].

2.7.3 The Gradient Echo Sequence

A two-dimensional Gradient Echo (GRE) sequence with slice selection in the third dimension is shown in fig. 2.27. This is a commonly used GRE sequence and it was also used in this work.

First, an excitation pulse (excitation angle of α) and a slice selection gradient in z -direction are applied at the same time. The excitation pulse only excites a certain range of frequencies. These two elements together lead to a selective excitation of a single slice. The slice selection gradient introduces an additional, unwanted phase, hence a rephasing gradient with the same area, but opposite sign has to be applied.

The next element is the phase encoding gradient, which leads to different phases along the y -axis. The multiple lines emphasize that for each repetition of the sequence, the phase encoding gradient strength is incremented. Each of these corresponds to a line in k -space.

The preparation gradient for frequency encoding is applied in x -direction. At the end of this gradient, all magnetic moments have acquired different phases depending on their x -position. Since this destroys the phase coherence, the total transverse magnetization is zero.

The following read out gradient has the opposite sign as the preparation gradient and twice the area. It therefore undoes the effect of the preparation gradient and rephases the magnetic moments. At the time TE , when the pre- and frequency encoding gradients have the same area A , all magnetic moments are rephased and the net magnetization

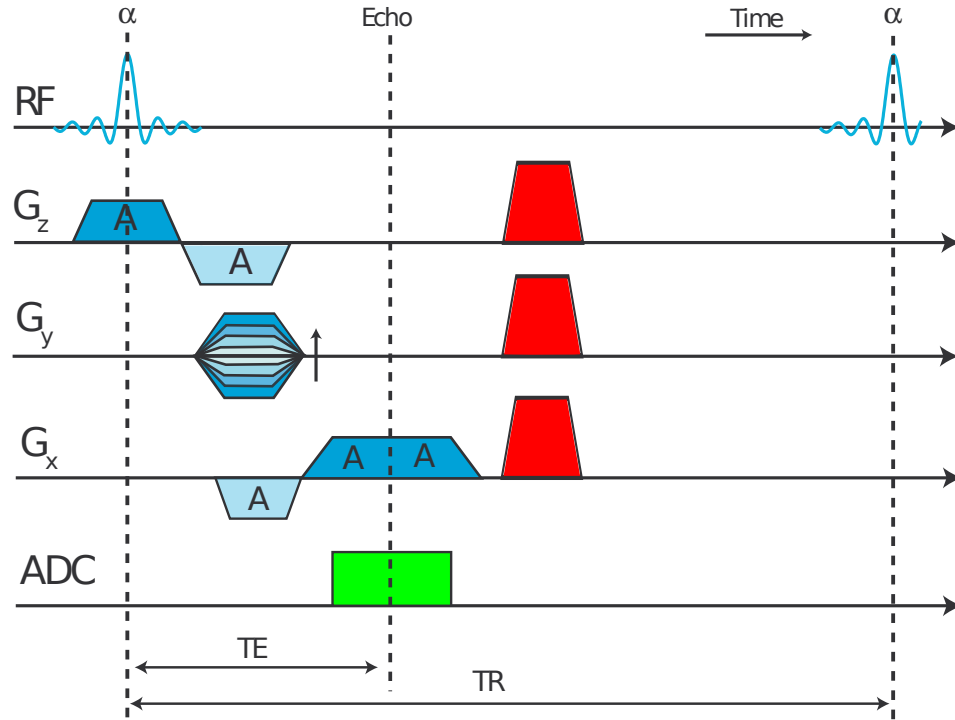


Figure 2.27: A standard GRE sequence consisting of an excitation pulse, a slice selection gradient (blue, z-direction), rephasing gradient (light blue, z-direction), phase encoding gradient in y-direction, prephasing gradient (light blue, x-direction), frequency encoding gradient (blue, x-direction), the acquisition with the ADC (green block), and the crusher gradients (red). The A's in the gradients indicate that the areas of the gradients are the same. Based on an illustration by Christian Horn, [Horn, 2012].

in the x-y-plane is therefore maximal. An echo (in this case a gradient echo) is created. Then the magnetization decreases again due to dephasing caused by the frequency encoding gradient.

During the whole read out period, the signal is measured by the ADC. Each measured point corresponds to one k-space point, and the whole echo to a k-space line.

After the readout, one has to either wait until the magnetization is fully T1-relaxed, or apply a “crusher gradient” that destroys all magnetization to avoid artifacts in the next repetition. Such a crusher gradient was used in the GRE sequence in this diploma thesis.

The time between the center of the excitation pulse and the center of the echo is called echo time (TE), the time between two repetitions of the sequence repetition time. The longer the TE, the more the magnetization relaxes due to T2*-relaxation. Since tissues have different T2 constants, one can get a higher or lower contrast between different tissue types by changing the TE. Although a gradient echo refocuses the magnetization, it does not undo the effects of B_0 -inhomogeneities, nor first order phasing errors. In this respect, a GRE with echo time TE exhibits the same behavior as the acquisition with an FID after an acquisition delay of the same duration.

2.7.4 FID-Based MRSI Sequence

In fig. 2.28 a scheme of the MRSI sequence that was used in this work is illustrated.

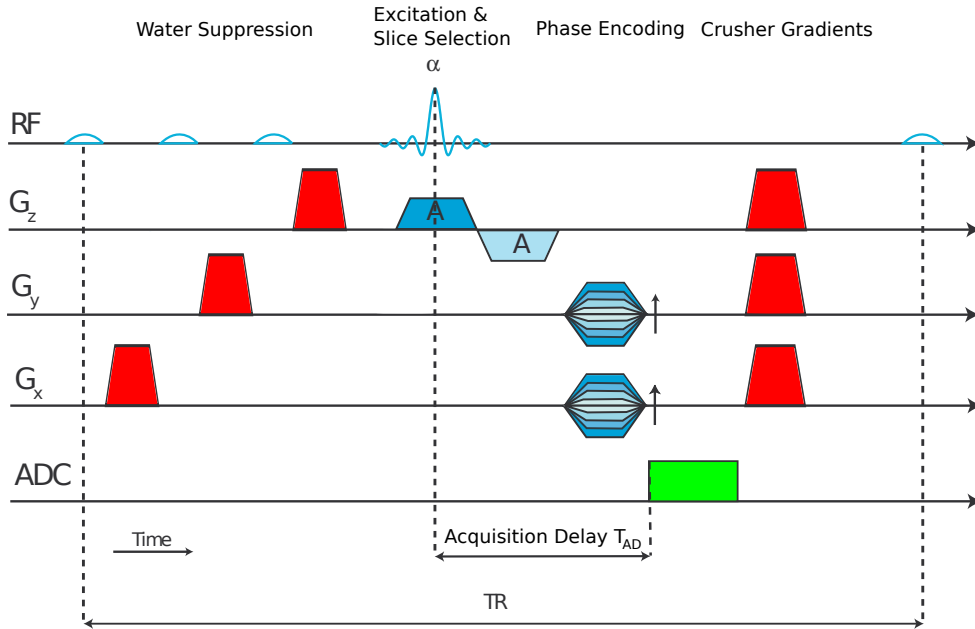


Figure 2.28: Scheme of the FID-based MRSI sequence used in this work. The water signal is suppressed by exciting only the frequency range of water followed by a crusher gradient to destroy the magnetization of the water. After the water suppression block, the magnetization of a single z-slice is excited by an excitation pulse and a simultaneous gradient in z-direction (blue gradient). The dephasing of the latter is undone by the rephasing gradient (light blue gradient). The phase encoding is done in x- and y-direction. Subsequently, the ADC block (green) measures the signal with an acquisition delay of t_{AD} . Finally, the crusher gradients destroy all remaining magnetization. Based on an illustration by Christian Horn, [Horn, 2012].

2 Theoretical Background

Since in MRSI we are normally not interested in the detection of water signal, the first part of the MR sequence is dedicated to water suppression. Water suppression can be achieved by repeated frequency selective excitation of the water resonance and subsequent destruction of this signal by a strong dephasing gradient. To read more about this type of water suppression called WET, see [Ogg et al., 1994].

After water suppression, the spins of all metabolites get excited within a single slice using a frequency selective excitation pulse and a gradient at the same time. In the next step, the phase encoding gradients are applied in the remaining two directions. In this case no frequency encoding is performed. Afterwards, the signal is read out by the ADC. Finally, crusher gradients are used to destroy all remaining magnetization and to prepare for the next phase encoding step.

2.8 Postprocessing

After the signal is measured, some post processing steps are either necessary or can be used to improve the appearance or to change the quality of the spectra.

2.8.1 Fourier Transformation

A very important post processing step is the Fourier transformation that was already described in section 2.4.4. It is crucial to understand that the Fourier transformation is used for two different purposes in MRSI: Once for retrieving spatial information, i.e. to get from the k-space to the image space as it is also used in MRI. Secondly, for retrieving spectral information, i.e. to get from the time domain to the spectral domain. The spatial Fourier transformation is always performed because very few people can extract information out of an k-space image. The second one is necessary for programs that analyze the data in the spectral domain. Nevertheless, some programs can analyze the FID directly, in such cases the spectral Fourier transformation is not necessary.

2.8.2 Apodization

Apodization is the weighting of the FID with different filter functions. The most common apodization method weights the beginning of the FID stronger than the end by multiplying the FID with an exponential filter function $e^{-\frac{t}{T_w}}$, $T_w > 0$. This can be seen as artificially increasing the T2*-relaxation time. The end of the FID contains mostly noise. Thus, weighting the end of the FID less increases the SNR. However, since signals with very close frequencies only differ at the end of the FID, the signals become less

discriminable. The effect on spectra is therefore a broadening of the peaks, i.e. the linewidth increases. Using the opposite filter function, $T_w < 0$, reverses the effects.

Other filter functions like Gaussian or Lorentzian functions can be used to optimize the effects according to ones needs [de Graaf, 2007, p. 20 ff.].

2.8.3 Zero Filling

When Fourier transforming an FID of e.g. 1024 time points, a spectrum with an identical number of spectral points is obtained. Although the FID may comprise the information to discriminate between two similar frequencies, they might be invisible in the spectrum, simply because not enough spectral points are available to represent the close peaks separately. In such cases, zero filling can enhance the appearance of the spectrum.

When performing zero filling, one simply adds zeros at the end of the raw time domain data. This results in an interpolation of the spectrum after Fourier transformation. Although the appearance can sometimes be improved strongly like in fig. 2.29, it is obvious that zero filled data bears no additional information. Zero filling can be performed in k-space as well as in the time domain. Further information can be found in [de Graaf, 2007, p. 25 ff.].

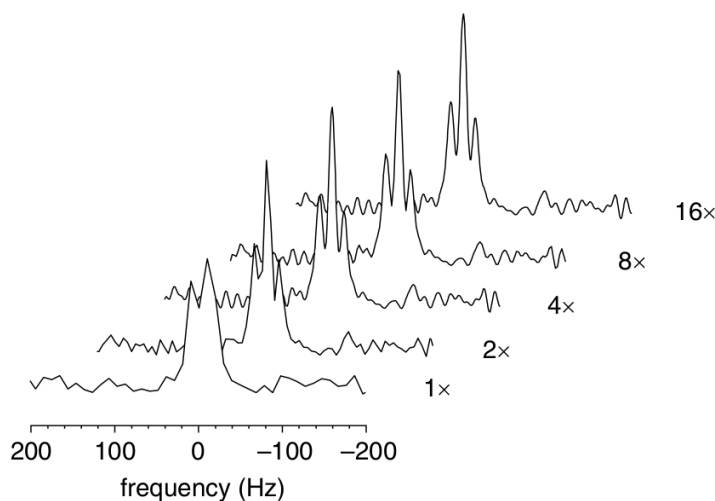


Figure 2.29: Without zero filling (1x) only two peaks are visible. Performing zero filling by redoubling the time points (2x) reveals another peak. Using higher multiplication factors further improves the appearance slightly. From: [de Graaf, 2007, p. 25]

2.8.4 Fitting the Spectroscopic Data

Fitting the spectroscopic data is typically one of the last postprocessing step. Nevertheless it has to be discussed prior the phasing of the signals, which is performed before the fitting process, since its understanding is necessary for the first order phase corrections as they were done in this thesis.

A certain biological tissue consists in most cases of the same types of metabolites, resulting in similar spectra. With the knowledge about these chemical compounds, the NMR spectrum of each metabolite can be simulated or measured in a phantom. The set of all these metabolite spectra is called basis set.

Fitting spectroscopic data is the attempt to get the best match between the basis set and the measured spectrum. As a consequence the metabolic concentrations can be determined. One way to calculate these concentrations is to use a linear combination model like it is done by the program LCModel (see [Provencher, 2012] for information about the program). In this case, the measured spectrum is considered as a linear combination of the individual metabolite signals. The amplitude and the linewidth of each basis set compound, as well as the frequency shift, the phase and other parameters are calculated to get the best match between the basis set and the spectrum. In fig. 2.30 an example of a measured spectrum that was fitted with a basis set, and some of these compounds are given.

The scaling factors the basis set components have to be multiplied with in order to agree with the measured spectrum are computed by a complex algorithm, see [Provencher, 1993]. The area under the resonance peaks is determined, which corresponds to the concentration of the metabolites in the tissue. The common practice is to compute the ratios of metabolic concentrations (e.g. ratios to creatine). However, if a suitable reference compound is available, so-called absolute concentrations are sometimes derived, by assuming the concentration of one metabolite to be fixed (e.g. by assuming the creatine concentration to be 6 mM). In pathologies this is often not the case, and external referencing phantoms may be useful, but pose different problems to absolute quantification.

The reliability of the concentration estimation is evaluated by the so called Cramer-Rao Lower Bond (CRLB), which is a lower bound for the standard deviation.

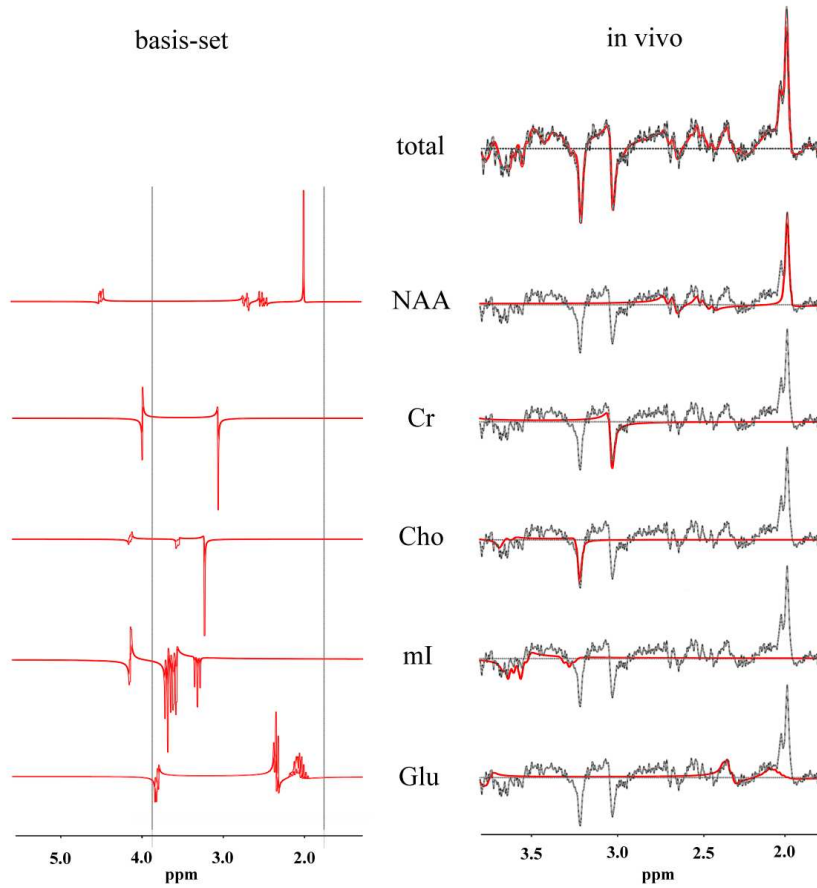


Figure 2.30: In the left column the individual basis set compounds are shown in red. In the right column the fit of each basis set compound (red) to match the measured spectrum (black) can be seen. In the top right, the sum of all the fitted compounds is shown.

While data quantification can be performed after the Fourier transformation on spectra, it can also be done before Fourier transformation in the time-domain. Two examples of such methods are AMARES [van der Veen et al., 1988] and VARPRO [Vanhamme et al., 1997].

2.8.5 Phasing the signal

Correcting the Zero Order Phases

Several methods can be used to correct for the zero order phase of spectra. The simplest one is to manually adjust the phase by multiplying $e^{-i\varphi_0}$ with different values of $\varphi_0 := \varphi_{Distance} + \varphi_{Cable} + \varphi_{Inhomo}$. This is obviously not practicable when processing a large amount of spectra, which is the case for MRSI with about $16 \times 16 = 256$ to $64 \times 64 = 4096$

2 Theoretical Background

spectra per dataset. An automatic alternative is to determine φ_0 by using the remaining water signal and to phase the whole spectrum with that phase. A disadvantage of this water referencing method is the fact, that water suppression may cause distortions of the remaining water peak. The phase of the water peak is then computed incorrectly. A good but rather time consuming solution can be to perform each measurement twice: Once with water suppression for analyzing the spectra, once without water suppression for phasing the water suppressed data set. However, this method is not applicable in clinical routine due to the long duration of MRSI sequences. Moreover there are complex algorithms that use several distinct metabolite peaks like those of creatine, NAA or choline as the fitting program LCModel does. Nevertheless, this method can be unreliable if the SNR of the metabolites is low.

The φ_0 -corrections that were used in this diploma thesis consisted of measuring a GRE image, in addition to the MRSI data, of the same voxels, compute the phase for each voxel of the imaging data and use this information for phasing.

Correcting the First Order Phases

The first order phase that result from the acquisition delay can be corrected in two different ways. The first and more obvious one is to simply multiply the signal with $e^{-i\varphi_{AD}} = e^{-i\delta \frac{\omega_0}{10^6} t_{AD}}$, with known t_{AD} from the sequence adjustments. However, additional baseline distortions of the spectra were reported [Henning et al., 2009], as depicted in fig. 2.31. The other option to correct for the acquisition delay is to truncate the first FID points of the basis set in order to get the same first order phase for the basis set and the measured spectra. This option was used in this work, leading to the basis set of fig. 2.30 (red lines) with the effects of the first order phase clearly visible.

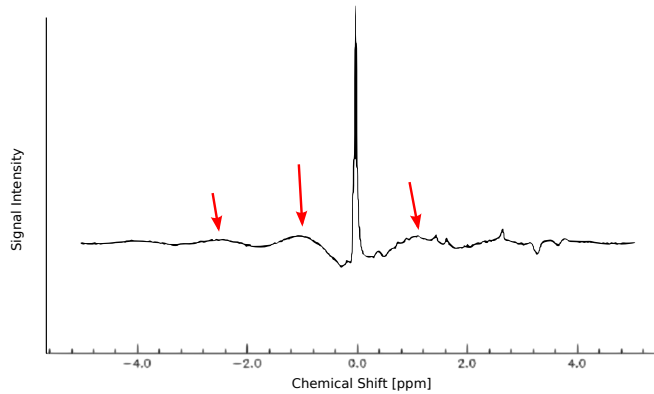


Figure 2.31: The φ_1 -correction by multiplying the data with $e^{-i\varphi_{AD}}$ leads to irregularities in the baseline.

3 Implementation

3.1 Materials & Methods: General Information

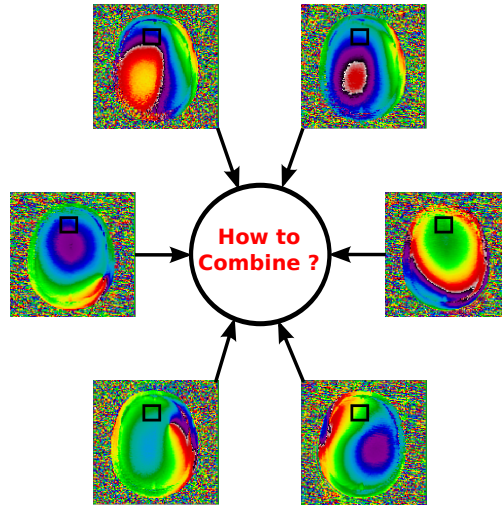
3.1.1 Principle of Coil Combination

The problematic of combining the spectroscopic data of different AC-channels is depicted in fig. 3.1. In fig. 3.1(a), the phase maps of 6 channels are shown. In black, the same voxel is drawn in the phase maps of all channels. It is obvious, that the phase of this voxel is different for all channels. Hence, the corresponding spectra of each of these channels are phased differently, as depicted in 3.1(b) (note that these spectra are simulated; however, the real spectra might have similar phases). It is evident, that summing all of these spectra leads to cancellation of the signal. In order to circumvent this, the spectra of all channels have to be phased prior to summing them up.

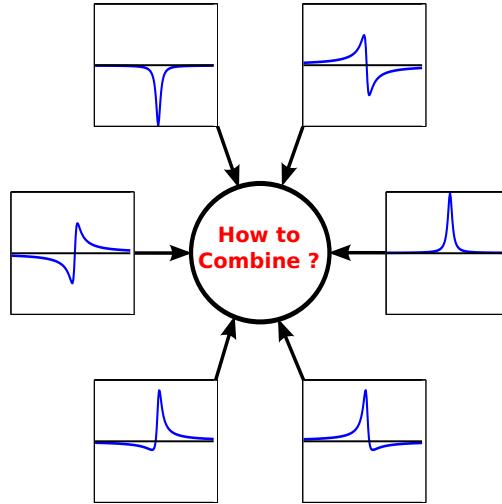
In this work, an improved approach for the combination of spectra, obtained from the individual channels of an AC, is presented, including the following steps.

- (i) First, MRSI data of the individual channels of an AC is acquired.
- (ii) two GRE images are acquired of the same slice, once with "normal" gradients, once with reversed ones. The latter is necessary to correct for phase errors resulting from gradient delays, as described further below. The parameters of the GRE sequence are similar to the one of the MRSI sequence.
- (iii) For weighting of the MRSI data, another GRE image is acquired with the VC.
- (iv) A MATLAB program processes the MRSI data by phasing (using the information of (ii)) and weighting (using the information of (ii) and (iii)) each channel with the GRE data.
- (v) The spectra of all channels are summed up.

This method will be referred to as "Gradient echo Image based coil combiNation (GIN)"



(a)



(b)

Figure 3.1: (a) The phase maps of six AC-channels illustrating the difficulty of coil combination in NMR spectroscopy. (b) Simulated spectra with different phases corresponding to the phase maps of (a).

3.1.2 Work plan

The whole work was divided in four steps:

Step 1: Validating the feasibility of the new phasing method

The feasibility of phasing the MRSI data with the GRE images was verified. This step was further divided in two parts:

- In part A, the deviation of the phase deduced from the MRSI data to that deduced from the GRE data was estimated.
- In part B, the assumption was tested, whether using the GRE phase prior knowledge, i.e. the additional phase information obtained from the GRE data, leads to better fitting results, and if this leads to a method that is more robust to changes in spectral quality.

Step 2: Implementing the Coil Combination Algorithm

In this step, the program for combining the channels was written. The resulting spectra and metabolic maps were qualitatively examined.

Step 3: SNR Comparison between the AC and VC

The SNR was compared between using the 32-channel AC, while deploying the GIN method, and the VC.

Step 4: Comparison with Existing Methods

The GIN method was compared to a present state of the art method, that is a method developed by Siemens, which is implemented on the 7 T scanner at the Center of Excellence of the Medical University of Vienna.

3.1.3 Hardware

The Scanner and the Coil

The data for this diploma thesis were acquired with a Siemens 7 T whole body NMR scanner at the MR Center of Excellence of the Medical University of Vienna, which can be seen in 3.2.

This scanner is used for development of new methods and clinical research studies only, since 7 T scanners are not yet allowed for clinical routine. Whole body 7 T scanners are still prototypes and currently only few of these exist worldwide. However, using ultra-high magnetic fields in MR offers several advantages like increased SNR, better spectral resolution (see section 2.2.4), and reduced indirect interaction between the spins of a

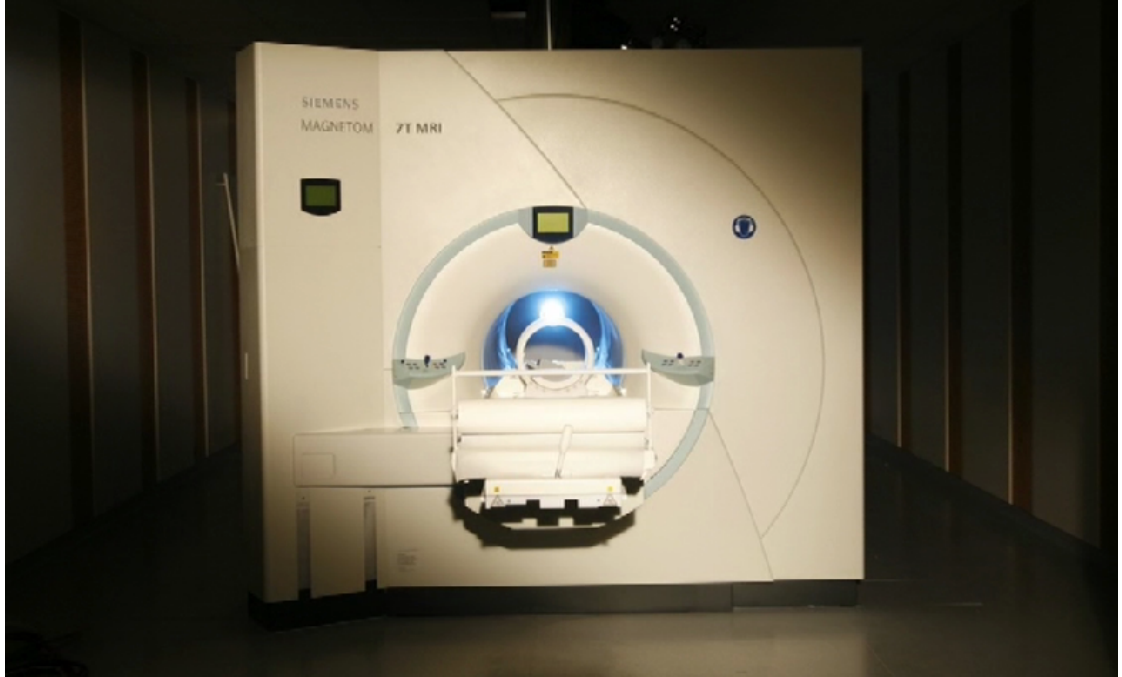


Figure 3.2: The 7T scanner at the Medical University of Vienna.

spin system referred to as j-coupling. This reduced j-coupling leads to simplified spectra and higher SNR for j-coupled metabolites. [Bogner et al., 2011] [Henning et al., 2009]

The NMR coil that was used in this work is a combined transmit and receive head coil, combining a VC and a 32-channel AC from Nova Medical Inc. Only the VC can be used for excitation, but both can be used for signal reception as it was done in this work for SNR comparison. A figure of the coil is provided in fig 3.3.

The Phantoms

An NMR measurement phantom is an object which contains NMR detectable substances, and is measured instead of volunteers. In many cases, only basic testing of work-in-progress sequences or postprocessing steps is performed. In these cases, it is better not to measure volunteers, but phantoms, since the tested methods could not work at all or lead to unusable data. After successful testing on phantoms, one can measure volunteers or patients, since it is then clear that the methods work. Properly built phantoms often provide more reproducible results, allowing better observation of artifacts related to problems in sequence design. [Hornak, 2011, Chapter 9]



Figure 3.3: The coil that was used in this work, manufactured by Nova Medical Inc.

The phantoms that were measured in this thesis are of a spherical shape with a diameter of about 15 cm. One is filled with water and the metabolites NAA, lactate, glutamate, creatine and choline. The other one is filled with dimethylpolysiloxan-oil, a silicone oil, 1g/kg tris(hydroxymethyl)-aminomethan (TRIS), and 0.2 g/kg of an orange colorant. In fig. 3.4, the water-phantom (left) and the oil-phantom (right) are shown.

The silicone oil phantom was only used for preliminary testings, since it does not contain any brain metabolites. Unfortunately, the water-phantom was originally prepared for experiments at 3 T scanners and is therefore less suitable for NMR measurements at 7 T, because of strong B_1 -inhomogeneities. This leads to high spatial inhomogeneities in the magnitude of the signal, which is shown in fig. 3.5. The reason for this behavior is mainly related to the standing wave effect (i.e. the wavelength of the RF signals at 7 T becomes similar to the diameter of the phantom) and the skin effect (i.e. the penetration of RF signals is more difficult for higher frequencies), described in [Tofts, 1994].

3 Implementation

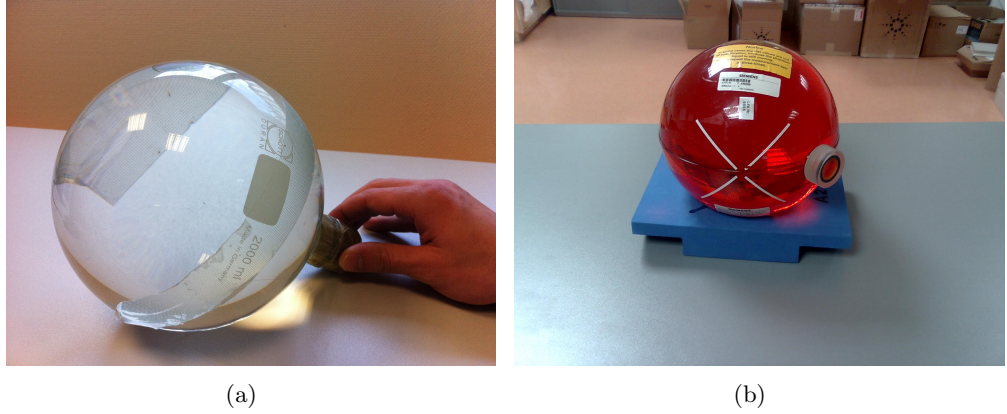


Figure 3.4: (a) The water phantom used in this work. (b) The oil phantom used for preliminary studies.

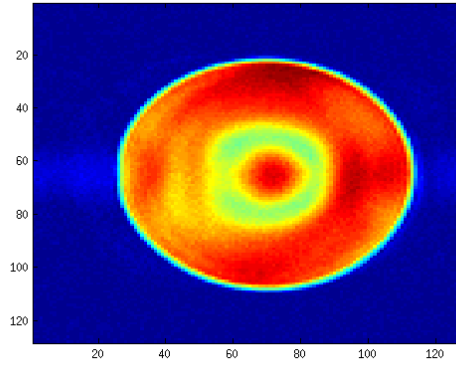


Figure 3.5: The standing wave effect causes an inhomogeneous B_1 -field. Thus, in some regions there is a high signal drop out, as in this figure clearly visible in a circle around the center of the phantom. High magnitude values are represented by red, low by blue.

3.1.4 Sequences

The MRSI Sequence

The scheme of the MRSI sequence, as it was used in this thesis, is shown in fig. 2.28. Conventional MRSI sequences use an echo, produced by a 180° -pulse, instead of the FID. This leads to several problems, including the following. At field strengths of 7 T and above, the T2-relaxation times of metabolites are decreased compared to lower magnetic fields [de Graaf et al., 2006]. Due to the faster T2-decay, the echo time TE has to be reduced in order to limit signal loss.

Moreover, slice selection at high field strengths is more prone to so called chemical shift

displacement errors, leading to different spatial displacements of the signal dependent on the chemical shift. Detailed information about this artifact can be found in [de Graaf, 2007, p. 303 ff.] and [Haacke et al., 1999, p. 421 ff.].

In order to minimize this artifact at 7 T, several methods were proposed. One way is to use special RF-pulses called “Adiabatic Pulses” for the excitation and the 180° - pulse. The problem with these pulses is their long duration, thus leading to an unfavorable increase of TE. Another way to circumvent this problem is to increase the gradient amplitudes during slice selection, accompanied with increasing the RF pulse bandwidth to maintain the slice thickness [de Graaf, 2007, p. 193 f.]. Higher RF pulse bandwidths lead to problems with the legal restrictions of energy deposition in the patients/volunteers tissue. Therefore, this option is as well not suitable for overcoming the chemical shift displacement errors at 7 T [Henning et al., 2009].

In contrast, using an FID-based sequence as proposed by Henning et al. [Henning et al., 2009] is the natural extension to further decrease the echo time and can overcome both problems at the same time: The acquisition delay of FIDs can be adjusted to even shorter times that are possible with any pulse echo sequence, and since no 180° -pulse is applied, the legal restriction of energy deposition is unproblematic.

In addition to the above mentioned advantages, acquiring the FID instead of an echo offers some more advantages, but also has some drawbacks:

– Drawbacks:

1. The FID cannot be acquired immediately after excitation, because the excitation pulse, the phase encoding and the slice selection gradients take some time, typically 0.5 ms each. This leads to a first order phase as described in section 2.5.2. The spectra containing a first order phase may look unfamiliar to spectroscopists, but do not lead to any disadvantage concerning the fitting of the spectra, since the metabolites of the basis can be simulated with the same acquisition delay. If both, the measured spectrum as well as the basis set contain the same first order phase, the spectrum can be fitted as usual.
2. Because macromolecules have a short T₂-relaxation time, the baseline of an FID-based brain spectrum contains very broad resonances of more metabolites like macromolecules than the one of an echo-based spectrum. The larger

3 Implementation

overlapping of these broad signals makes the fitting of those compounds, and thus of the whole spectra more problematic. The quantified data may be reproducible but less accurate.

– Advantages:

1. The second disadvantage can also be an advantage, since it was described that some macromolecule concentrations are different in tumor tissue compared to healthy [Seeger et al., 2003]. Hence, shorter TE offers additional information that could be valuable for diagnosis.
2. As mentioned above, one constraint in *in vivo* NMR measurements is the energy deposited in volunteers. The deposited energy increases approximately quadratically with the main magnetic field B_0 because the frequency of the RF pulse scales with B_0 , which in turn is proportional to the energy. Hence, the energy deposition is a severe restriction, especially in ultra-high field MR. Since a basic FID-sequence consists of only one pulse (e.g. 90° pulse), whereas a basic spin echo sequence consists of at least two pulses (e.g. 90° and 180°), any spin echo sequence deposits more energy in the volunteer. Therefore, in high field MR, FID-sequences are favorable.
3. Non-perfect pulses lead to additional signal loss. Because FID-sequences consist of only one excitation pulse, they are less prone to this problem than echo sequences with two or more pulses.

Other approaches to overcome this problem can be found in [Avdievich et al., 2009], [Mlynárik et al., 2006] and [Mekle et al., 2009].

Henning et al. [Henning et al., 2009] and Boer et al. [Boer et al., 2011] on the other hand used a similar approach as in the studies this diploma thesis is based on.

These considerations led to the usage of an FID-based sequence. It is a 2D-sequence, so it excites and acquires the data of a slice and it covers the k-space in a pseudo-spiral pattern shown in figure 2.23(a), in order to minimize artifacts resulting from movements of the volunteer [Bogner et al., 2011]. In all data acquisitions performed to investigate the metabolic concentrations, water suppression was applied, except if the water signal itself was of interest.

The MRSI sequence, adjusted with the parameters we used, has an overall duration of approximately 30 minutes. The measurement parameters were:

3.1 Materials & Methods: General Information

– Field of View	$220 \times 220 \times 12 \text{ mm}^3$
– Number of Voxels	$64 \times 64 \times 1$
– Voxel Size	$3.4 \times 3.4 \times 12 \text{ mm}^3$
– Acquisition Delay	1.3 ms
– Repetition Time	600 ms
– FID time points	2048
– Dwell Time	0.1667 ms

where dwell time is the sampling interval between consecutive FID time points, and field of view is that part of the excited volume that is actually measured.

The Gradient Echo Sequence

The GRE sequence of this work, for phasing and weighting the MRSI data, is a standard two-dimensional GRE sequence, i.e. the k-space is acquired line by line. The sequence is described in section 2.7.3. Since the GRE images are used for phasing the MRSI data, the used parameters have to be the same as the ones of the MRSI sequence. This is in detail the same field of view, the number of voxels must be equal or higher, and the TE of the GRE sequence must be the same as the acquisition delay of the MRSI sequence. The latter is important to get the same first order phase for the GRE and the MRSI data. Because the overall duration of one GRE measurement is only 0.6 s, more voxels were acquired with the GRE than with the MRSI sequence. The matrix size of the GRE was then reduced to that of the MRSI measurement by interpolation.

The parameters of the GRE sequence were:

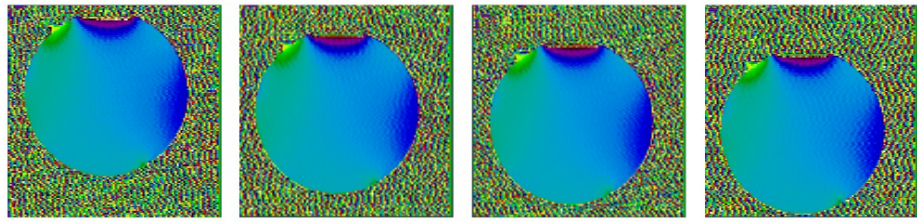
– Field of View	$220 \times 220 \times 12 \text{ mm}^3$
– Number of Voxels	$128 \times 128 \times 1$
– Voxel Size	$1.7 \times 1.7 \times 12 \text{ mm}^3$
– TE	1.3 ms
– Repetition Time	4.7 ms (minimum possible)
– Dwell Time	2 μs

3 Implementation

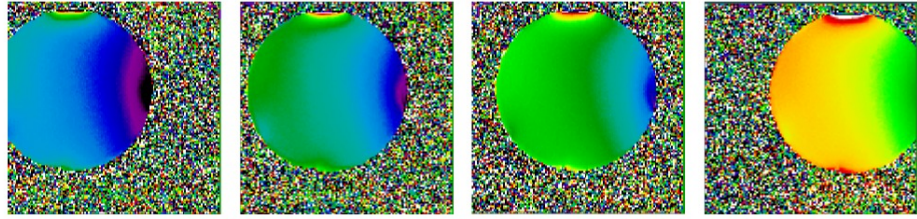
Phase Problems of the GRE Sequence

Two problems occur concerning the phase images of the used GRE sequence.

First, due to the localization in frequency encoding direction, each field of view that is placed off-center relative to the isocenter of the magnet, i.e. the point where the magnetic fields of the localization gradients are always zero, leads to an additional constant phase offset in the data. This offset is not related to any physical properties of the object, and thus has to be eliminated before further processing is performed. The effect is shown in fig. 3.6. It can be seen that the effect only occurs for shifts in frequency encoding direction.



(a) Shifts in phase encoding direction



(b) Shifts in frequency encoding direction

Figure 3.6: The field of view shift in phase encoding direction does not influence the phase (a), whereas the influence in frequency encoding direction is clearly visible (b), as the phantom measurements “Herr und Frau Phantom 6” show. Both measurements were done using the silicone oil phantom. Violet and black stand for low phase values and red and white for high values.

The problem was overcome by adding a spatially constant, but field of view-dependent phase to all voxels. The phase was calculated from the field of view shift in frequency encoding direction relative to the isocenter.

The second problem was a linearly increasing phase from one side of the GRE slice to the other. Like the first problem, this effect only occurs in frequency encoding direction.

3.1 Materials & Methods: General Information

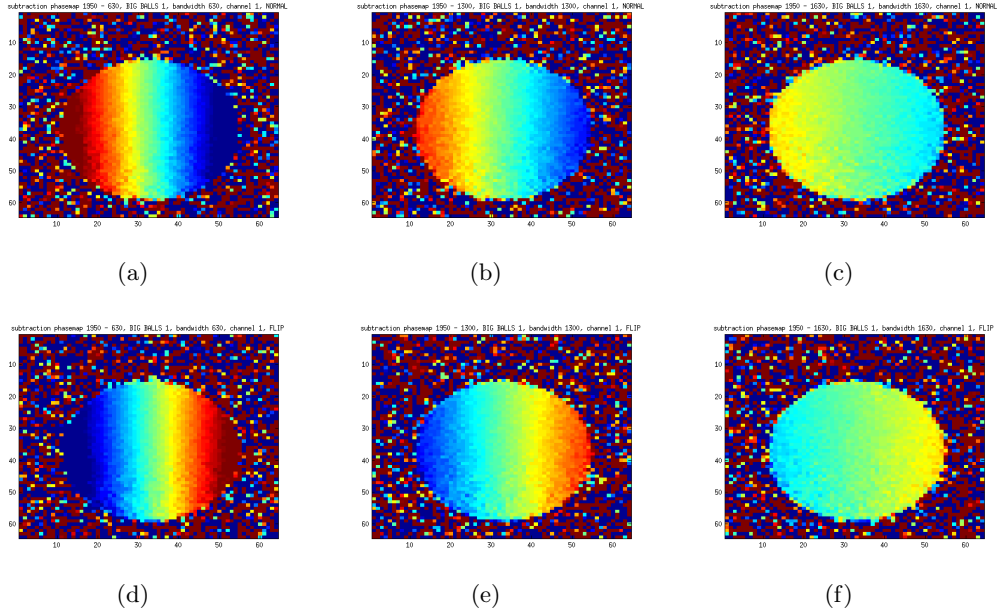


Figure 3.7: (a)-(c): The phase maps of different dwell times were subtracted from the phase map of a reference dwell time. The dwell time decreases from left to right. (d)-(f): The same is shown for reversed gradients resulting in the reversed effect. Red stands for high values, blue for low.

Further investigations showed that it is dependent on the dwell time, and is probably related to small but inevitable timing errors in the sequence. In fig. 3.7, the effect is shown by subtracting the phase maps of different dwell times from that of a reference dwell time. At the bottom, the same effect is shown for reversed gradients, leading to the reversed effect.

The exact reason for the problem is most probably a gradient delay error. Consider the GRE sequence shown in fig. 2.27. If the frequency encoding gradient starts a little too late, the expected and the actual maximum of the echo do not coincide. Since the time positions of the sampled points are computed according to the **expected** echo, the actual maximum of the echo is not sampled, as it is shown in fig. 3.8(a). The maximum of the echo is equivalent to the center of the k-space. This means, that all k-space points are shifted towards lower values, e.g. the k-space point at (0,0) is in fact at (-0.1,0) and so on. According to the Fourier shift theorem, a shift in k-space results in a linear phase in the image space.

The gradient delay was accounted for by measuring an additional image with the GRE sequence with an field of view rotated about 180° against the "normal" one (the rotated

3 Implementation

one will be referred to as the "flipped" GRE image). This rotation reverses all imaging gradients, leading to exactly the reversed effect, shown in fig. 3.8(b) and 3.7 (d) - (f). A gradient delay that leads to a linear increase of the phase from left to right, leads to a linear decrease in case of reversed gradients. Looking at both figures, 3.8(a) and 3.8(b), one can imagine that the actual echo maximum can be reconstructed. This can be achieved by simply adding both complex signals, as it was incorporated in the program.

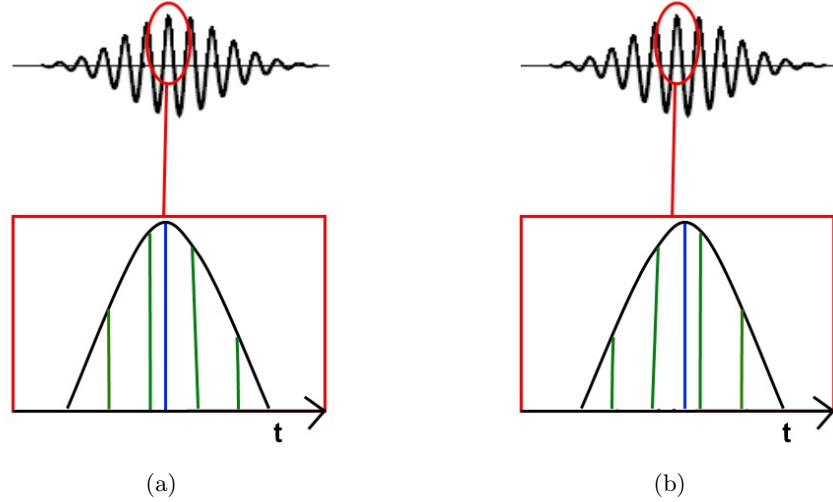


Figure 3.8: (a) The maximum of the gradient echo (blue) is not sampled (the green lines represent the sampling time points) due to gradient delays. Instead, it is sampled a little too early (as the echo should be exactly there in theory), leading to a shift in k-space. (b) For reversed gradients, the opposite is true.

3.1.5 Basis Set

The basis set for fitting the measured MRSI data with LCModel consisted of 17 compounds for the volunteers, and 18 for the phantom measurements. These were: Aspartate, creatine (Cr), gamma-aminobutyric acid, glutamine, glutamate, glycine, glycerophosphocholine, *myo*-inositol (Ins), N-acetyl aspartate (NAA), N-acetylaspartylglutamate, phosphocholine, phosphocreatine, *scyllo*-inositol, taurine, a simulated lipid with resonances at 2.7, 3.0 and 3.2 ppm and two macromolecules at 2.05 and 2.95 ppm, respectively. The phantom basis set consisted moreover of choline (Cho).

All metabolites were simulated using NMR-scope of the free program jMRUI. The first points of the simulated FIDs were truncated, in order to get the same first order phase as the measured spectra.

3.1.6 The Basic Algorithm

In this section, the basic algorithm for post processing the measurement data is described, on which the programs of this diploma thesis is founded. The main program was written in Bash and MATLAB. The flow chart of the program can be seen in fig. 3.9

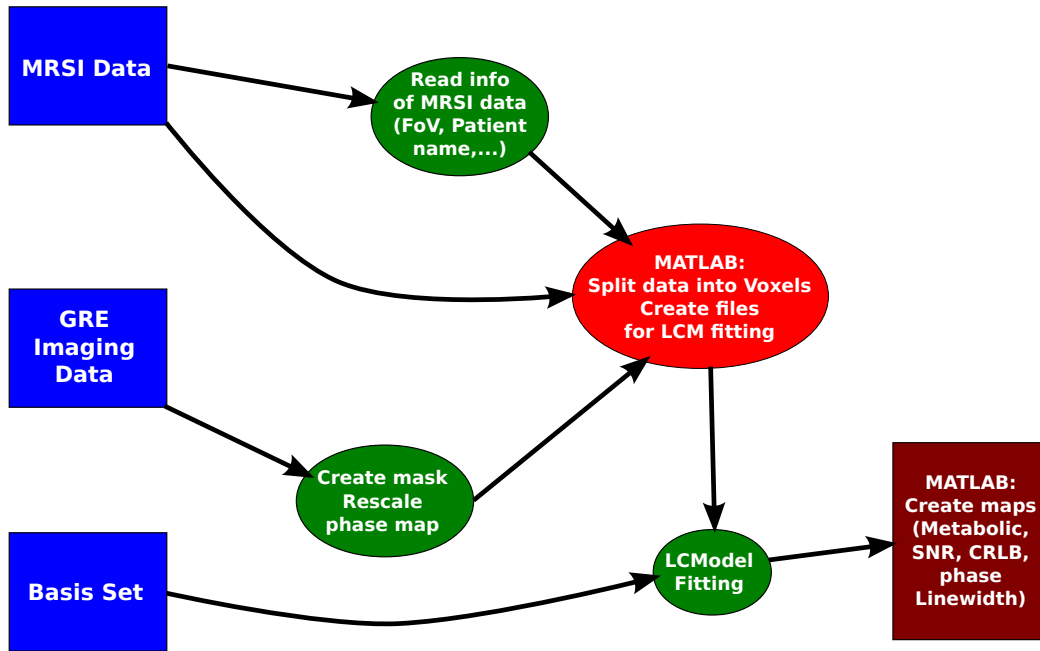


Figure 3.9: Flowchart of the basic program on which this diploma thesis is based on.

The described program requires the following input data:

- A basis set for LCModel fitting
- The MRSI-data
- Optional: Magnitude and phase-images of the GRE sequence.

This program was written to process only VC-data; it can not combine the individual channels of an AC. In the following, the program is described step by step.

3 Implementation

1. The main program has to be started via Bash, and requires the following input parameters, including the paths of the MRSI, GRE-magnitude, GRE-phase and basis set file, the path of the output folder and some further options.
2. Important information is obtained from the MRSI text header, e.g. parameters concerning the spatial position and orientation of the measured slice. This is necessary to overlay the data with other imaging data.
3. In case of using a GRE image, the GRE phase image is prepared for MATLAB usage and a mask is created out of the magnitude map. This mask ensures that only voxels within the brain are processed, and thus improves the processing speed.
4. A MATLAB program reads in the MRSI and GRE data and splits all the measured data in single voxels. This is necessary to improve the processing speed (i.e. on a multi-core computer several voxels can be quantified in parallel). For each voxel within the mask, a control and a raw file is created for LCModel fitting. The control file contains parameters that are used to control the fitting process, e.g. a mean and standard deviation of the phase within which LCModel is allowed to vary it during the fitting process. The raw files contain the FID of the respective voxel.
5. The LCModel fitting process is started with a Bash command. LCModel creates a table of the results obtained from each voxel, where information like the concentrations of the fitted metabolites, the phase, the SNR and so forth is written.
6. A MATLAB program reads and summarizes the results of all single-voxel tables, and creates maps, like metabolic maps, a phase map, and an SNR map. The metabolic maps display the concentrations of the fitted metabolite in dependence of the position, e.g. the concentration of NAA of all processed voxels.

3.1.7 The Data

Using the Raw Data

The Siemens scanner provides the measured data in different formats. Since we did not want the data to be processed by the automatic scanner post processing chain, we extracted our measured data in the following way. During the measurement, the data, i.e. the complex numbers that are proportional to the voltage measured with the coil(s), are written directly to a file. The data are not modified by any post processing step, but there is a header put in front of the data. This header contains additional information

like the name of the patient/volunteer, etc. Moreover, each data block is preceded by the so called measurement data header, which contains information about the following data block, like the k-space point of the data block, the number of FID data points, the used channels of the coil, and so on. The data can be extracted in this raw format using a special program at the scanner control computer. The files of this format are referred to as “raw data”.

On the other hand, the most common way of getting the measurement data out of the scanner is using the DICOM file format. Some post-processing steps like weighting the individual channels, applying a spatial Fourier transform, and in case of AC MRSI data, phasing the individual channels with the phase of the first MRSI-point, are performed, when saving the data in the DICOM file format. This phasing is the state of the art method to combine the AC-channels and is implemented on Siemens scanners. Because of this phasing, the DICOM files of the MRSI data could not be used in this work, since we needed unphased data. Instead, the raw data had to be used.

The Measured Datasets

The following data sets were measured for testing the phasing and the combination of the AC channels:

- One volunteer (Volunteer 1) was measured with the VC only.
- One volunteer (Volunteer 2) was measured with the AC using the MRSI as well as the GRE sequence.
- Five volunteers (Volunteer 3 – Volunteer 7) were measured using the MRSI and the GRE sequence, in modes VC and AC. One volunteer (Volunteer 4) seems to have moved his/her head during the MRSI VC measurement, leading to unacceptable artifacts. The VC measurement was therefore excluded from the evaluation, the AC measurement was used for step 2 and step 4.
- Three measurements (Phantom 1 – Phantom 3) were measured using the water phantom described in section 3.1.3. It was measured using the MRSI as well as the GRE sequence, in modes VC and AC. The AC measurement of Phantom 3 failed due to unknown reasons, thus the AC measurement had to be excluded from evaluation. The VC measurement was however used for step 1. The VC MRSI measurements were performed once with water suppression, and once without. This was done for step 1, part A in order to have a good phase reference.

3 Implementation

Further measurements using volunteers, the water and oil-phantom were done for preliminary evaluations.

The data of Volunteer 1 were used for part B of step 1. The VC measurements of Volunteer 3 – Volunteer 6 and Phantom 1 – Phantom 3 were used for part A of step 1. All phantom and volunteer measurements that included reliable VC and AC data were used for step 3.

3.2 Step 1: Validation of Proper Phasing & Additional Benefits

3.2.1 Materials & Methods

Before writing the coil combination algorithm, it was necessary to check whether phasing the MRSI data with the GRE image data is feasible. This step is further subdivided in two parts. In part A the phases of the first MRSI FID point, the phase that was computed by LCModel, and the phase of the GRE image were compared. In part B the influence of phasing the MRSI data using the GRE data on LCModel fitting was investigated. In both parts, only the data of the VC were used.

Part A: Comparison of Phase Maps

In part A of step 1, the phase of the MRSI and GRE data was directly compared. Therefore, the MRSI data was fitted by LCModel without any preceding phasing and without restricting LCModel in the phase computation. LCModel varies the phase to get the best match between the measured spectrum and the basis set. These "LCModel phase maps" were used for the comparison.

Next, out of the first FID point, the phase was computed for each MRSI voxel. The reason for using the first point is that its magnitude is the highest, and that using another point would introduce an additional first order phase. In case of phantom measurements, non-water-suppressed MRSI data was acquired and used for this comparison, since the phase is then not distorted due to a deformed, partially suppressed water peak.

Afterwards, the GRE data were corrected for phase errors caused by gradient delays, as described in 3.1.4. Using the corrected data, the phase was computed for each voxel.

These three phase maps (the phase map arising from the fitting process of LCModel ("LCM phase map", Φ_{LCM}), the one resulting from the first MRSI FID point ("FID phase map", Φ_{FID}), and the one from the GRE-image ("GRE phase map", Φ_{GRE}))

3.2 Step 1: Validation of Proper Phasing & Additional Benefits

were then compared.

Therefore, a mask within the brain/phantom was created for all data sets. Only the voxels within these masks were used for evaluation. Subsequently, the GRE phase maps were subtracted from the FID phase maps, as well as from the LCM phase maps. Moreover, the LCM phase maps were subtracted from the FID phase maps. The resulting difference maps are referred to as “FID - GRE” ($\Phi_{FID-GRE}$), “LCM - GRE” ($\Phi_{LCM-GRE}$) and “FID - LCM” ($\Phi_{FID-LCM}$). The phase differences arising from all volunteers were put together, and the mean and standard deviations were computed for these three sets, in order to check for consistency between the GRE and the FID phase, and to check whether phasing with the GRE data or the first FID point is favorable.

The same was done separately for the phantom measurements because their phase maps differed substantially from the ones of the volunteer measurements.

To check for reproducibility between different measurements, the phase differences were also compared for each volunteer/phantom individually. The whole process of step 1 part A is summarized in fig. 3.10.

Part B: Side Benefits

In addition to checking the consistency between the phase maps directly, the effects of using the GRE phase information on the fitting process were investigated for different simulated SNR-levels, line widths and acquisition delays. In all three cases, the basic program described in section 3.1.6 was used, but the fifth step of the program was changed as follows:

- SNR simulation: Gaussian noise was added to all voxels of the MRSI data in varying extents to simulate different SNR levels.
- Line width simulation: This should mimic the acquisition of data with lower B_0 homogeneity. The line width was increased by applying an exponential filter to each FID according to

$$S_{filtered}(\vec{r}, t) = S(\vec{r}, t) \cdot e^{-\pi \cdot LWI \cdot t} \quad (3.1)$$

where LWI is the Line width increase in Hz.

- Acquisition delay simulation: The first points of the FID were truncated which is equivalent to a longer acquisition delay. The number of truncated points was

3 Implementation

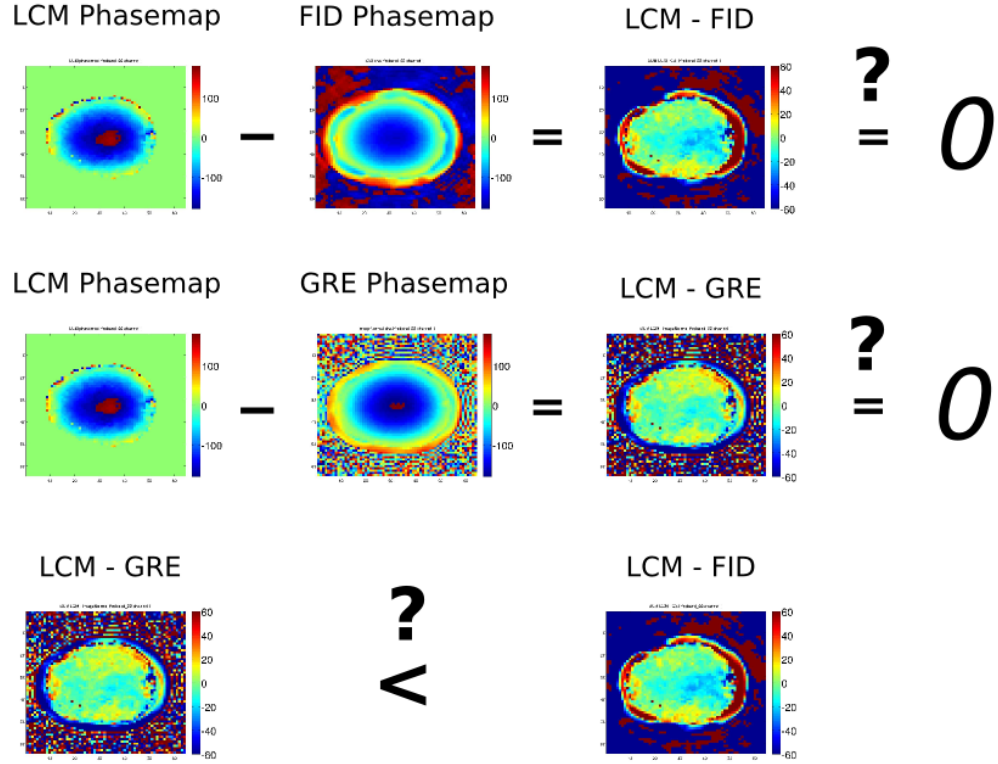


Figure 3.10: Summary of the whole process of step 1 part A.

incrementally increased. Since this leads to a higher first order phase, a different basis set and GRE images with adapted echo times had to be created/acquired for each simulated acquisition delay.

The different modified data sets were then processed like in the basic program. Once, they were processed using the phase information of the GRE image and once without. In case of using the phase information, LCModel was instructed not to vary the phase. The differences of important fitting results (metabolic concentrations, the CRLBs of these, and the phase) between the modified MRSI data and a "gold standard" were calculated. The "gold standard" was defined as the fitting results obtained from the non-modified MRSI data without using any phase prior knowledge. These differences were compared between using the phase prior knowledge and not using it, for varying SNRs, line widths and acquisition delays and within two regions of the brain with about 25 voxels each.

3.2 Step 1: Validation of Proper Phasing & Additional Benefits

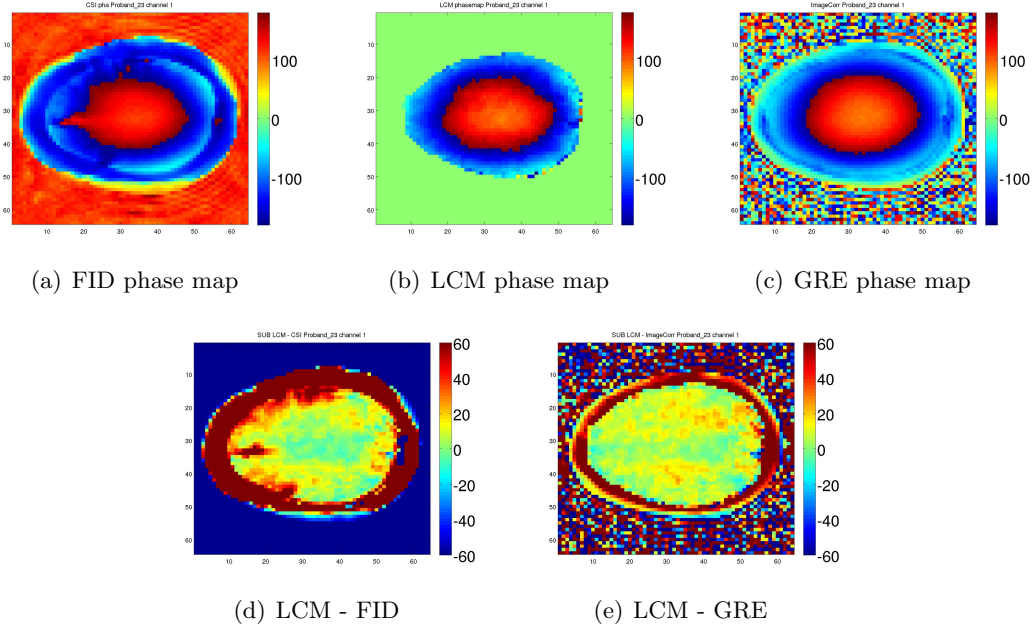


Figure 3.11: The phase and phase subtraction maps of Volunteer 7. Top row: Phase maps Φ_{FID} , Φ_{LCM} and Φ_{GRE} . Lower row: Subtraction phase maps $\Phi_{LCM-FID}$ and $\Phi_{LCM-GRE}$.

3.2.2 Results

Part A: Phase Map Comparison

In figures 3.11 and 3.12, phase maps Φ_{GRE} , Φ_{LCM} , Φ_{FID} , and the difference maps $\Phi_{LCM-FID}$, $\Phi_{LCM-GRE}$ are shown for a volunteer and a phantom measurement. A constant phase was added to the GRE and FID phase maps in order to minimize the deviation to the LCM phase map.

Looking at fig. 3.11, one can see that the volunteer phase maps match each other quite well. It is clearly visible that the GRE and LCM phase maps match better than the LCM and the FID phase maps. This is the case for all volunteer measurements, except for one, where no difference is visible.

The phase maps of the phantom measurements differ substantially firstly from each other, as depicted in fig. 3.12, and secondly from that of the volunteer phase maps. A different phase had to be added to the phantom phase maps Φ_{GRE} and Φ_{FID} to match Φ_{LCM} . Especially at the center of the phantom, severe problems are encountered, as the LCM phases do not match there at all with the other phase maps. LCModel seems not capable of fitting the phase at the center, as suggested by fig. 3.12(b). The spectra in

3 Implementation

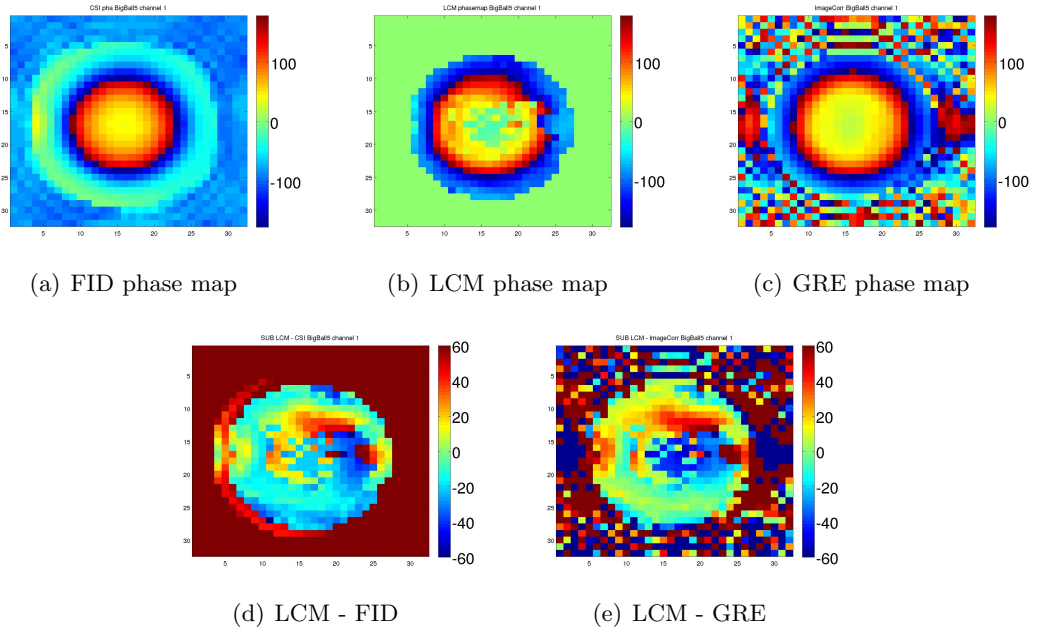


Figure 3.12: The phase and phase subtraction maps of the phantom measurement Phantom 2. (a)-(c): Phase maps Φ_{FID} , Φ_{GRE} and Φ_{LCM} . In (b) the fitting problems at the center of the phantom are clearly visible. (d),(e): Subtraction phase maps $\Phi_{LCM-FID}$ and $\Phi_{LCM-GRE}$.

3.2 Step 1: Validation of Proper Phasing & Additional Benefits

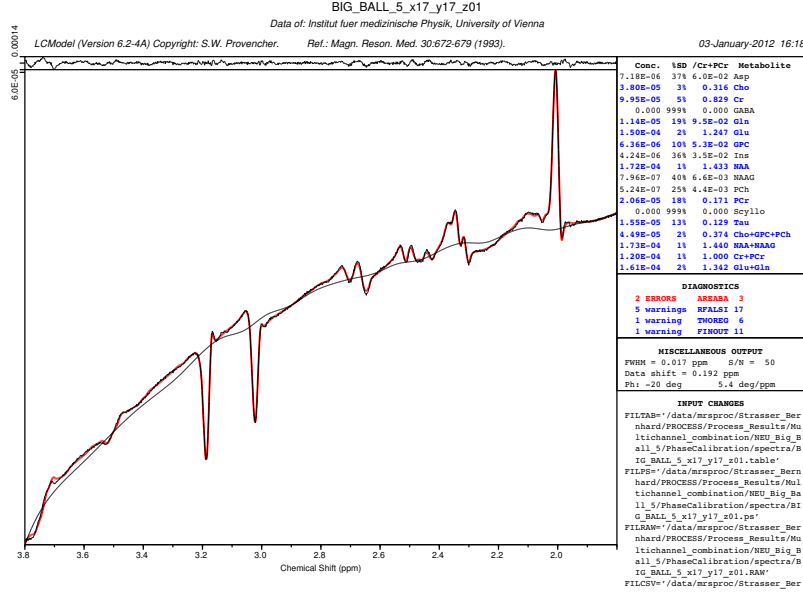


Figure 3.13: A spectrum of the center region of fig. 3.12(b). All voxels at the center suffer from poor water suppression, leading to a strongly curved baseline.

this region show a highly bent baseline originating from poor water suppression. An example spectrum of this region is given by fig. 3.13. However, it is unclear why LCModel cannot determine the phase, even if the fit seems to be fine. These problems occurred in all phantom measurements, except in one. Standing wave effects are supposed to be responsible for the poor water suppression. Further investigations have to be done. Designing a different phantom that is less prone to standing wave artifacts is planned.

Nevertheless, the GRE image based phasing of MRSI data (and therefore the GRE image based coil combination) seems to be possible for volunteer measurements. The mean and standard deviation of the phase differences of all volunteers confirm this assumption, and since the standard deviation of $\overline{\Phi}_{LCM-GRE}^{vol}$ is lower than that of $\overline{\Phi}_{LCM-FID}^{vol}$, this method seems to be superior to the state of the art method.

$$\overline{\Phi}_{LCM-GRE}^{vol} = (-30 \pm 11)^\circ$$

$$\overline{\Phi}_{LCM-FID}^{vol} = (-15 \pm 14)^\circ$$

$$\overline{\Phi}_{FID-GRE}^{vol} = (-14.4 \pm 8.7)^\circ$$

3 Implementation

Those for the phantoms are:

$$\overline{\Phi}_{LCM-GRE}^{pha} = (-63 \pm 32)^\circ$$

$$\overline{\Phi}_{LCM-FID}^{pha} = (-40 \pm 29)^\circ$$

$$\overline{\Phi}_{FID-GRE}^{pha} = (-23 \pm 13)^\circ$$

To correct for a constant phase offset, the mean phase $\overline{\Phi}_{LCM-GRE}$ was added to Φ_{GRE} so that the deviation to Φ_{LCM} is minimized. This mean phase difference $\overline{\Phi}_{LCM-GRE} = -30^\circ$ was used for the coil combination in the final program, in order to get the most accurate phasing of the spectra with the GRE data.

From the results of $\overline{\Phi}_{LCM-GRE}^{vol}$ and $\overline{\Phi}_{FID-GRE}^{vol}$ one can deduce that phasing the MRSI data with the GRE phase information is possible for volunteers. Since $\approx 95\%$ of all GRE phases concur with the LCM phases within 22° , which can be partially explained by the uncertainty of the LCModel phase computation, the phasing prior to coil combination of AC MRSI data seems as well feasible.

Next, the constancy of the phase differences were investigated. In table 3.1, the means and standard deviations of $\Phi_{LCM-GRE}$, $\Phi_{LCM-FID}$ and $\Phi_{FID-GRE}$ are shown for each measurement separately. $\overline{\Phi}_{LCM-GRE}$ was added to Φ_{GRE} , and $\overline{\Phi}_{LCM-FID}$ to Φ_{FID} prior to subtraction. The means and standard deviations of the volunteer measurements are very similar, thus proving the reliability of our method for volunteer measurements.

Measurement	$\Phi_{LCM-GRE}$	$\Phi_{LCM-FID}$	$\Phi_{FID-GRE}$
Phantom 1	-8 \pm 44	-45 \pm 38	38 \pm 13
Phantom 2	-3 \pm 31	-43 \pm 28	41 \pm 14
Phantom 3	7 \pm 14	-43 \pm 19	41 \pm 13
Volunteer 3	-2 \pm 11	-7 \pm 14	4.9 \pm 8.4
Volunteer 5	-4 \pm 11	-20 \pm 12	16.1 \pm 3.3
Volunteer 6	-3.2 \pm 8.3	-24.1 \pm 9.5	20.9 \pm 5.5
Volunteer 7	8.3 \pm 6.6	-7.8 \pm 9.1	16.2 \pm 8.4

Table 3.1: The mean values and standard deviations of the phase subtraction maps for each volunteer/phantom individually.

As shown in table 3.1, the volunteer phase differences are reproducible. The phantom measurements are as well reproducible, but show high standard deviations, except for

3.2 Step 1: Validation of Proper Phasing & Additional Benefits

Phantom 3. In all volunteer measurements and in the Phantom 3 measurement, the standard deviations of $\Phi_{LCM-GRE}$ are lower than that of $\Phi_{LCM-FID}$, thus showing again the superiority of phasing the MRSI data with the GRE data.

Part B: Side Benefits

Although many metabolites are in principle detectable in the human brain at 7 T, only the phase differences to the gold standard and few metabolites and their CRLBs are shown in dependence of SNR, line width and acquisition delay.

In the figures 3.14 - 3.16, the phase difference to the gold standard is shown for using the GRE phase prior knowledge in blue, and for not using it in orange.

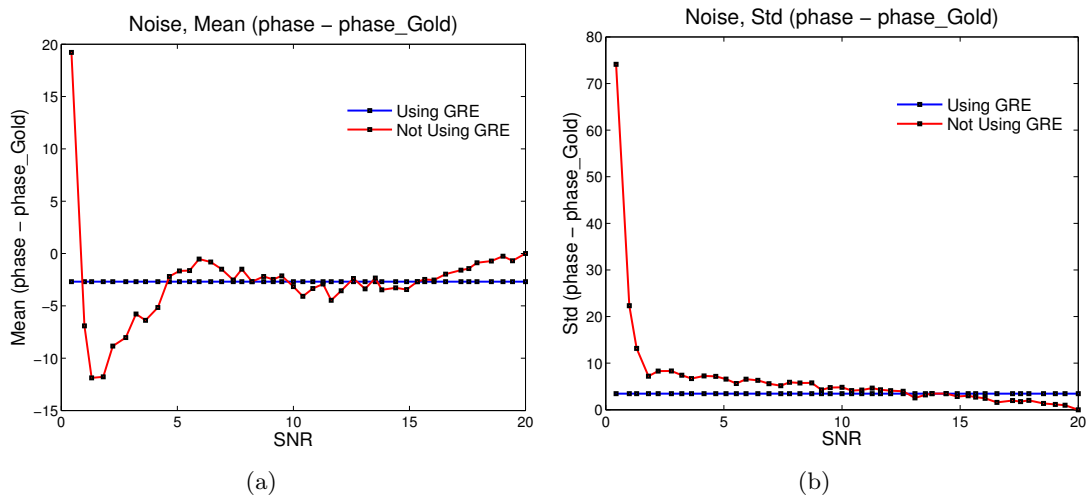


Figure 3.14: After simulating different SNR values, the phase maps resulting from LCMModel fitting were subtracted from the non-modified phase maps. The mean and standard deviation of these phase differences are plotted in dependence of the SNR. The blue curves show the results from using the GRE phase prior knowledge, while the orange ones show the results of letting LCMModel compute the phase.

These results show clearly that the phase determined by LCM varies with different spectral quality (i.e. SNR and line width), although it should in principle be independent of these properties. This provides evidence that LCM based phase estimation is prone to both systematic and statistical errors. From figures 3.14 - 3.16 it is obvious that using the phase information of the GRE images has some benefit over not using this additional knowledge, at least for data of lower spectral quality, that are difficult to quantify.

The phase of the MRSI data is of course identical to the gold standard since they were defined to be identical. However, the variability of the phase as determined by LCMModel

3 Implementation

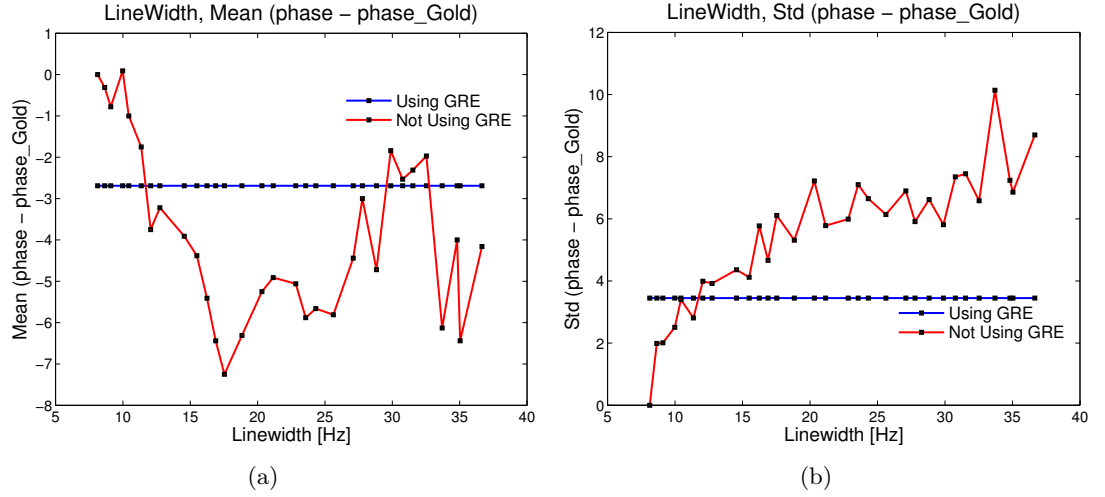


Figure 3.15: The mean and standard deviation of the phase difference in dependence of the simulated line width. The blue curve results from using the GRE phase prior knowledge, the orange one from not using it.

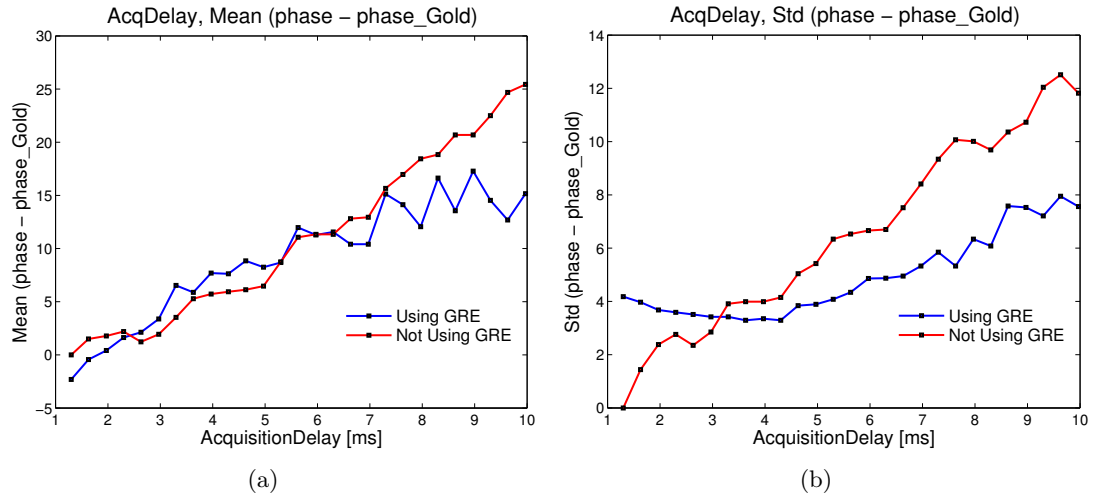


Figure 3.16: The mean and standard deviation of the phase difference in dependence of the simulated acquisition delay

indicates that these values are certainly not the "correct" values. They are just assumed to be close to the correct values as they were determined based on spectra of very high spectral quality. In any way, some sort of reference is necessary.

3.2 Step 1: Validation of Proper Phasing & Additional Benefits

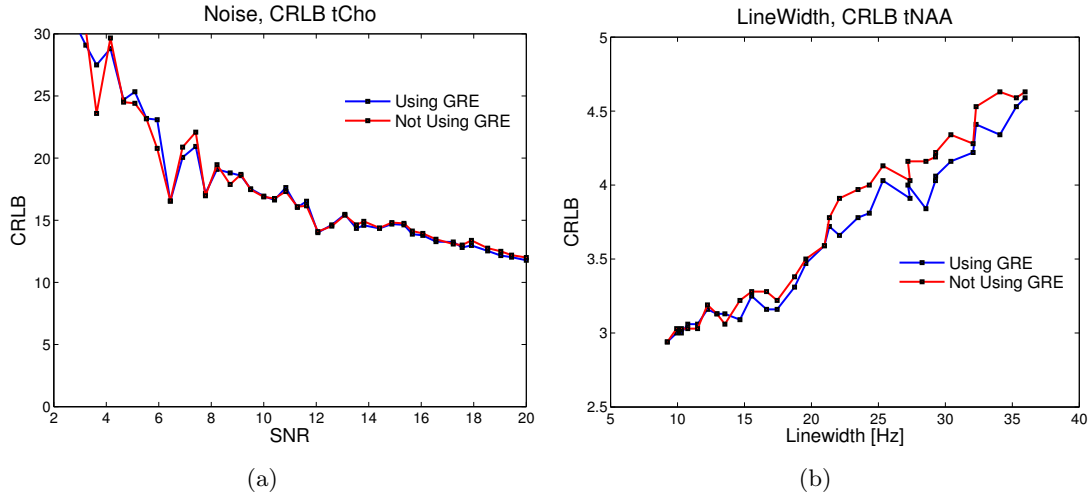


Figure 3.17: The CRLBs of tCho and tNAA in dependence of the simulated SNR and line width, respectively. There are only marginal differences between the phase prior knowledge (blue) and the LCModel phase computation (orange)

In fig. 3.17 the CRLBs of tCho and tNAA are shown in dependence of the SNR and the line width, respectively. There is hardly any difference in the CRLB of tCho for using the GRE phase information and not using it. In case of the CRLB of tNAA, one can see that the phase prior knowledge leads to a slightly lower deviation. However, there is no clear superiority when comparing the CRLBs of more metabolites and in dependence of all three modifications.

The same is true for the ratio concentrations of different metabolites. An example is given in fig. 3.18 for tNAA in dependence of the acquisition delay.

Summing up step 1, one can conclude that phasing the MRSI data with the GRE data is possible. The phase of the GRE images is comparable with the phase computed by LCModel and that of the first FID point of high quality MRSI data.

In terms of low quality MRSI data, the fitting of the phase by LCModel is more prone to errors. Thus, phase prior knowledge of GRE images improves the phase estimation. However, we could not find any significant effect on the metabolic concentrations and the CRLBs of these. Nevertheless, the quantification of the metabolites is not impaired by using the additional phase information and the processing speed is enhanced by a factor of approximately 4, according to the LCModel manual [Provencher, 2011, p. 113]. After investigating the effects of phasing with the GRE phase prior knowledge on single channel

3 Implementation

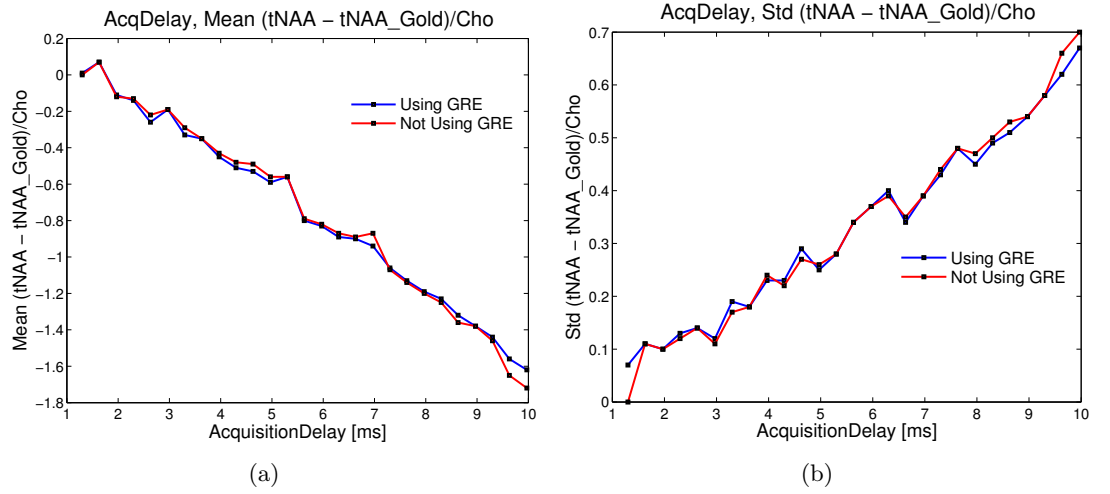


Figure 3.18: The ratio maps of the deviation of $tNAA/Cho$ to the gold standard. There is more or less no difference between the GRE based phasing and the standard approach of letting LCModel compute the phase.

(i.e. VC) MRSI data, the work could be continued with step 2, the implementation of the coil combination algorithm.

3.3 Step 2: Implementing the Coil Combination Algorithm

3.3.1 Materials & Methods

An algorithm for combining the MRSI data of different channels was implemented in the basic program. Since the MRSI data could not be used in the DICOM format, some further modifications had to be made to the basic program.

A flow chart of the extended program can be seen in fig 3.19.

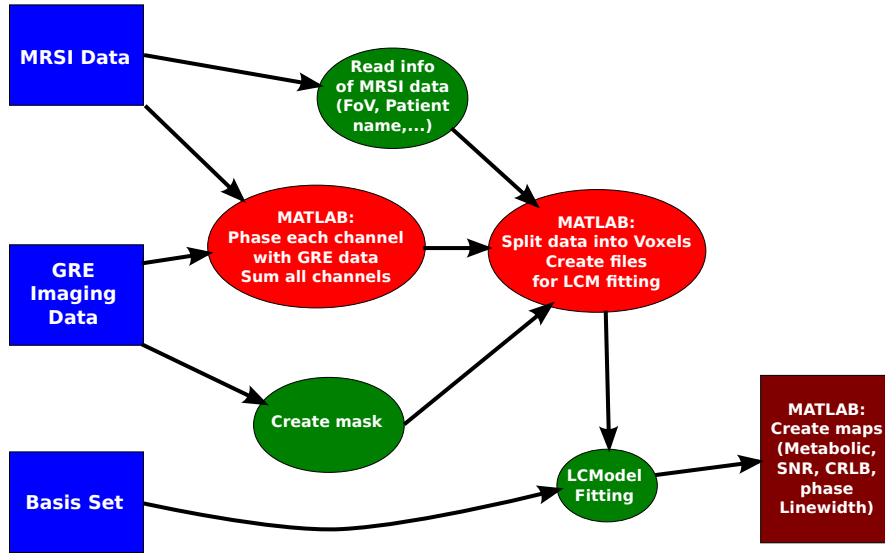


Figure 3.19: Flowchart of the extended program to combine the channels of an AC using the GIN combination method. The MRSI data is phased before splitting it into the voxels, as it is illustrated by the additional red ellipse at center-right.

The first step of the coil combination algorithm is to phase the MRSI data S_{MRSI} with the GRE data:

$$S_{phased}(channel, \vec{r}, t) = e^{-i\varphi_{AC,GRE}(channel, \vec{r})} \cdot S_{MRSI}(channel, \vec{r}, t) \quad (3.2)$$

with

3 Implementation

S_{phased}	...	Phased time domain MRSI signal
S	...	Original time domain MRSI signal
$\varphi_{AC,GRE}$...	Phase of the GRE data acquired with the AC

The phased MRSI data has then a phase φ_{phased} of

$$\varphi_{phased}(channel, \vec{r}) = \varphi_{MRSI}(channel, \vec{r}) - \varphi_{AC,GRE}(channel, \vec{r}) \quad (3.3)$$

Assuming that the phases of the MRSI data and of the GRE image are the same, φ_{phased} is zero.

The data are then weighted by the magnitude of the GRE image, channel by channel and voxel by voxel. As a result, voxels with low signal are weighted less.

$$S_{weight}(channel, \vec{r}, t) = |I_{AC}(channel, \vec{r})| \cdot S_{phased}(channel, \vec{r}, t) \quad (3.4)$$

where I_{AC} is the GRE imaging data acquired with the AC.

The signal is summed over all channels and weighted with another weighting factor, the magnitude of the VC GRE data I_{VC} , in order to get a homogeneous signal:

$$S_{Comb}(\vec{r}, t) = \frac{I_{VC}(\vec{r})}{\sum_{channels} |I_{AC}(channel, \vec{r})|^2} \cdot \sum_{channels} S_{weight}(channel, \vec{r}, t) \quad (3.5)$$

All in all, the channel combined MRSI signal S_{Comb} is obtained by

$$S_{Comb}(\vec{r}, t) = \frac{I_{VC}(\vec{r})}{\sum_{channels} |I_{AC}(channel, \vec{r})|^2} \cdot \sum_{channels} I_{AC}^*(channel, \vec{r}) S(channel, \vec{r}, t) \quad (3.6)$$

where the $*$ denotes the complex conjugation operator. The conjugation inverts the phase of the GRE data, which together with the multiplication with the MRSI data leads to the phase difference of eq. (3.3). The algorithm for the channel combination was implemented in part 5 of the basic program according to eq. (3.6).

In addition to this change, the part of the basic program for reading information of the MRSI text header (part 2 of the basic program) and the read in of the MRSI data itself (included in part 5 of the basic program) had to be changed, due to the usage of raw

3.3 Step 2: Implementing the Coil Combination Algorithm

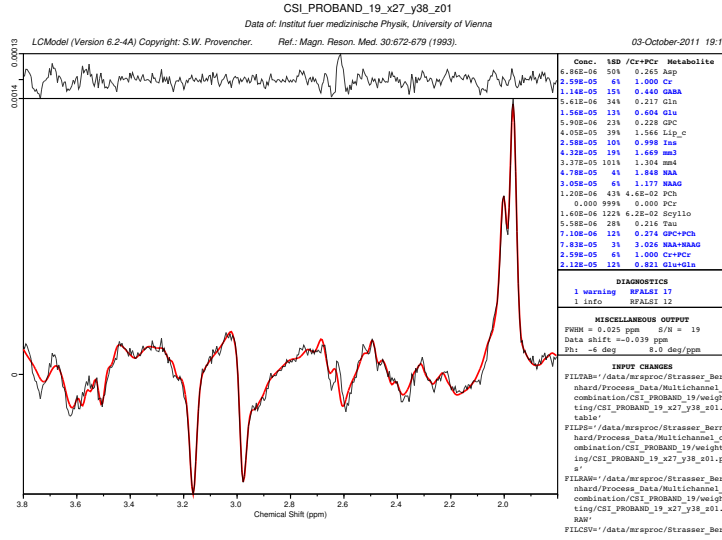


Figure 3.20: An example spectrum of a volunteer that shows the feasibility of the GIN method.

instead of DICOM files. The latter was achieved by writing a MATLAB function for reading MRSI raw data. With little modifications, another function for reading GRE image raw data was as well written for the sake of convenience.

Moreover, the corrections for the phase problems of the GRE data were implemented in part 2 (reading out the field of view shift in frequency encoding direction) and 5 (correcting for the shift and summing the "normal" and the "flipped" GRE image data).

3.3.2 Results

To prove that the GRE based coil combination algorithm was programmed correctly and leads to the desired results, a spectrum resulting from the GIN method is shown in figures 3.20.

This spectrum shows that no severe phasing problems prior to coil combination occur, since the SNR is high and the spectrum seems not to be distorted. If the GRE based coil combination did not work properly, signal cancellation would happen and the resulting SNR would be low. Considering the spectra of more voxels and different volunteers leads to the same conclusion. Most spectra allowed a quantification of 7 metabolites with a CRLB of below 20%, which is a widely used threshold for the defining reliable quantification.

3 Implementation

In fig. 3.21, the metabolic maps of AC MRSI data, processed with the GIN method, are compared with those maps obtained from VC MRSI data. The maps agree well, showing again the correctness of our method. More metabolic maps and in particular ratio maps are shown in step 4 in the course of comparing the GIN method with the available technique.

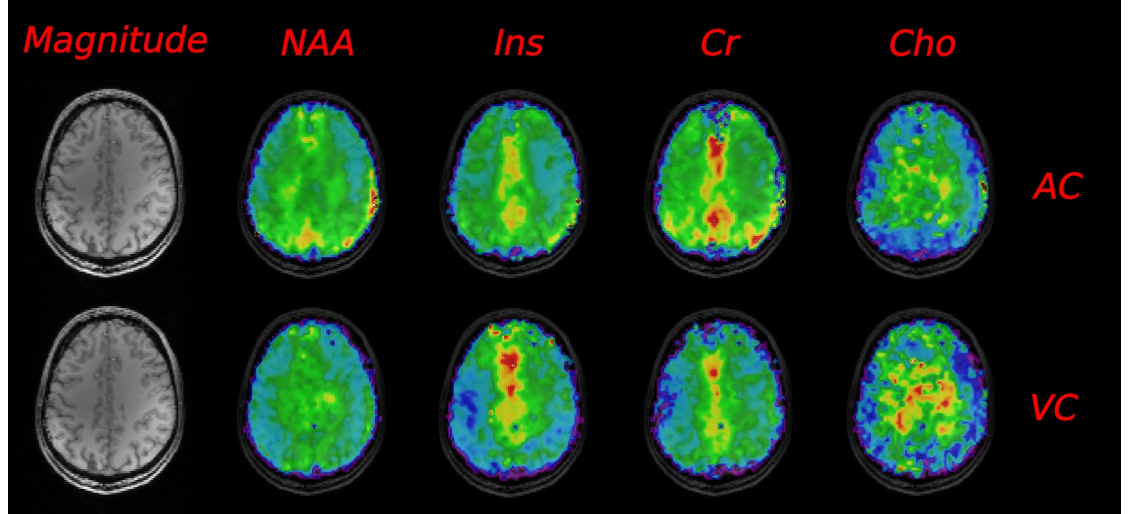


Figure 3.21: Top row, from left to right: The magnitude map and the metabolic maps of NAA, *myo*-Inositol, total creatine, and total choline, derived from AC data and processed with our method. Lower row: The same maps resulting from the VC data. The AC and VC maps are scaled the same for each metabolite. All metabolic maps are zero filled with a factor of two. Low values are represented by black and violet, high by white and red. The magnitude maps are in both cases the same and acquired with a different sequence.

Finally, fig. 3.22 proves that processing AC MRSI data with this method improves the reliability of the fit compared to VC MRSI data, by showing that the CRLB values of the AC are in all cases lower than those of the VC.

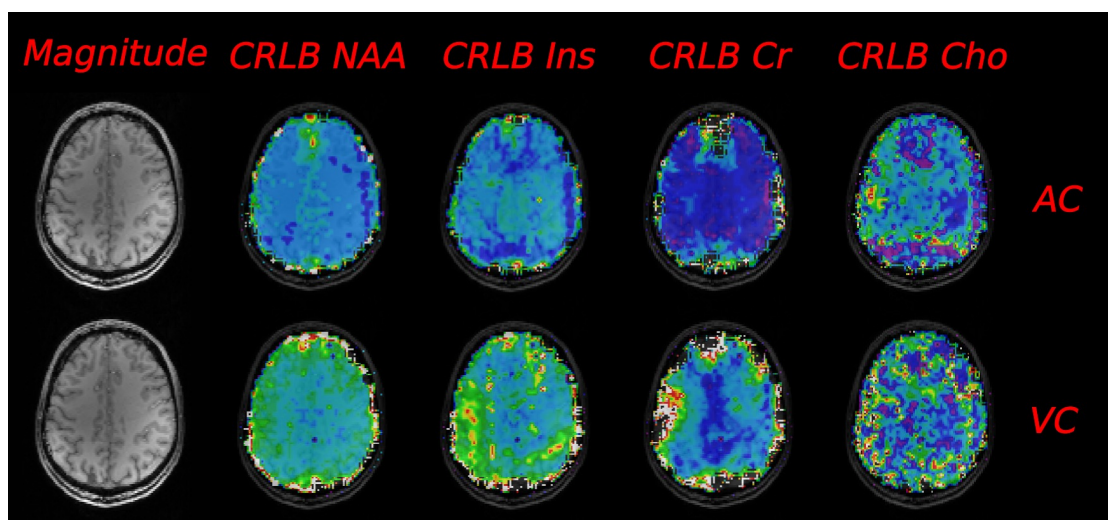


Figure 3.22: Top row, from left to right: The magnitude map and the CRLB maps of NAA, *myo*-Inositol, total creatine, and total choline derived from AC data and processed with our method. Lower row: The same maps resulting from the VC data. The CRLB maps are all scaled the same for AC and VC, and are zero filled with a factor of two. One can see that the CRLBs of the AC maps are lower, since they have more colors close to violet, which represents the minimum of the scale, whereas red represents the maximum. The magnitude maps are again in both cases the same.

3.4 Step 3: Validation of SNR Increase

3.4.1 Materials & Methods

In this step, the SNR between the AC and the VC was compared for using the GIN method. Since LCModel underestimates high SNR values, a MATLAB function for computing the SNR of spectra was written.

The SNR Computation Function

The program was further extended with the function for computing the SNR of spectra. The flow chart of the extended program is shown in fig. 3.23.

The reason for writing an own function to compute the SNR is founded in the way how LCModel defines the noise of a spectrum. LCModel fits the measured spectrum with all components of the basis set and computes a baseline - a spline function - to characterize the slowly varying components of the spectrum. The “Signal” for computing the SNR is then defined as the maximum of the baseline-subtracted spectrum in a given chemical shift range. The noise is defined in LCModel as the root-mean-square of the residuum,

3 Implementation

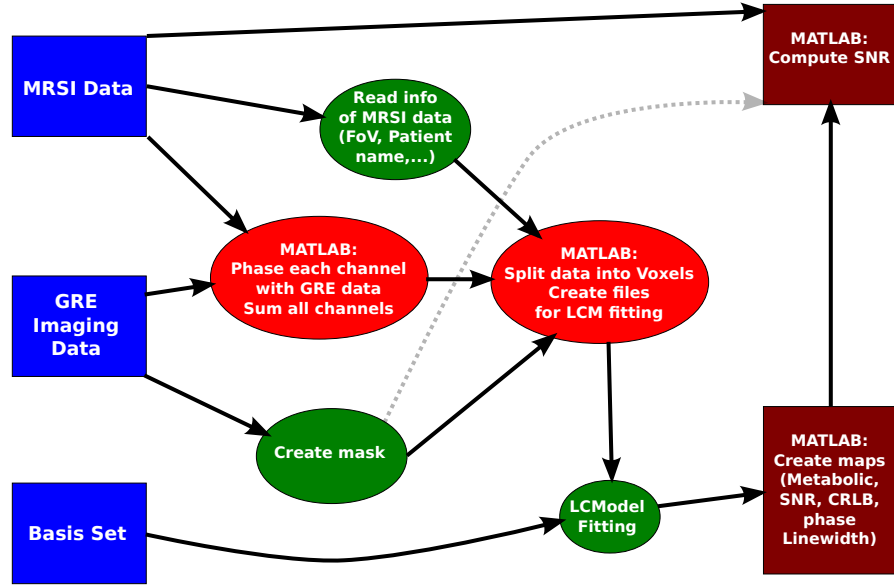


Figure 3.23: Flowchart of the program that was further extended with a self-written program to compute the SNR depicted in the top right.

i.e. the signal that remains after subtracting the fit [Provencher, 2011, p. 18]. In fig. 3.24 an example fit of LCMModel is given, showing the residuum at the top.

The SNR, as it is determined by LCMModel, is given by $\frac{Signal}{2 \cdot Noise}$. As already mentioned in section 3.1.4, a spectrum obtained from an FID based sequence contains a lot more signals from macromolecules and lipids than that of an typical echo sequence. These macromolecules have broad peaks that are hard to implement in the basis set. If not all metabolites that are visible in the spectrum are included in the basis set, or if their spectral shape is not perfectly Lorentzian, the residuum does not only contain pure white noise, but also metabolite signals or even artifacts (e.g. sideband artifacts). In such cases, the SNR computation of LCMModel is incorrect, since the “Noise” as well as the “Signal” scale with the real SNR, leading to a systematic underestimation of the computed SNR.

The SNR computation function includes the following subtasks:

3.4 Step 3: Validation of SNR Increase

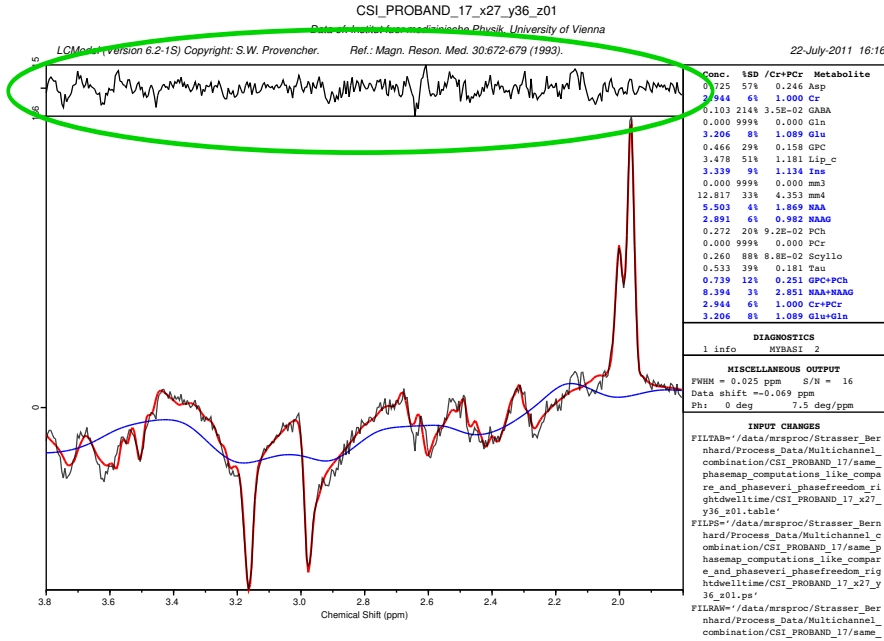


Figure 3.24: Example of a fit (red curve) and the baseline (blue curve) on the measured spectrum (black curve). The residuum at the top (green ellipse) is the difference of the fit to the measured spectrum.

1. Interpolate all spectra by performing zero filling in time domain to make them smoother, and thus, determining the maximum of the spectrum more accurately. The interpolated spectra are used for computing the “Signal”, the non-interpolated ones for the “Noise”, as zero filling can change the standard deviation of the noise.
2. Loop over all voxels
3. Compute the Noise, i.e. the standard deviation of the spectrum within user defined noise regions. Since this subtask is the backbone of the function, it is described in detail below. Remark: The noise definition of LCModel as the rms, and this definition coincide in case of a vanishing mean.
4. Determine the frequency shift of the spectrum by searching the remaining water peak.
5. Compute the “Signal”, defined as the height of the NAA peak. This step is as well described in detail below. The NAA peak is the highest metabolite peak in the

3 Implementation

human brain except for the water peak and signals from fats. This is why it was used for the SNR quantification.

6. Compute the SNR defined by $SNR := \frac{Signal}{2Noise}$. Ignore values with SNRs below 2, otherwise save the value in a matrix, containing the SNR values of all voxels.
7. Write an error log file and save plots of the whole process.

In contrast to the LCModel noise computation, the self written function computes the noise in a set of chemical shift ranges passed to the function, where no peaks normally are, and if there are some, the program excludes them. The region in the range of 6.5 to 9.5 ppm was used in this work, since no detectable metabolites resonate in this region.

The subtasks of the noise computation function are as follows:

1. Loop over all noise regions passed to the function
2. Fit the noise region with a linear regression. Subtract this baseline from the original data. This is necessary to deal with spectra suffering from poor water suppression.
3. Subdivide the noise region and compute the ratio of the "global" standard deviation (i.e. the standard deviation of the whole noise region) over the "local" standard deviation (i.e. the mean of the standard deviations of the subdivided spectrum). The global-to-local-noise-ratio is an indicator for peaks comprised within the noise region.
4. Smooth the data with a span derived from the global-to-local-noise-ratio. Subtract the smoothed data. This eliminates global variations in the noise as well as some peaks.
5. Exclude remaining peaks: Smooth the data with a constant span and find points that have an high absolute value compared to the standard deviation of the data. Exclude groups that comprise at least 14 of such data points. This number was estimated by error & trial.

A reason for remaining peaks in the noise region can be poor water suppression, leading to so called sideband artifacts. This artifact causes small peaks originating from water, shifted to different chemical shift values due to mechanical vibrations [de Graaf, 2007, p. 340]. Another possible reason are severe frequency shifts of the spectrum, so that metabolites have their resonance frequencies in the regions used for noise computation.

The computation of the "Signal" comprises the following subtasks:

1. Fit a linear regression to the signal within a region passed to the function. Subtract this baseline from the data.
2. Search for the peak, i.e. the maximum of the data in this region.
3. Define two "basis regions" in a certain distance from the peak on the left and the right side. The distance from the peak as well as the width of these two regions are passed to the function.
4. Compute the mean in both "basis regions".
5. Compute the "basis" as the mean value of these two means.
6. Define the height of the peak, i.e. the "Signal" as "peak value - basis value".

Evaluation of the SNR Results

In step 3, the data of four volunteer (Volunteer 3, Volunteer 5, Volunteer 6, Volunteer 7) and two phantom (Phantom 1, Phantom 2) measurements were used. A mask was created for all volunteers. The voxels within these masks were used for the SNR comparison. The "mask-voxels" of all volunteer measurements were put together. The means, standard deviations and standard errors of the SNR values using the following six combinations were determined:

1. VC measurement, SNR computed by LCModel
2. AC measurement, SNR computed by LCModel
3. SNR Ratio (AC/VC), SNR computed by LCModel
4. VC measurement, SNR computed by self written program
5. AC measurement, SNR computed by self written program
6. SNR Ratio (AC/VC), SNR computed by self written program.

The SNR ratios directly reflect the SNR increase when using the AC in comparison to the VC. The same was done for the phantom measurements separately. In order to check for consistency between different measurements, the values described above were also computed for each volunteer/phantom separately.

3.4.2 Results

The SNR maps of the AC, the VC and their ratio AC/VC are depicted in fig. 3.25 for using the SNR computation of LCModel as well as the self written program. For better comparison, the AC and VC maps are scaled the same. One can see that using the AC and our coil combination method significantly increases the SNR. Furthermore, the ratio maps show that every voxel has a higher SNR in case of the AC compared to the VC, even those voxels that are in the center of the head, where the sensitivity of surface coils is typically low.

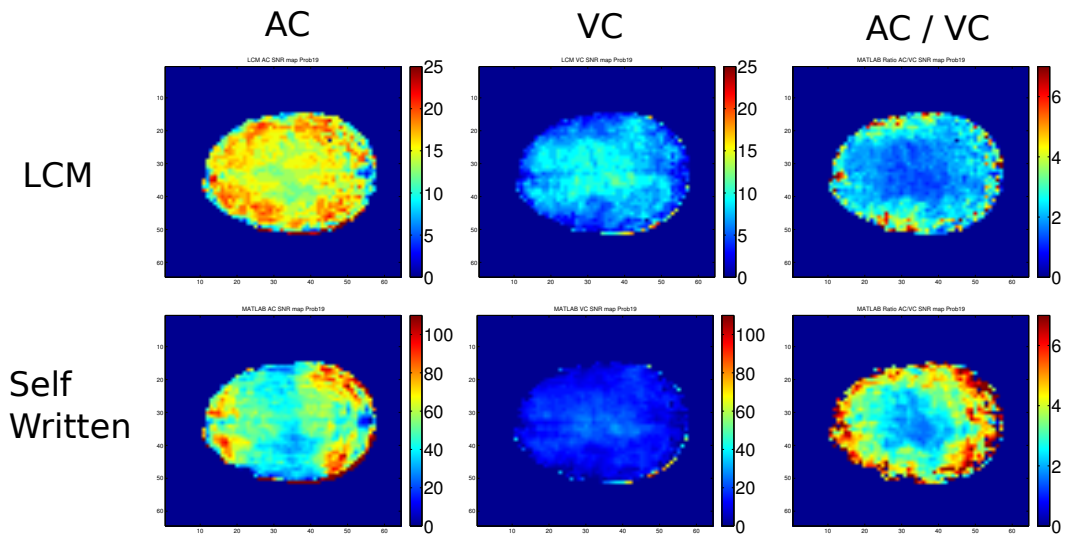


Figure 3.25: The SNR maps of the AC (left), the VC (center) MRSI data, and the ratio of these (right), resulting from the LCModel computation (top row) and the self written program (bottom). The AC and VC maps of both rows are scaled equally as well as the two ratio maps.

The quantitative assessment proves this impression: In table 3.2 the means, standard deviations and standard errors of the VC, AC and ratio SNR values are given. The computation was done for all volunteer voxels, and only those voxels within a user created mask were included. These masks are of rectangular shape, hence most “mask-voxels” are not near the surface of the brain. As a result, the computed SNR of the AC might be underestimated. The phantoms were treated separately, as their values differed again fundamentally from those of the volunteers.

3.4 Step 3: Validation of SNR Increase

	AC LCM	VC LCM	AC/VC LCM	AC SW	VC SW	AC/VC SW
Volunt.						
Mean	15.783	8.705	1.960	53.28	18.444	3.215
St. Error	0.040	0.030	0.011	0.26	0.082	0.022
St. Dev.	2.5	1.8	0.56	16	5.0	1.2
Phan.						
Mean	55.68	26.30	2.477	502	183.6	3.685
St. Error	0.73	0.50	0.060	14	7.4	0.069
St. Dev.	17	12	1.4	310	180	1.6

Table 3.2: Mean, standard error and standard deviation of the SNR values obtained by the LCModel SNR computation (LCM) and the self written (SW) SNR computation-program. The values are given for the AC, VC and their ratio AC/VC, separately for the volunteer (Volunt.) and the phantom (Phan.) measurements.

The standard deviations of all values are quite high, especially those of the AC. However, this is not surprising, since the sensitivity profile of ACs is more inhomogeneous than that of a VC. Moreover, the “SelfWritten SNR values” are higher than the “LCM SNR values” as one might suppose due to the sloppy SNR computation of LCModel. Because of this sloppy computation, the SNR ratios of the self-written program are assumed to be more reliable.

According to table 3.2, the SNR increases by a factor of approximately 3.2 for the volunteer measurements, and even 3.7 for the phantom measurements. This is a large SNR increase that can be traded for an increase of acquisition speed. That can be achieved e.g. by doing parallel imaging, a method where only a part of k-space is acquired. The rest is reconstructed by using the fact that the individual surface coils of an AC have a distinct sensitivity profile, hence comprising some additional spatial information [Pruessmann et al., 1999] [Griswold et al., 2002]. This acquisition acceleration method, as all others, reduces the SNR again, which can be compensated or even overcompensated by the SNR increase gained with the coil combination method of this work.

Like in step 1, the consistency between different measurements was checked as well by computing the mean and standard deviation of all individual data sets separately. The results are shown in table 3.3.

3 Implementation

	AC LCM	VC LCM	AC/VC LCM	AC SW	VC SW	AC/VC SW
Volun3						
Mean	15.299	7.808	2.067	51.89	16.36	3.397
St. Error	0.066	0.051	0.020	0.41	0.14	0.041
St. Dev	2.1	1.6	0.63	13	4.4	1.3
Volun5						
Mean	14.696	9.320	1.606	47.76	20.87	2.288
St. Error	0.074	0.0695	0.015	0.34	0.21	0.029
St. Dev	2.0	1.8	0.38	9.1	5.3	0.73
Volun6						
Mean	15.181	8.789	1.806	44.60	18.21	2.595
St. Error	0.061	0.062	0.017	0.34	0.15	0.031
St. Dev	1.8	1.8	0.48	9.8	4.3	0.90
Volun7						
Mean	17.383	9.082	1.982	64.78	19.08	3.530
St. Error	0.080	0.047	0.016	0.56	0.15	0.033
St. Dev	2.7	1.6	0.52	19	5.0	1.1
Phantom 1						
Mean	52.1	25.42	2.364	614	235	3.561
St. Error	1.1	0.60	0.083	22	13	0.090
St. Dev.	18	11	1.4	360	220	1.6
Phantom 2						
Mean	59.62	27.25	2.602	379	127.6	3.82
St. Error	0.97	0.82	0.086	11	5.0	0.11
St. Dev.	16	13	1.4	180	81	1.7

Table 3.3: SNR comparison between the AC and VC like in table 3.3, but for each volunteer/phantom separately. The ratios of Volunteer 5 were not computed voxelwise, but the means of the AC and VC measurements were divided and the errors were computed by propagation of uncertainty due to technical reasons.

One can see that the SNRs of the volunteers as well as the ones of the phantoms are consistent with each other. The GIN method is therefore proven to be reliable. However, the phantom measurements have a much higher SNR increase which is already clear from table 3.2.

3.5 Step 4: Comparison with Available Techniques

3.5.1 Materials & Methods

In this step, our method for coil combination is compared with the method implemented by Siemens at the 7 T scanner.

Description of the Available Technique

The available technique (denoted as “Siemens coil combination”) that is implemented at the 7 T Siemens scanner computes the phase based on the first FID point for all voxels and all channels. Using this value, the signal of each channel is phased. This phase can be assumed to be less accurate compared to the phase derived from the GRE image, since the remaining water peak can be distorted due to water suppression and is also 1000-10000 times smaller than the unsuppressed water peak, depending on the water suppression efficiency. Generally, a good water suppression is desired, but this complicates phase estimation. The principle of this technique is similar to the GRE based coil combination:

Each channel of the MRSI data is phased by

$$S_{FID,phased}(channel, \vec{r}, t) = e^{-i\varphi_{FID}(channel, \vec{r})} \cdot S_{MRSI}(channel, \vec{r}, t) \quad (3.7)$$

where φ_{FID} is the phase of the first FID time point of the MRSI data.

Each voxel is then weighted by its absolute value, so that the sensitivity profiles of the individual channels are taken into account.

$$S_{FID,weight}(channel, \vec{r}, t) = |S_{MRSI}(channel, \vec{r}, 0)| \cdot S_{FID,phased}(channel, \vec{r}, t) \quad (3.8)$$

Summing over all channels, and weighting with a factor to obtain homogeneous data, leads to:

3 Implementation

$$S_{FID,Comb}(\vec{r}, t) = \frac{\sum_{channel} S_{FIDweight}(channel, \vec{r}, t)}{\sqrt{\sum_{channels} |S_{MRSI}(channel, \vec{r}, 0)|^2}} \quad (3.9)$$

All in all, the combined signal is obtained by

$$S_{FID,Comb}(\vec{r}, t) = \frac{\sum_{channels} S_{MRSI}^*(channel, \vec{r}, 0) \cdot S_{MRSI}(channel, \vec{r}, t)}{\sqrt{\sum_{channels} |S_{MRSI}(channel, \vec{r}, 0)|^2}} \quad (3.10)$$

Comparison of the methods

The spectra resulting from the GIN method and that of the Siemens coil combination were compared qualitatively, as well as metabolic maps of NAA, total creatine, total choline, *myo*-inositol and their ratios to NAA. The SNR computed by LCModel and that by the self-written program were compared quantitatively like in step 3.

3.5.2 Results

In fig. 3.26, the spectra resulting from the VC, the AC using the GIN method, and the AC using the Siemens coil combination are shown. Spectra where phase problems are expected, i.e. at the border of the brain, were chosen.

Particularly in figures 3.26(a) - 3.26(c) one can see that the Siemens coil combination can result in spectra of poor quality, whereas the same spectrum resulting from the GIN method is of good quality. Moreover, while the spectrum processed with the Siemens method does not resemble the VC spectrum, the one resulting from the GIN method does. The Siemens coil combination can also alter the ratio between different peaks heavily, which is demonstrated in figures 3.26(d) - 3.26(f). In figures 3.26(g) - 3.26(i) finally, the Siemens coil combination seems not to distort the spectrum, but the SNR is decreased compared to the GIN method.

When comparing more spectra, one can say that spectra of high quality are very similar for both competitive methods. However, in areas where phasing is problematic, e.g. at the border of the brain, the GIN method performs much better than the Siemens coil combination.

Comparing the metabolic maps of the VC and the two methods, the similarity between the maps of the VC and the GIN method is remarkable. By contrast, the metabolic maps of the Siemens coil combination appears totally different as shown in fig. 3.27 for

3.5 Step 4: Comparison with Available Techniques

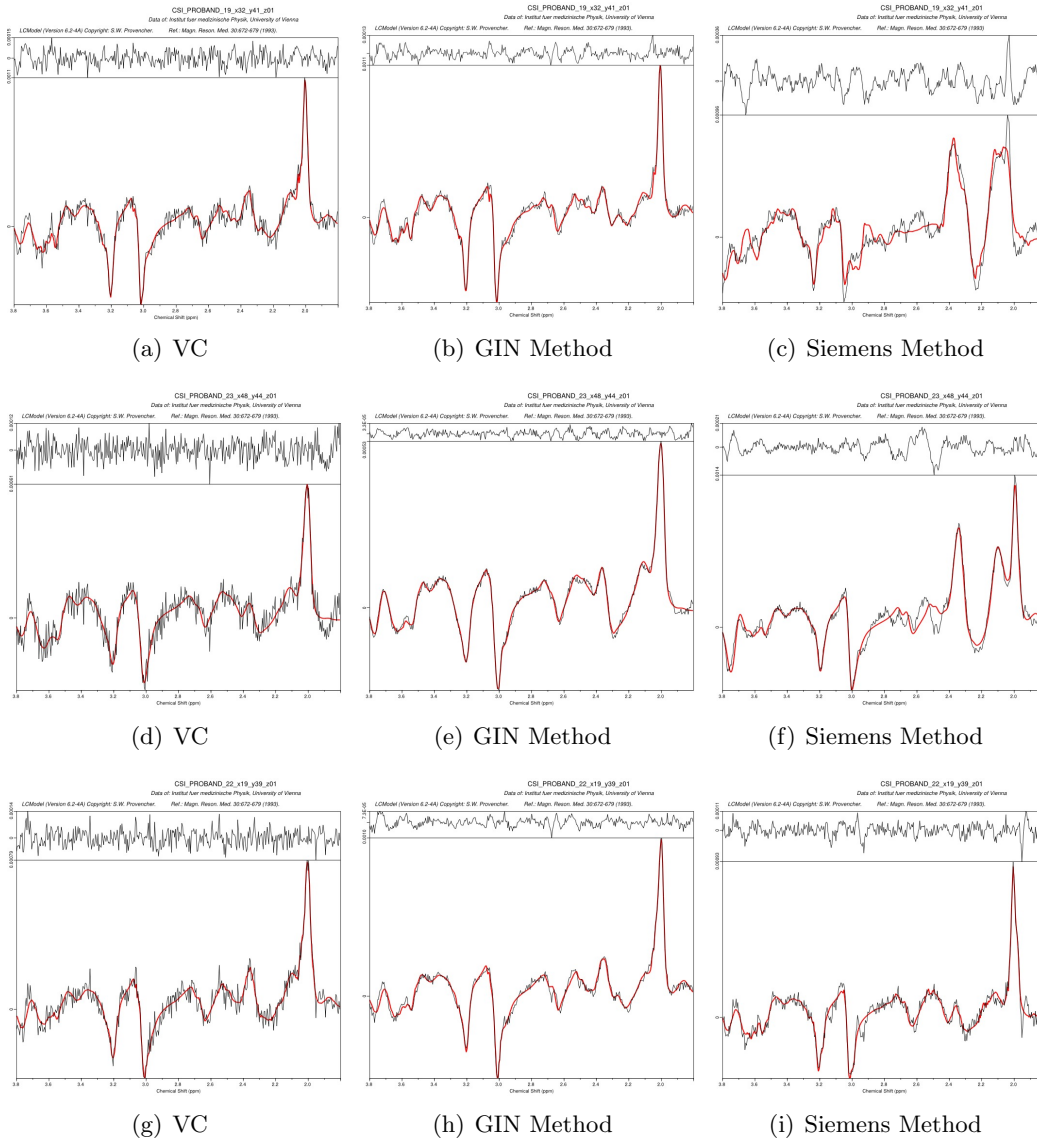


Figure 3.26: The fitted spectra resulting from the VC (left), the AC-GIN method (center), and the AC-Siemens method (right). (a)-(c) The Siemens spectrum is heavily distorted and therefore unusable. (d)-(f) The ratios of the peaks in the Siemens spectrum are very different to that of the reference (VC spectrum). (g)-(i) Even if the spectrum obtained with the Siemens method is not distorted, the SNR is often lower than the SNR of the GIN method.

myo-inositol and NAA. When scaling all three maps equally as it was done for creatine and choline, the strongly differing metabolic concentrations have to be noted. Nevertheless, the metabolic ratio maps to NAA, fig. 3.28, are in good accordance with each

3 Implementation

other. It seems that when fitting the spectra resulting from the Siemens method, all metabolites are over- or underestimated in the same regions, and computing ratios thus compensates these errors.

The SNR comparison between both methods is shown in table 3.4. One can see that the GIN method does not only improve the appearance of the spectra and metabolic maps, but also increases the SNR, which is to be expected, because wrong phasing of the spectra prior to summing them leads to signal cancellation, and therefore to an SNR decrease.

	GIN/Siemens LCM	GIN/Siemens SW
Volunteers		
Mean	1.374	1.574
St. Error	0.017	0.029
St. Dev.	1.2	2.0
Phantoms		
Mean	2.13	1.254
St. Error	0.22	0.036
St. Dev.	4.0	0.69

Table 3.4: Mean, standard error and standard deviation of the SNR ratio “GIN / Siemens” obtained by the LCModel SNR computation (LCM) and the self written (SW) SNR computation-program.

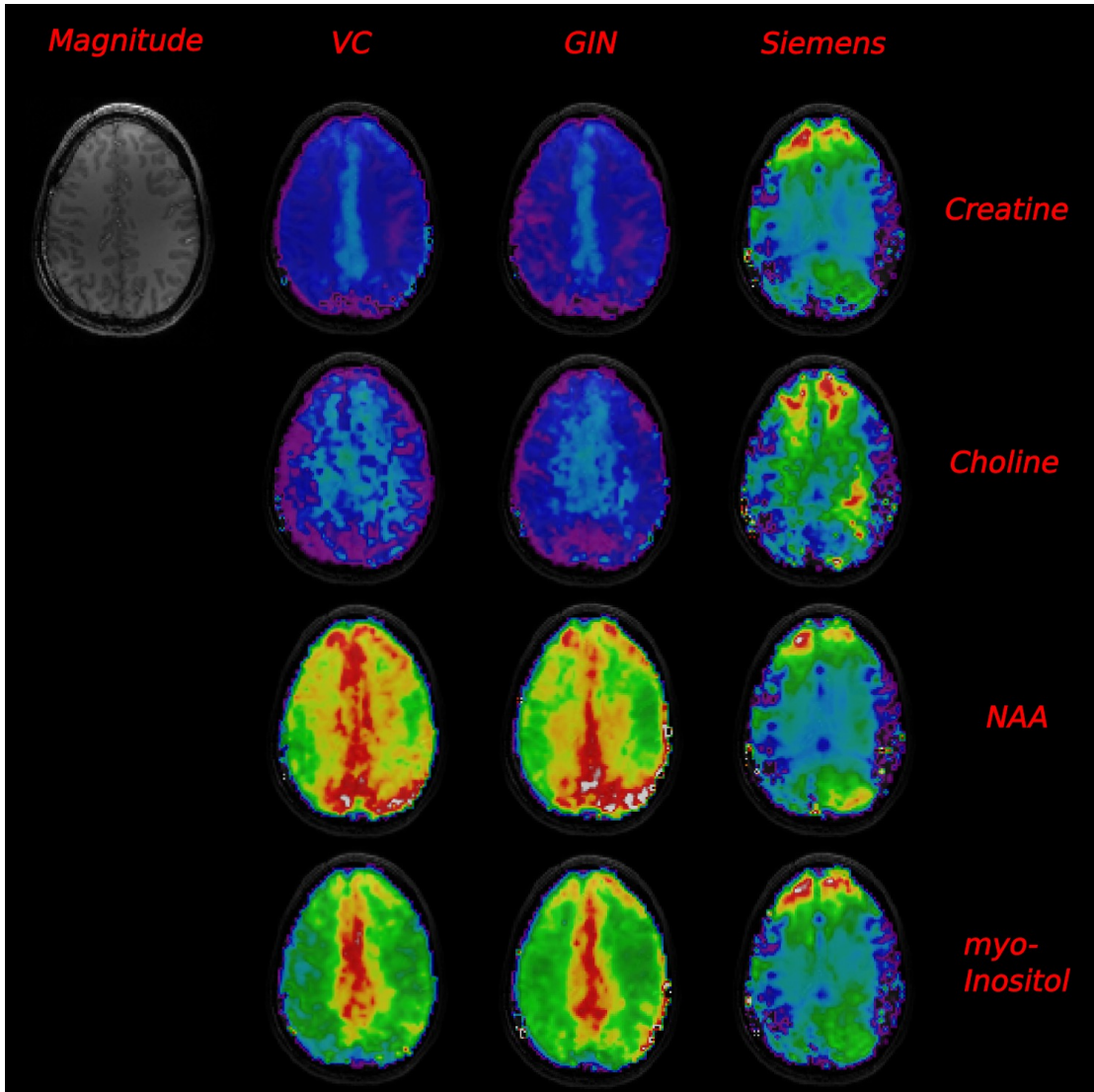


Figure 3.27: The metabolic maps of creatine, choline, NAA and *myo*-inositol derived from the VC data (left), AC data using the GIN method (center), and AC data using the Siemens method (right) are shown, as well as the magnitude map of the brain acquired with a 3D-imaging sequence. The maps of creatine and choline are scaled equally for all three methods to show the difference in the fitted concentrations between the VC and AC-GIN maps on the one hand, and the AC-Siemens maps on the other. In case of NAA and *myo*-inositol, only the VC and AC-GIN maps are scaled the same. The AC-Siemens map is not, in order to stress the different appearance of the latter map.

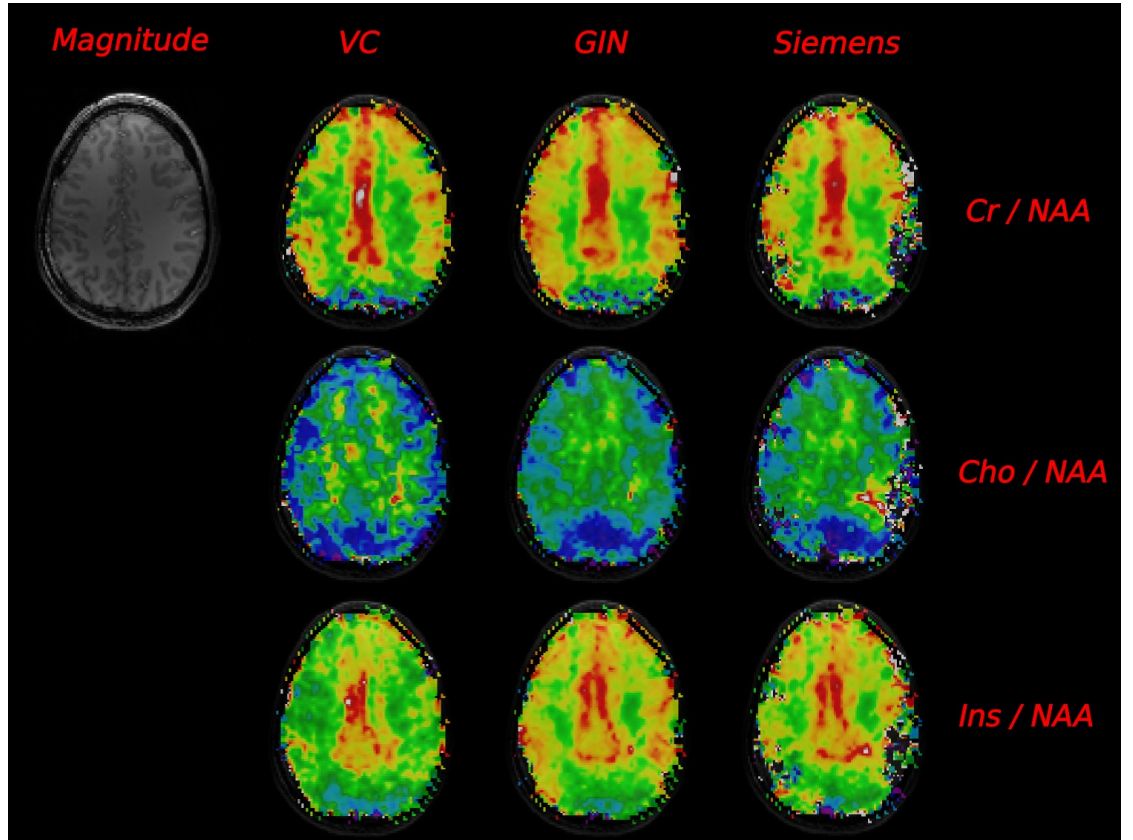


Figure 3.28: The ratio metabolic maps of total creatine/NAA (Cr/NAA), total choline/NAA (Cho/NAA), and *myo*-inositol/NAA (Ins/NAA) obtained from the VC data (left), AC data using the GIN method (center), and AC data using the Siemens method (right). Moreover a magnitude map of the brain is shown.

4 Summary

In this diploma thesis, a new method for combining multichannel MRSI data of an AC at 7 T was presented, and its feasibility was proven. In case of MRSI, coil combination is critical due to signal cancellations resulting from phase deviations of different channels. For this reason, the presented method uses the data acquired with a standard GRE sequence. The GRE based phase and magnitude is used to phase and weight the MRSI signals of each AC-channel, in order to sum up the signals of all channels, thus highly increasing the SNR compared to a VC.

Summarizing the results, one can conclude that using GRE data for phasing AC-channels prior to coil combination is feasible and leads to increased SNR and reliability of the fit after coil combination.

More specifically, the possibility of phasing MRSI with GRE data was shown to be reliable, leading to no difference in the metabolite concentrations and CRLBs computed by LCModel, even for low quality spectra. The phase however is estimated more reliable using the GRE data than LCModel does in case of low quality data.

Moreover, using an AC and the proposed method highly increases the SNR compared to VCs, which consequently leads to a more reliable quantification of metabolite concentrations in volunteers, showing up as reduced CRLB values. Therefore, at least 7 metabolites could be quantified with an $\text{CRLB} \leq 20\%$ in almost all spectra in the human brains of healthy volunteers.

The proposed method was furthermore proven to perform better in qualitative and quantitative assessment than the state of the art method does.

Nevertheless, there are still some limitations of this coil combination method, as the method is still inconvenient in its use, since the three GRE image measurements in addition to the MRSI one have to be performed manually, which have then passed to the coil combination program. In future, a sequence that performs these three GRE measurements automatically as pre-scans, and an automatic reconstruction of the MRSI

4 Summary

data performing the phasing and summing with these pre-scans directly on the scanner console computer is planned.

Further improvements in near future include the option to perform parallel imaging based on this coil combination method. With parallel imaging, the acquisition time is supposed to be reduced from 30 minutes to under 10 minutes by trading some of the SNR that is gained with the GIN method, bringing the acquisition durations to times that are feasible in clinical routine. In the long term, this work can be seen as part of a project to make high-resolution MRSI to an integral part in clinical routine, particularly in pre-operative planning of surgeries in the brain (“7 Tesla MR spectroscopy in diffusely infiltrating gliomas”, FWF Grant KLI 61, 2011).

Bibliography

- N.I. Avdievich, J.W. Pan, J.M. Baehring, D.D. Spencer, and H.P. Hetherington. Short Echo Spectroscopic Imaging of the Human Brain at 7T Using Transceiver Arrays. *Magnetic Resonance in Medicine*, 62(1):17–25, 2009. doi: {10.1002/mrm.21970}.
- G. Badurek. *Biological and medical applications of nuclear physics II*. Lecture Notes, 2010.
- F. Bloch. Nuclear Induction. *Physical Review*, 70(7):460 – 474, 1946.
- V.O. Boer, J.C.W. Sieroa, H. Hoogduina, J.S. van Gorp, P.R. Luijtena, and D.W.J. Klomp. High-field MRS of the human brain at short TE and TR. *NMR in Biomedicine*, 24(9):1081 – 1088, 2011. doi: {10.1002/nbm.1660}.
- W. Bogner, S. Gruber, S. Trattnig, and M. Chmelik. High-resolution mapping of human brain metabolites by proton FID-MRSI at 7T. [EPub], 2011. doi: {10.1002/nbm.1805}.
- R.A. de Graaf. *In Vivo NMR Spectroscopy: Principles and Techniques*. John Wiley & Sons, 2nd edition, 2007.
- R.A. de Graaf, P.B. Brown, S. McIntyre, T.W. Nixon, K.L. Behar, and D.L. Rothman. High magnetic field water and metabolite proton T1 and T2 relaxation in rat brain in vivo. *Magnetic Resonance in Medicine*, 56(2):386–394, 2006.
- M.A. Griswold, P.M. Jakob, R.M. Heidemann, M. Nittka, V. Jellus, J. Wang, B. Kiefer, and A. Haase. Generalized Autocalibrating Partially Parallel Acquisitions (GRAPPA). *Magnetic Resonance in Medicine*, 47(6):1202–1210, 2002. doi: {10.1002/mrm.10171}.
- N. Gurker. *Computerunterstützte Abbildungsverfahren*. Lecture Notes, 2011.
- E.M. Haacke, R.W. Brown, M.R. Thompson, and R. Venkatesan. *Magnetic Resonance Imaging: Physical Principles and Sequence Design*. John Wiley & Sons, New York, 1st edition, 1999.
- A. Henning, A. Fuchs, J.B. Murdoch, and P. Boesiger. Slice-selective FID acquisition, localized by outer volume suppression (FIDLOVS) for (1)H-MRSI of the human brain at 7 T with minimal signal loss. *NMR in Biomedicine*, 22(7):683–696, 2009. doi: {10.1002/nbm.1366}.

BIBLIOGRAPHY

- C. Horn. Parameter selective MR-Microimaging of Biomaterials with short T2s. Master's thesis, University of Technology, Vienna, 2012.
- J.P. Hornak. The Basics of MRI. URL: <http://www.cis.rit.edu/htbooks/mri>, 2011. Access time: 31.03.2012.
- U. Katscher and P. Börnert. Parallel RF transmission in MRI. *NMR in Biomedicine*, 19(3):393–400, 2006.
- R. Mekte, V. Mlynárik, G. Gambarota, M. Hergt, G. Krueger, and R. Gruetter. MR spectroscopy of the human brain with enhanced signal intensity at ultrashort echo times on a clinical platform at 3T and 7T. *Magnetic Resonance in Medicine*, 61(6):1279–1285, 2009.
- V. Mlynárik, G. Gambarota, H. Frenkel, and R. Gruetter. Localized short-echo-time proton MR spectroscopy with full signal-intensity acquisition. *Magnetic Resonance in Medicine*, 56(5):965–970, 2006.
- R.J. Ogg, P.B. Kingsley, and J.S.: Taylor. WET, a T1- and B1- insensitive water suppression method for in vivo localized ^1H NMR spectroscopy. *Journal of Magnetic Resonance B*, 104(1):1–10, 1994.
- S.W. Provencher. Estimation of metabolite concentrations from localized in vivo proton NMR spectra. *Magnetic Resonance in Medicine*, 30(6):672–679, 1993. doi: {10.1002/mrm.1910300604}.
- S.W. Provencher. *LCModel & LCMgui User's Manual*, September 2011.
- S.W. Provencher. LCModel website. URL: <http://www.s-provencher.com/pages/lcmodel.shtml>, March 2012. Access time: 31.03.2012.
- K.P. Pruessmann, M. Weiger, M.B. Scheidegger, and P. Boesiger. SENSE: Sensitivity Encoding for Fast MRI. *Magnetic Resonance in Medicine*, 42(5):952–962, 1999. doi: {10.1002/(SICI)1522-2594(199911)42:5<952::AID-MRM16>3.0.CO;2-S}.
- J. Reichenbach and M. Haacke. *Susceptibility Weighted Imaging in MRI*. John Wileys & Sons, 1st edition, 2011.
- S. Robinson, G. Grabner, S. Witoszynskyj, and S. Trattnig. Combining Phase Images From Multi-Channel RF Coils Using 3D Phase Offset Maps Derived From a Dual-Echo Scan. *Magnetic Resonance in Medicine*, 65(6):1638–1648, 2011. doi: {10.1002/mrm.22753}.
- U. Seeger, U. Klose, I. Mader, W. Grodd, and T. Nägele. Parameterized evaluation of macromolecules and lipids in proton MR spectroscopy of brain diseases. *Magnetic Resonance in Medicine*, 49(1):19–28, 2003. doi: {10.1002/mrm.10332}.
- P. Tofts. Standing Waves in Uniform Water Phantoms. *Journal of Magnetic Resonance*, 104(B):143–147, 1994.

- J.W. van der Veen, R. de Beer, P.R. Luyten, and D. van Ormondt. Accurate quantification of in vivo ^{31}P NMR signals using the variable projection method and prior knowledge. *Magnetic Resonance in Medicine*, 6(1):92–98, 1988. doi: {10.1002/mrm.1910060111}.
- L. Vanhamme, A. van den Boogaartb, and S. Van Huffel. Improved Method for Accurate and Efficient Quantification of MRS Data with Use of Prior Knowledge. *Journal of Magnetic Resonance*, 129(1):35–43, 1997.

Acknowledgements

Foremost I want to thank Ass. Prof. Wolfgang Bogner at the Medical University of Vienna for making this diploma thesis possible and for providing, among other things, a working place, measurement time at the scanner, his immense knowledge about NMR and a stipend for me (thank you for prolonging my stipend over and over again!). Thank you as well for your patience, for proofreading everything I ever wrote about NMR, and for the good working atmosphere. We still have to perform **scientific** NMR measurements of beer!

My special gratitude I want to express to Prof. Wilfried Schranz at the University of Vienna for his supervision, despite the occupation with all his other diplomands and doctorands and his own research work!

I want to thank all colleagues for support, especially Christian Horn for providing the sequence images, Stephan Witoszynskyj for helping me solve the phase problems of the GRE images, Marek Chmélík for explaining me everything when Wolfgang was on vacation, Simon Robinson for helping me with understanding the phase and its sources in general, and Gilbert Hangel and Martin Gajdošík for all the fun at work.

To all friends I want to pass on my cordially greetings! Thank you for all the distraction by playing AoE2 against me and always losing disastrously, David, Sam, Andreas and Marius! Thank you also Maria and David, and Christian, Anika, Pia and Clemens for tons of fun with playing old-school board games! I also would like to show my gratitude to Goran & Marija for annihilating liters of beer with me, Marcus for disassembling the whole world, and Chrizzy for discussing interesting scientific and mathematical topics.

I feel very indebted to my family, especially to Helga, Roman and Ursula Strasser, for solving the unsolvable problem of bringing me up, for all their encouragement and for not conducting the resolution of beating me to coma when I ran for hours after my sister, trying to bite her.

With all my heart I want to thank my future girlfriend, for all her love and support. I hope you will be pleased that I wrote this acknowledgement in wise foresight, although we might not know each other yet! Without you I will be nothing!

Curriculum Vitae of Bernhard Strasser

Contact Information

Name	Bernhard Strasser
Address	Hilschergasse 4/10 1120 Wien Austria
Cell Phone	0660/5270987
E-Mail	bernhard.strasser@meduniwien.ac.at

Personal information

Date of Birth	26.05.1987
Place of Birth	Salzburg, Austria
Citizenship	Austria

Employment History

2005 – 2006	Civilian Service at the Samariterbund Salzburg
--------------------	--

Education

1993 – 1997	Elementary School, Volksschule Obertrum
1997 – 2001	Secondary School, BG Zaunergasse
2001 – 2002	Vocational School, Technical School Itzling, Department of Electrical Engineering
2002 – 2005	Secondary School, BG Zaunergasse
July 2005	Higher School Certificate, passed with merit
Since 2006	Diploma studies in physics at the University of Vienna
Since March 2011	Diploma thesis about “Increasing the Signal to Noise Ratio in MR Spectroscopic Imaging by Coil Combination at 7T”

Professional Qualifications

Languages	German (native language) English Italian (basis knowledge) Latin (basis knowledge)
------------------	---

Driver licence	B
-----------------------	---

Computer Skills	Programming in MATLAB, Bash, LaTeX, Fortran 90, C Basics in Ubuntu, Windows, Open Office, Word, Excel
------------------------	--

Conference Contributions

May 2011:

Talk at International Workshop “Magnetic Resonance Studies” in Třešť, “Prior knowledge in CSI obtained from phase images: initial results”, Strasser B, Chmelik M, Trattnig S, Gruber S, Bogner W

September 2011:

Talk at Workshop “Methods in Proton MR Spectroscopy – Data Acquisition and Evaluation” in Tübingen, “Improved quantification of CSI data by phase prior knowledge: Application to Multichannel coils”, Strasser B, Chmelik M, Trattnig S, Gruber S, Bogner W

October 2011:

E-Poster at the ESMRMB in Leipzig, “Prior Knowledge in CSI Obtained from Phase Images: Initial Results”, Strasser B, Chmelik M, Trattnig S, Gruber S, Bogner W

Personal Interests

Music, Science, Sports